ORGANIC PHOTOVOLTAICS: INTEGRATING NON-FULLERENE ACCEPTORS INTO SOLUTION-PROCESSED DEVICES

by

Jon-Paul Sun

Submitted in partial fulfilment of the requirements
for the degree of Doctor of Philosophy

at

Dalhousie University
Halifax, Nova Scotia
August 2017

TABLE OF CONTENTS

LIST OF TABLES

LIST OF FIGURES

ABSTRACT

In recent decades the demand for low-cost and sustainable energy sources has fueled the growth of photovoltaic research. Among the various photovoltaic technologies, organic semiconductors offer a light-weight and inherently-flexible solution that can be fabricated in a roll-to-roll process, significantly reducing fabrication and installation costs. Additionally, due to their transparent nature a number of previously unutilized architectural surfaces such as windows, building facades, and vehicle panels can be employed for energy production.

Among solution-processed organic photovoltaics, fullerenes have dominated as the highest performing electron acceptor materials. However, their low absorption in the solar spectrum and high-energy synthesis is undesirable. Non-fullerene acceptors have the potential for low-cost synthesis while providing complementary absorption to the donor material, enhancing photocurrent.

This dissertation presents the design, characterization, and integration into solar cells of novel non-fullerene acceptors. A family of related push-pull chromophores with phthalimide or naphthalimide end-groups, as well as perylene diimide-based acceptors were characterized using a combination of ultraviolet-visible absorption spectroscopy and ultraviolet photoemission spectroscopy. The acceptor molecules were integrated into thin-film transistors to measure field-effect mobilities. Solution-processed bulk heterojunction photovoltaic devices were fabricated and characterized using atomic force microscopy and by measuring current density-voltage curves and external quantum efficiencies while under illumination. The best performing devices achieved power conversion efficiencies of 5.5 %, where overall performance was limited by domain sizes in the blend films. Difficulties in forming nanoscale domain sizes in blend films are presented and discussed.

A low-cost nanoembossing technique utilizing anodized aluminum oxide templates is presented to address the associated challenges with bulk heterojunctions. Initial results show that small-molecule acceptor films can be nanostructured prior to donor material deposition. This presents a viable method for fabricating large-area modules with predetermined nanoscale domain sizes, that is compatible with roll-to-roll processing.

LIST OF ABBREVIATIONS AND SYMBOLS USED

Abbreviations

AAO	anodized aluminum oxide
AFM	atomic force microscopy
AM0	air mass 0
AM1.5D	air mass 1.5 direct
AM1.5G	air mass 1.5 global
B3LYP	Becke, 3 parameter, Lee, Yang, Parr
BE	binding energy
BHJ	bulk heterojunction
c-pol-TOM	circularly polarized transmission optical microscopy
CB	conduction band
CT	charge transfer
D/A	donor/acceptor
DFT	density functional theory
DI	deionized
DPP	diketopyrrolopyrrole
DUT	device under test
ESP	electrostatic potential
EQE	external quantum efficiency
FF	fill factor
HMDS	hexamethyldisilazane
HOMO	highest occupied molecular orbital
IPCE	incident photon conversion efficiency
IR	infrared
ITO	indium tin oxide
JV	current density-voltage
KE	kinetic energy
LCR	inductance, capacitance, resistance
LUMO	lowest unoccupied molecular orbital

OPV	organic photovoltaic
P3HT	poly(3-hexylthiophene)
PCE	power conversion efficiency
PEDOT:PSS	poly(3,4-ethylenedioxythiophene) polystyrene sulfonate
PDI	perylene diimide
PMMA	polymethylmethacrylate
ppm	parts per million
PTCDI	perylene-3,4,9,10-tetracarboxylic diimide
PTFE	polytetrafluoroethylene
PV	photovoltaic
SEM	scanning electron microscopy
TFT	thin film transistor
UPS	ultraviolet photoelectron spectroscopy
UV-vis	ultraviolet-visible
v/v	volume per volume
VB	valence band
XRD	x-ray diffraction

Symbols

B_λ	spectral radiance
c	speed of light
C_{ox}	specific capacitance (transistor dielectric)
e	elementary charge
ε	electric field
D_n	electron diffusion coefficient
D_p	hole diffusion coefficient
E	energy
E_0	ground state energy
E_B	binding energy
$E_{B,CT}$	charge-transfer binding energy
E_F	Fermi level

E_{onset}	secondary onset binding energy
E_{VBM}	valence band maximum binding energy
E_{xc}	exchange-correlation energy
F_n	electron quasi-Fermi level
F_p	hole quasi-Fermi level
h	Planck's constant
H	Hamiltonian
I_D	drain current
j	power density
J_{sc}	short-circuit current density
J_n	electron current density
J_p	hole current density
k_B	Boltzmann constant
L	length
λ	wavelength
μ_n	electron mobility
μ_p	hole mobility
n	electron density
ω	spin speed
p	hole density
Φ	energy difference between Fermi level and local vacuum level
φ	atomic wavefunction
ψ	molecular wavefunction
r	radius
ρ	resistivity
$\rho(r)$	electron density
R_s	sheet resistance
P_{max}	maximum power density
t	thickness
T	temperature
T_e	electron kinetic energy

V_{app}	applied voltage
V_{DS}	drain-source voltage
V_{ee}	electron-electron Coulomb potential energy
V_{en}	electron-nucleus Coulomb potential energy
V_{GS}	gate-source voltage
V_{oc}	open circuit voltage
V_t	threshold voltage
W	width
x	concentration

CHAPTER 1 INTRODUCTION

1.1 GLOBAL ENERGY DEMAND

For most of human civilization, economic activity has been limited by the doctrine that total global wealth is a fixed amount.[1] However, in 1776, Adam Smith published *An Inquiry into the Nature and Causes of the Wealth of Nations*, demonstrating that through free markets, division of labor, and accumulation of capital, total global wealth is capable of sustained growth.[2] Concurrently, the Industrial Revolution was well underway, combining these new economic theories with technological advances in steam power, metallurgy, rail transport, machining, and agriculture.[3] Over the past two hundred years, dramatic changes to the global economy have resulted in a twenty-fold increase in global power consumption, and a nearly ten-fold increase in human population. Figure 1.1 shows global power consumption (top panel) and human population (center panel) from 1800-2010. Throughout these years, the majority of energy usage has been from sources that emit carbon dioxide (CO_2) into the atmosphere. The bottom panel of Figure 1.1 shows mean atmospheric CO_2 concentration. The dashed line at 300 ppm indicates the maximum level of CO_2 concentration prior to 1900, going backwards in time 800,000 years.

The role of atmospheric gases, such as CO_2, in trapping heat radiating from the surface of the Earth was analyzed by Joseph Fourier as early as the 1820s.[4] In the last few decades the large-scale observable effects of rising CO_2 levels have begun to manifest as increasing global surface temperatures,[5] rising sea levels,[6] and increased occurrences of extreme weather phenomena.[7,8] At this juncture in human history, it seems imperative to transition energy producing technology to non-CO_2 emitting sources, with solar photovoltaics among the leading candidates. As of 2010, total global solar photovoltaic capacity amounted to approximately 40 GW. By 2014 this had increased to 180 GW and is expected to surpass 450 GW by 2020.[9]

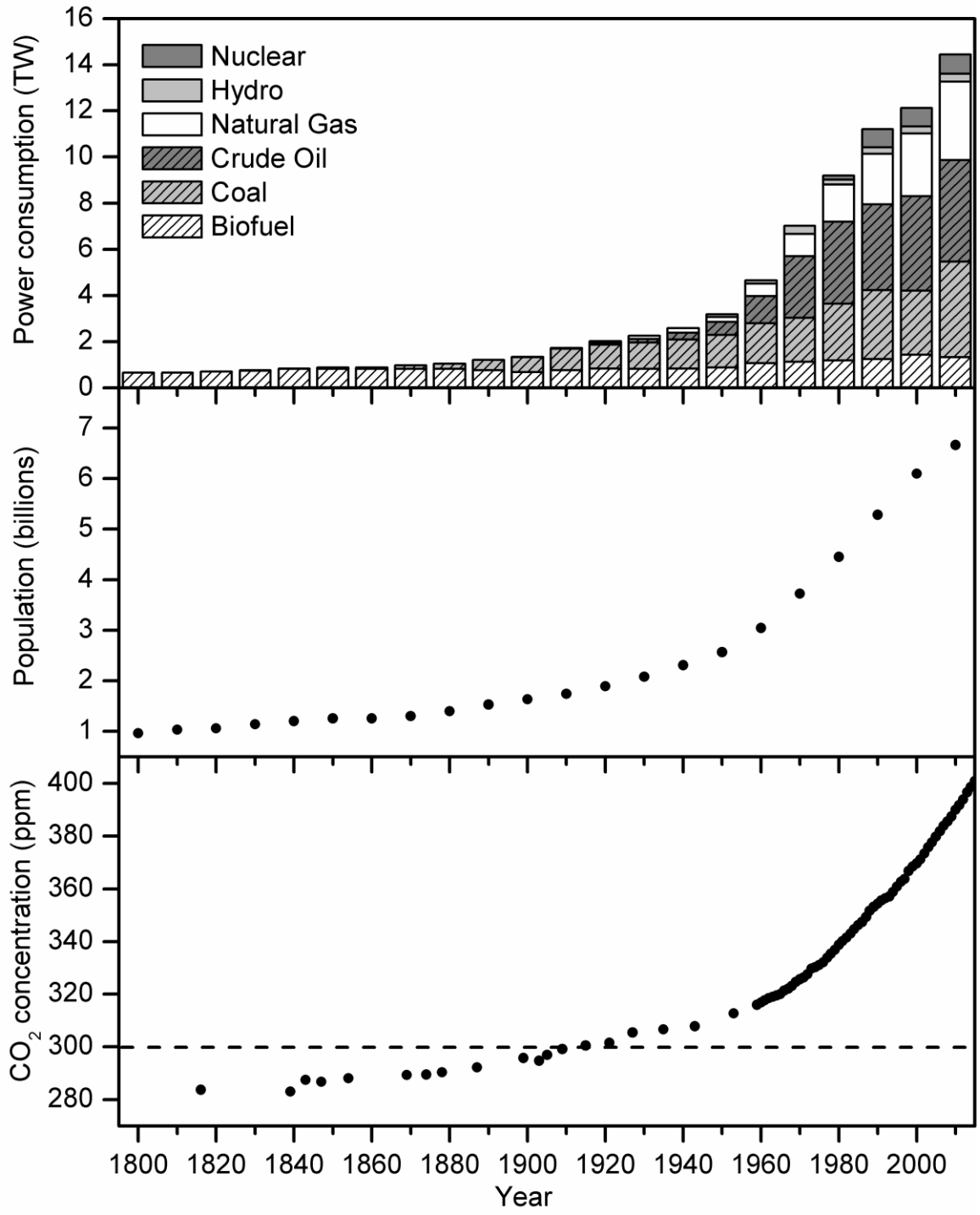

Figure 1.1. Global power consumption (top panel), data from[10]; human population (center panel), data from[11]; and mean atmospheric CO_2 concentration (bottom panel) from 1800-2010, data from[12,13]. The dashed line in the bottom panel represents the maximum CO_2 concentration for 800,000 years prior to 1900.[14]

1.2 SOLAR ENERGY RESOURCES

Planck's Law describes the spectral radiance of a blackbody at a given wavelength λ and temperature T

$$B_\lambda(\lambda,T) = \frac{2hc^2}{\lambda^5} \cdot \frac{1}{e^{hc/\lambda k_B T} - 1} \quad [\mathrm{W \cdot sr^{-1} \cdot m^{-3}}] \tag{1}$$

where k_B is the Boltzmann constant, c is the speed of light in a vacuum, and h is Planck's constant. Integration of B_λ over all wavelengths and solid angles results in the Stefan-Boltzmann law for the total power radiated per unit area

$$j = \frac{2\pi^5 {k_B}^4}{15c^2h^3} T^4 \quad [\mathrm{W \cdot m^{-2}}] \tag{2}$$

This formula can be modified to determine the solar power per unit area incident upon Earth's atmosphere when the Sun is approximated as a blackbody

$$j_{Earth} = \frac{2\pi^5 {k_B}^4}{15c^2h^3} T^4 \cdot \left(\frac{r_{Sun}}{r_{Sun-Earth}} \right)^2 \quad [\mathrm{W \cdot m^{-2}}] \tag{3}$$

where r_{Sun} is the radius of the sun (6.957×10^8 m), and $r_{Sun\text{-}Earth}$ is the distance from the Sun to the Earth (1.496×10^{11} m). Evaluation of (3), using the Sun's surface temperature (5778 K), leads to a power density of approximately 1400 $\mathrm{W \cdot m^{-2}}$. This corresponds to what is commonly referred to as Air Mass 0 (AM0), with a standard value of 1366.1 $\mathrm{W \cdot m^{-2}}$. For terrestrial solar applications, attenuation through the Earth's atmosphere needs to be taken into account, arriving at the AM1.5G value of 1000 $\mathrm{W \cdot m^{-2}}$. The 1.5 indicates the number of atmospheric thicknesses that solar energy passes through at a solar zenith angle of 48.2°, an accepted standard that is representative of Earth's major population centers. G indicates global, which is a combination of direct and diffuse light.

For solar concentrator applications, an alternative AM1.5D (D = direct) is used with a total power density of 900 $W \cdot m^{-2}$.

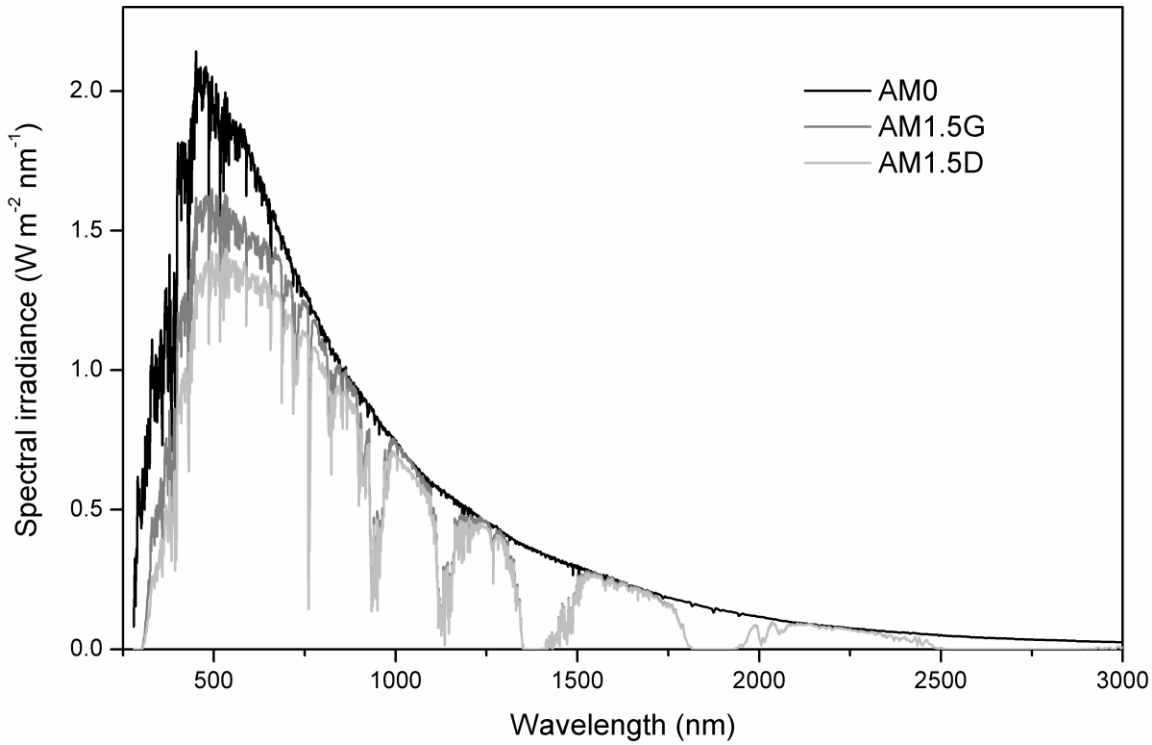

Figure 1.2. AM0, AM1.5G, and AM1.5D solar spectra.

Figure 1.2 shows the standard solar spectra for AM0, AM1.5G, and AM1.5D. Using the AM1.5G illumination intensity, it becomes apparent that solar photovoltaics have the potential to supply a significant fraction, if not all, of Earth's power requirements. Even at modest power conversion efficiencies (PCEs) of 10 %, 20 TW of power could be supplied from an area of 200,000 km^2, approximately four times the area of Nova Scotia.

1.3 Photovoltaic Technologies

Photovoltaics (PVs) have been under investigation for a number of decades, with new materials and device configurations continuing to emerge. Figure 1.3 shows the best research-cell PCEs for various technologies from 1976-2017.[15] The best performing

PVs are currently made from III-V semiconductors, achieving up to 46 % PCE in multijunction devices. These devices are epitaxially grown by chemical vapor deposition on top of single crystal Ge or GaAs wafers.[16] Recent lift-off techniques have been developed to allow for the 2-5 μm thick devices to be peeled from the substrate, allowing the wafers to be reused several times. This has reduced the cost per watt to approximately $50 USD.[17] Despite the cost reduction, this technology is still comparatively expensive and is predominantly used in solar concentrator arrays or space-based applications. Crystalline silicon PVs achieve moderate PCEs of approximately 25 % in research-cell devices. The cost per watt of the modules has dropped to below $0.50 USD recently.[18] However, since the modules are rigid and thicker than other technologies (~ 200 μm), mechanically robust mounts required to support the panels and longer installation times lead to an installation cost approximately ten times larger than the price of the modules.

The remaining technologies in Figure 1.3 are commercially-available thin-film PVs and emerging PVs, many of which are also thin-film technologies. The benefit of a thin-film technology is that the devices can often be fabricated on flexible plastic substrates in a roll-to-roll process, reducing the cost of the modules. Additionally, since installing thin-film PVs only requires laminating a pre-existing surface, the installation cost can be reduced. Organic photovoltaics (OPVs) are a thin-film technology that is expected to have a large presence in building-integrated PVs. The light-absorbing dyes and pigments can be made at very low cost and are already produced in quantities of millions of tons per year.[19] Additionally, the optical properties can be easily tuned such that a wide variety of colors can be attained, satisfying the aesthetic requirement for building integration. OPVs have made significant gains in PCE over the past two decades,[20] with a best certified research-cell PCE of 11.5 % in 2015.[21]

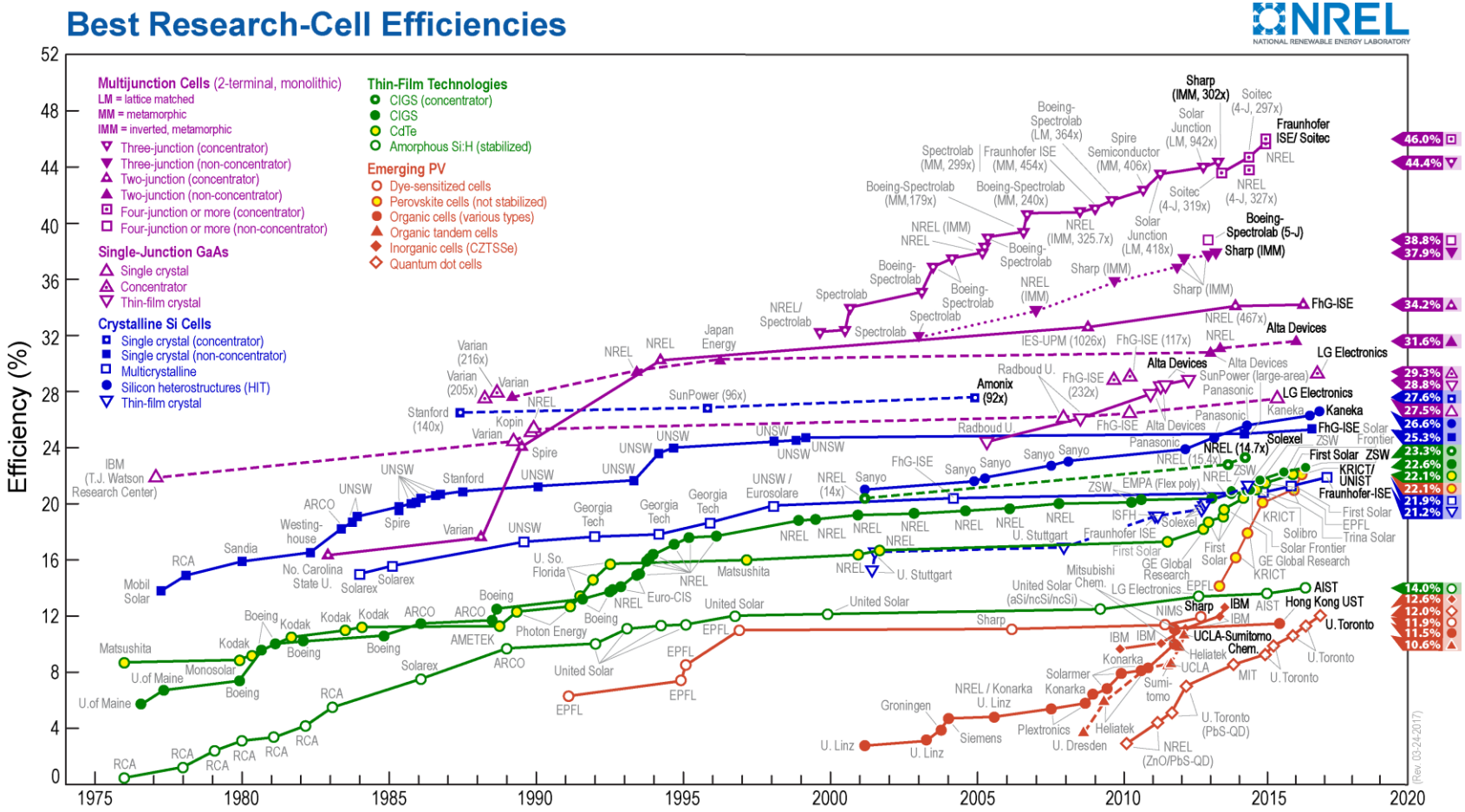

Figure 1.3. Chart of best research-cell efficiencies by year for various photovoltaic technologies.[15]

1.4 PN-JUNCTION PHOTOVOLTAICS

Due to a variety of factors including fabrication cost and efficiency, silicon PVs have become ubiquitous around the world. Thus it is worthwhile to briefly discuss the operating principle of a silicon PV device before addressing the physics behind OPVs. Silicon PVs are made by forming a junction between p-type and n-type silicon. A p-type material, while electrically neutral, contains an excess concentration of free holes, resulting in a Fermi level (E_F) that is closer to the valence band (VB). In silicon this is typically achieved by implanting trivalent impurities that ionize at room temperature. Conversely, an n-type material has an excess concentration of free electrons, with a Fermi level that is closer to the conduction band (CB). In silicon this is typically achieved by implanting pentavalent impurities that ionize at room temperature. When a p-type material comes into contact with an n-type material, excess free electrons from the n-side migrate to the p-side, and excess free holes from the p-side migrate to the n-side. The excess electrons (holes) that migrate across the junction recombine with majority holes (electrons). Charge migration occurs until equilibrium is reached, and the Fermi levels on the p- and n-side are aligned. This migration of charge across the junction creates a region on the p-side that is depleted of excess holes and a region on the n-side that is depleted of excess electrons. Since the depletion region is no longer electrically neutral, an electric field is established across the depletion region. This is shown schematically in Figure 1.4.

Figure 1.5 illustrates a pn-junction band diagram under short-circuit (equilibrium) and forward bias operation. The current density through a pn-junction can be described by the drift-diffusion equation

$$\begin{aligned} J_n &= J_n^{Drift} + J_n^{Diff.} = en\mu_n\varepsilon + eD_n\nabla n \\ J_p &= J_p^{Drift} + J_p^{Diff.} = ep\mu_p\varepsilon - eD_p\nabla p \end{aligned} \qquad [\mathrm{A\cdot m^{-2}}] \qquad (4)$$

where e is the elementary charge, n and p are the respective electron and hole concentrations, $\mu_{n,p}$ is the respective electron or hole mobility, ε is the electric field, and

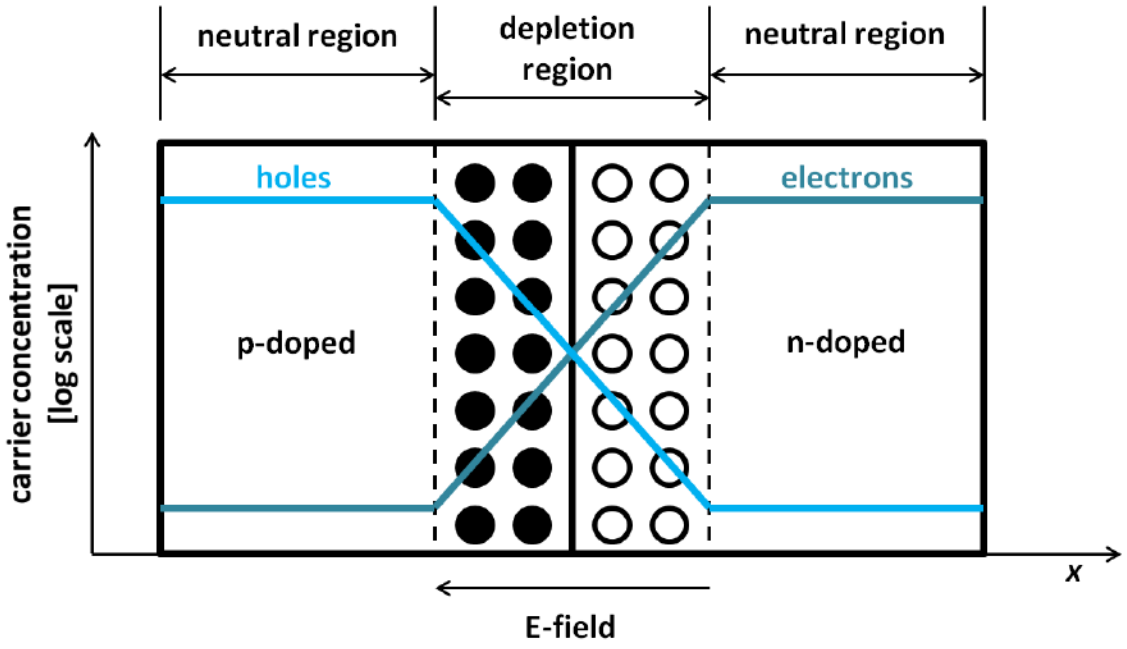

Figure 1.4. pn-junction under equilibrium, with indicated carrier concentrations. Electrons (solid circles) and holes (open circles) that have migrated to the depletion region are shown.

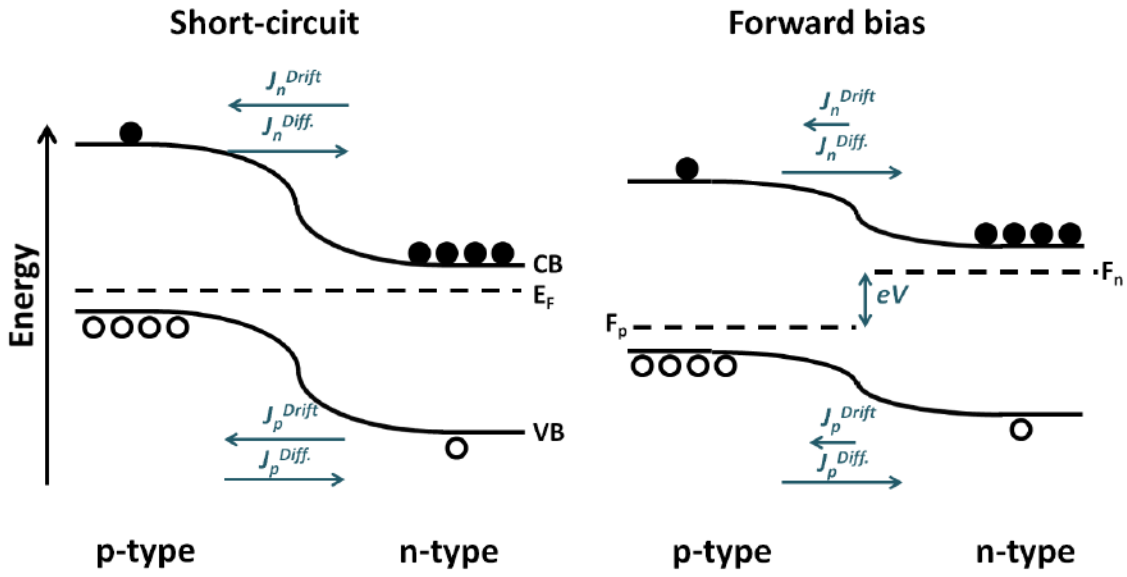

Figure 1.5. pn-junction under short-circuit (equilibrium) and forward bias operation. J_n and J_p are the electron and hole contributions to the current density, with *Drift* and *Diff.* denoting either drift or diffusion current densities. F_n and F_p are the quasi-Fermi levels of electrons and holes, respectively.

$D_{n,p}$ are the electron or hole diffusivities. Under short circuit conditions, the bulk p-side and n-side have neither an electric field nor a concentration gradient for current to flow. Although in the depletion region, an electric field and carrier concentration gradients provide drift and diffusion currents that are equal and opposite in magnitude, also resulting in net zero current.

When a positive bias is applied to the p-side, with respect to the n-side, the pn-junction is said to be under forward bias. This results in the splitting of the quasi-Fermi levels of holes (F_p) and electrons (F_n). It also reduces the magnitude of the electric field within the depletion region, since the applied field is in the opposite direction to the built-in field. With the electric field reduced, the drift current is also reduced, and the diffusion current becomes dominant, establishing a net current through the depletion region and injecting carriers into the bulk. This causes an increase in minority carrier concentration at the boundary between the depletion region and the bulk. However, the metal contacts on either side of the device ensure equilibrium and pull the excess minority carrier concentration back to zero. This carrier concentration gradient in the bulk region allows the diffusion current to continue through the device and be collected by the contacts.

Under illumination, photoexcited electrons and holes are created when the photon energy is larger than the bandgap. The band diagram for this situation is shown in Figure 1.6. Any photoexcited minority carriers that are generated within a minority carrier diffusion length of the depletion region can migrate there and be swept across by the electric field, increasing the drift current. The minority carrier diffusion length is the average distance a minority carrier can travel before recombining. In silicon PVs this length is limited by the density of trap states within the bandgap that act as recombination centers. Once across the depletion region they are injected into the bulk region as majority carriers, increasing the local carrier concentration and continuing through the device as a diffusion current.

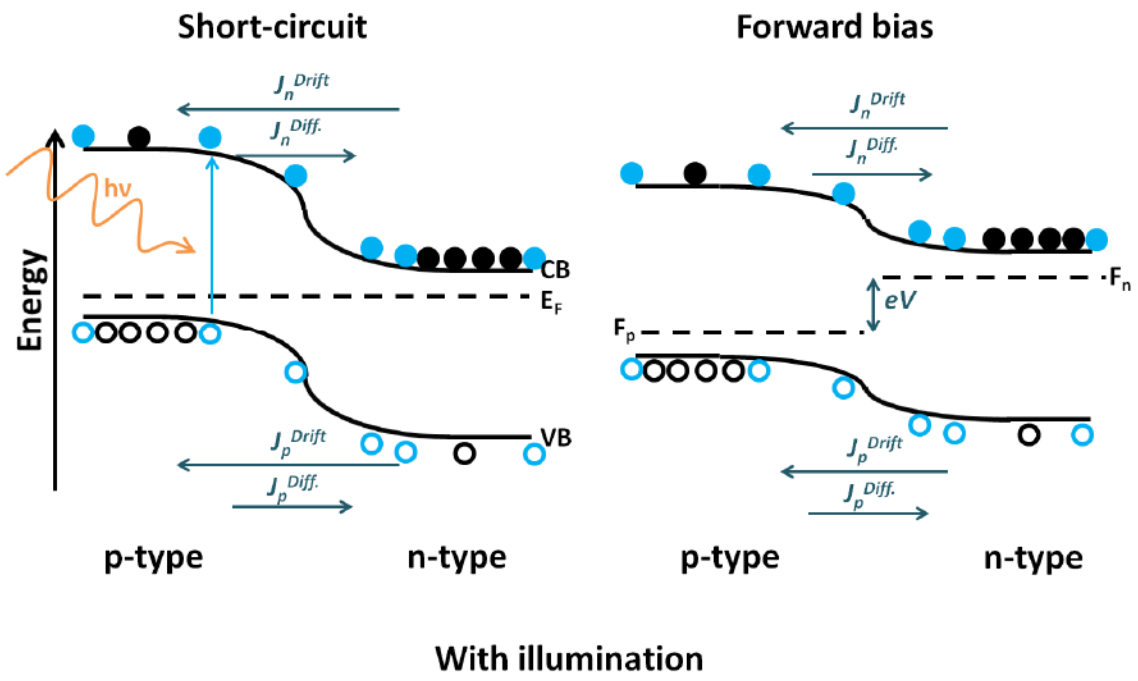

Figure 1.6. pn-junction under short-circuit and forward bias operation, while under illumination. For simplicity, the spatial dependence of quasi-Fermi levels of electrons and holes are not drawn. J_n and J_p are the electron and hole contributions to the current density, with *Drift* and *Diff.* denoting either drift or diffusion current densities. F_n and F_p are the quasi-Fermi levels of electrons and holes, respectively.

When a small forward bias is applied ($V_{app} < V_{oc}$), the reduction in electric field within the depletion region reduces the net current. However, since there is now a quasi-Fermi level separation of electrons and holes at the contacts, power is being supplied by the pn-junction. If the forward bias continues to increase, at some point the drift current will be reduced to the same magnitude as the diffusion current within the depletion region, and the net current through the device will go to zero. The bias at which this occurs is known as the open circuit voltage (V_{oc}). As the name suggests, applying an infinite load on a pn-junction under illumination will also result in the same measured potential across the device due to an accumulation of photoexcited carriers.

1.5 Organic Semiconductors

Organic semiconductors are conjugated molecules or polymers made from carbon, hydrogen, and various heteroatoms such as nitrogen, oxygen, and sulfur. Conjugated molecules are formed from alternating single and double bonds, with the former made from a σ-bond, and the latter a σ-bond and a π-bond. Figure 1.7 shows the simplest π-bonded molecule, ethylene. The electron configuration of carbon is $1s^2 2s^2 2p^2$, consisting of four valence electrons that participate in bonding interactions. The C-C σ-bond originates from a pair of electrons in overlapping sp^2 hybridized orbitals along the x-direction, with respect to the coordinates drawn in Figure 1.7. The π-bond originates from a pair of electrons in overlapping p-orbitals oriented along the z-direction. The four remaining C-H σ-bonds originate from pairs of electrons in C sp^2 orbitals overlapping with H 1s orbitals, and lie in the xy-plane.

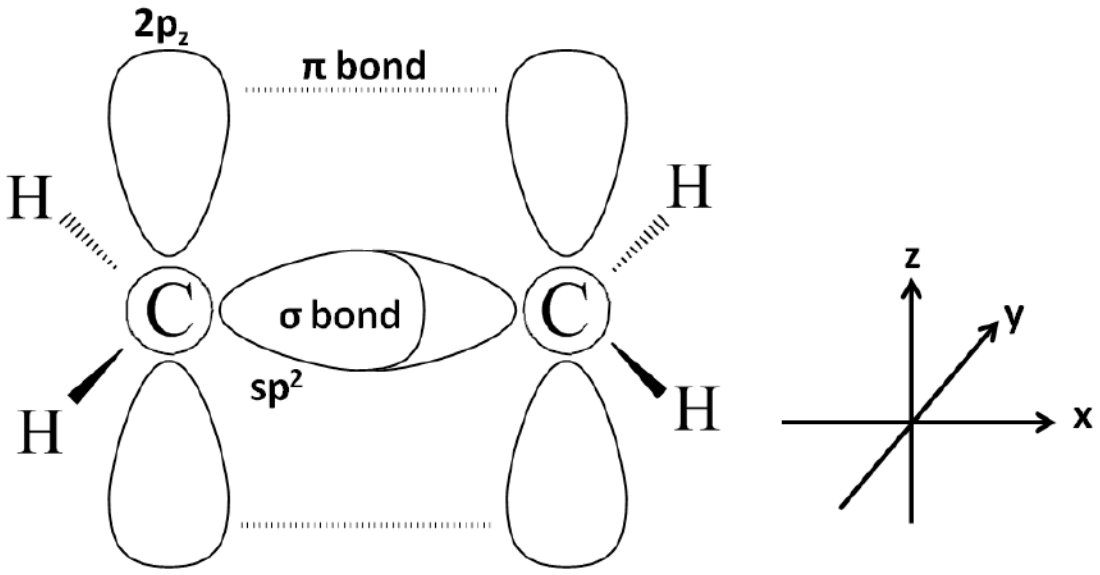

Figure 1.7. Orbital bonding configuration of ethylene, illustrating spatial orientation of σ- and π-bonds.

The molecular orbital energy diagram of ethylene is shown in Figure 1.8. The highest occupied molecular orbital (HOMO) of ethylene is the π-bonding orbital. The lowest unoccupied molecular orbital (LUMO) is the π-antibonding orbital. These two molecular

orbitals are the most important for both electronic transport and optical properties of organic semiconductors.

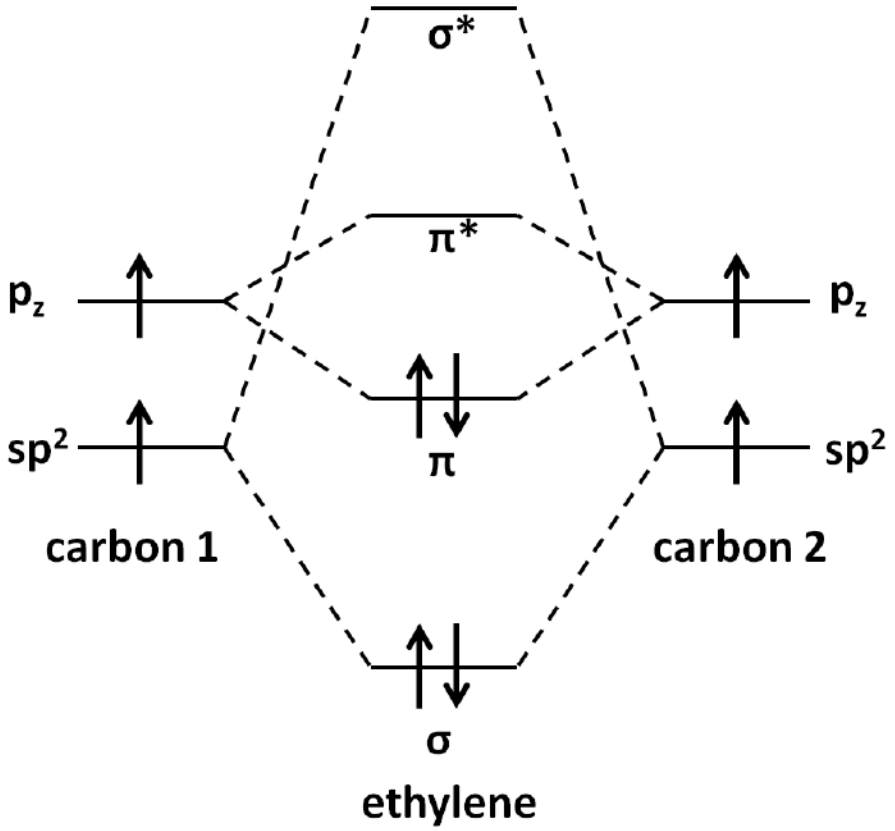

Figure 1.8. Molecular orbital energy diagram of ethylene. The HOMO consists of the π-bonding orbital, while the LUMO consists of the π-antibonding orbtal.

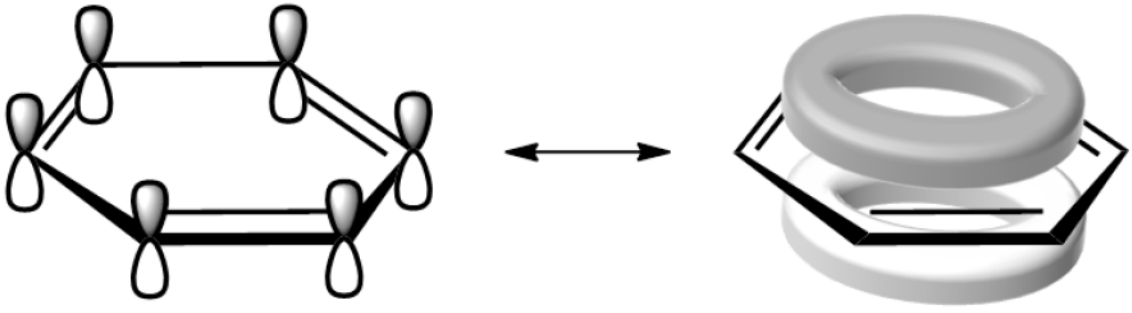

Figure 1.9. Symmetry of π-orbitals in benzene allows mixing between orbitals, resulting in delocalization of π-electrons around the conjugated structure.

In larger conjugated systems, mixing between adjacent π-orbitals allows π-electrons to delocalize over the spatial extent of the conjugated system. Figure 1.9 shows a larger conjugated molecule, benzene, with π-orbitals delocalized around the aromatic ring.

1.6 Electronic Transport in Organic Semiconductors

Organic solids consist of weak van der Waals interactions between neighboring molecules, with charge-transport properties strongly depending on the extent of electronic coupling between adjacent sites. The magnitude of this coupling depends on the matrix element

$$t_{12} = \langle \Psi_1 | H | \Psi_2 \rangle \tag{5}$$

where Ψ_1 and Ψ_2 are the wavefunctions of the two charge localized states, and H is the electronic Hamiltonian of the system. For two interacting molecules M_1 and M_2 with an excess charge, the states correspond to (M_1^+,M_2) and (M_1,M_2^+), or (M_1^-,M_2) and (M_1,M_2^-). The difficulty in determining electronic coupling parameters for organic solids lies in the weak interactions between neighboring sites. In traditional inorganic semiconductors, strong covalent bonds limit the degrees of freedom of lattice sites, such that electronic interactions dominate transport mechanisms. Electron-phonon interactions are relatively small and act as perturbations that account for scattering of delocalized carriers. Organic semiconductors however, have many vibrational degrees of freedom, such that electron-phonon interactions have been found to be comparable to or sometimes larger than electronic interactions.[22] In this case electron-phonon interactions lead to the formation of quasi-particles known as polarons, consisting of an electronic charge dressed by a phonon cloud.

The situation is further complicated by the dependence of electronic coupling on spatial orientation between adjacent molecules. This is illustrated in Figure 1.10, where two adjacent anthracene molecules are shown in two different packing arrangements. The fictional wavefunctions of the charge localized states (Ψ_1, Ψ_2, $\Psi_{1'}$, $\Psi_{2'}$) in this scenario

are expected to result in very different electronic coupling matrix elements due to the relative phase relationships between Ψ_1-Ψ_2, and $\Psi_{1'}$-$\Psi_{2'}$. This has been experimentally demonstrated by Diao *et al.*, who used a shear-casting technique to produce crystalline films with five different polymorphs of 6,13-bis(triisopropylsilylethylnyl)pentacene (TIPS-pentacene). Thin-film transistors made from these polymorphs exhibited hole mobilities ranging from 6 x 10^{-2} to 8 $cm^2 \cdot V^{-1} \cdot s^{-1}$.[23]

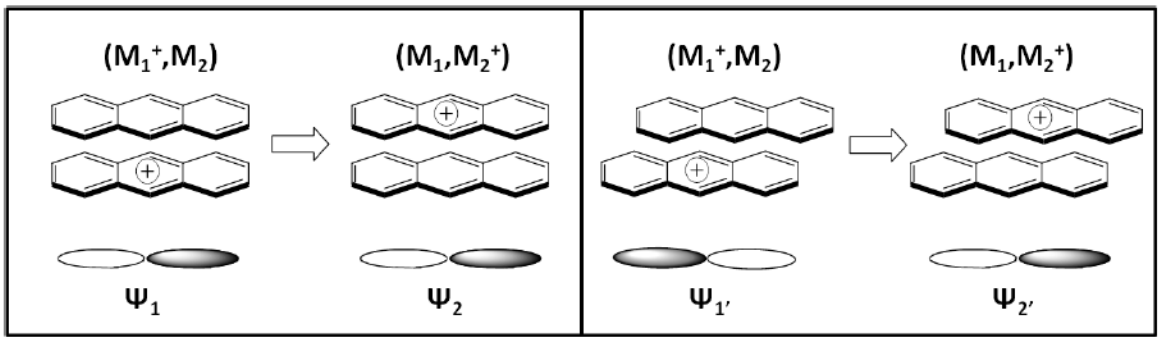

Figure 1.10. Fictional representation of the dependence of electronic coupling on spatial orientation. In the left panel Ψ_1 and Ψ_2 are the wavefunctions of the charge localized states (M_1^+,M_2) and (M_1,M_2^+), respectively, and are in phase with each other. In the right panel M_1 has been translated along the longitudinal axis of the molecule with respect to M_2, such that $\Psi_{1'}$ and $\Psi_{2'}$ are out of phase with each other. The dark and light lobes of Ψ_x represent the phase of the wavefunction.

Aside from the wide variety of crystalline packing motifs in organic semiconductors, semi-crystalline to amorphous morphologies are also common and depend on the size and shape of molecules, intermolecular interactions, and processing conditions. Furthermore, semiconducting polymers are able to transport charge using both interchain and intrachain mechanisms.

1.7 Organic Dyes and Pigments

Organic dyes (soluble) and pigments (insoluble) are organic semiconductors that absorb light in the visible to near-infrared spectrum. The part of the molecule or polymer responsible for the visible absorption properties is referred to as the chromophore. The

optical bandgap of organic chromophores originate from a HOMO to LUMO transition of π-electrons. In large, extended chromophores, symmetry relations between adjacent π-bonds allow orbital mixing to produce delocalized HOMOs and LUMOs that extend over the entire chromophore. The analogous toy model for these systems is a 2-dimensional particle in a box, where the energy spacing between modes is inversely proportional to the size of the box. Similarly, in an organic chromophore, the energy spacing between the HOMO and LUMO (adjacent modes) decreases as the size of the chromophore increases, or as the conjugation length increases. Since conjugated polymers can be infinitely long in theory, one would expect the optical bandgap to go to zero. In reality, there exists an effective conjugation length over which the π-electrons remain localized. This effective conjugation length requires overlap of p-orbitals orthogonal to the plane of conjugation. However, steric effects between adjacent polymeric units can lead to twisting of the polymer backbone, causing p-orbitals to misalign and reduce the effective conjugation length.

There are three strategies that are commonly used for synthesizing organic chromophores with optical bandgaps in the visible to near-IR spectrum. The first uses a single type of conjugated building block to form linear molecules or polymers. Two common examples are shown in the top row of Figure 1.11. This strategy is limited in its ability to tune the optoelectronic properties of these chromophores, however. The second strategy uses rigid, extended chromophores, with several examples shown in the middle row of Figure 1.11. This strategy is limited by the commercial availability of large, rigid building blocks, and by the more complex chemical reactions required to form macrocyclic compounds and tune their properties. The third strategy uses a combination of electron-poor and electron-rich building blocks to form push-pull chromophores. Two examples are shown in the bottom row of Figure 1.11. This strategy has a much larger representation in OPVs due to the simpler chemistry and relative ease of tuning optoelectronic properties.

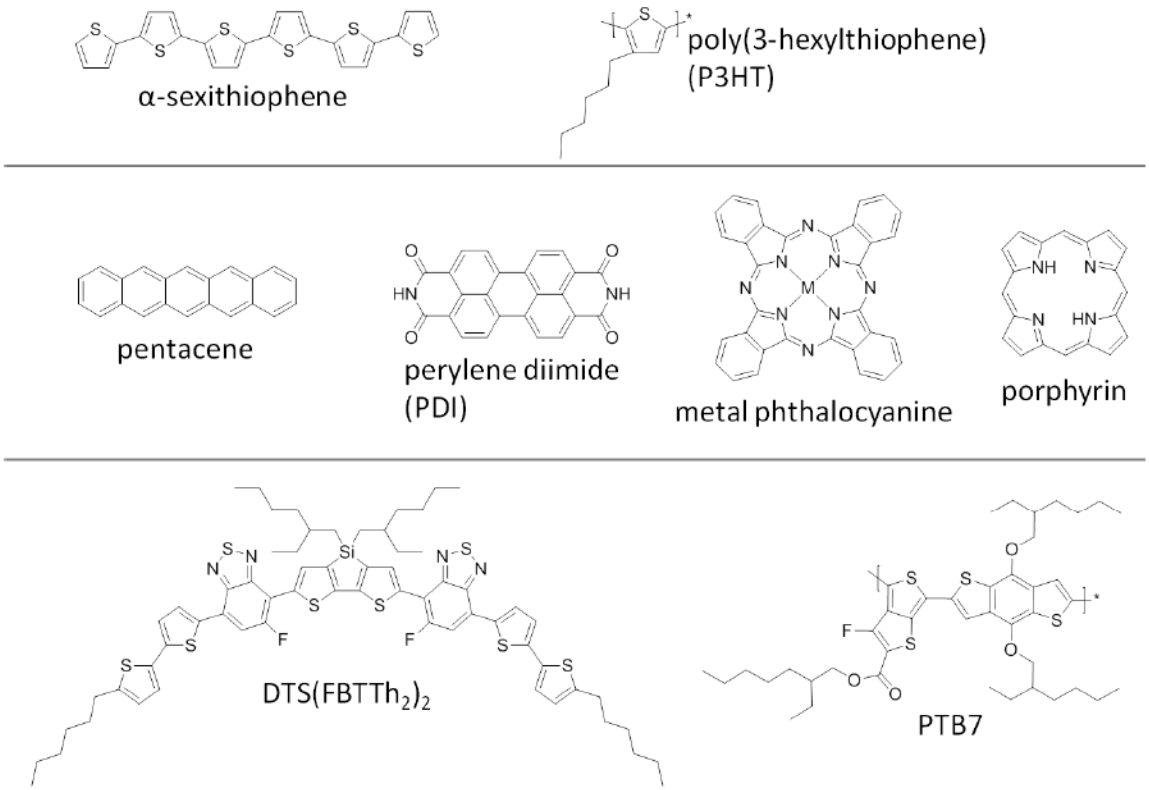

Figure 1.11. Example of organic dyes and pigments using linear chains of single building blocks (top row), rigid extended chromophores (middle row), and push-pull chromophores (bottom row). The plane of conjugation is coincident with the page, with π-orbitals extending above and below the page.

The concept of a push-pull chromophore is illustrated in the molecular orbital diagram in Figure 1.12. The chromophore in the center is made from joining phthalimide-thiophene-thiophene-phthalimide. The constituent building blocks are shown to the left and right of the central chromophore. Thiophene is considered to be electron-rich. The sulfur atom has two lone pairs of electrons. One pair extends in the plane of the molecule in a trigonal planar confirmation, occupying a sp^2 orbital. The other extends above and below the plane in a p orbital. Since the symmetry of this lone pair is the same as the π-orbitals that form the HOMO and LUMO of the molecule, they are able to donate electron density to the π-system, reducing the HOMO and LUMO binding energies. The HOMO and LUMO energy levels, shown for illustrative purposes, have been calculated using density functional theory (*vide infra* section 2.5). The lobes superimposed on the molecular structures are isocontours of the HOMO and LUMO wavefunction amplitudes

(electrons$^{1/2}$·bohr$^{-3/2}$), with different colors for the phase. Squaring the wavefunction amplitude corresponds to the electron probability distribution (electrons·bohr^{-3}). The HOMO of the central chromophore is largely derived from the HOMO of the electron rich building blocks, as indicated by the dashed lines.

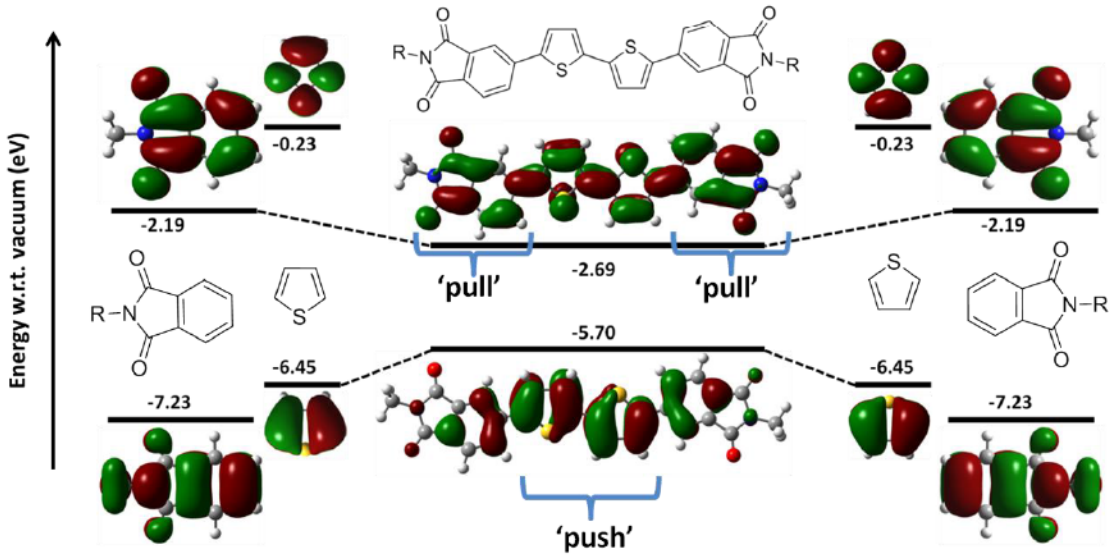

Figure 1.12. Molecular orbital diagram of a push-pull chromophore. The HOMO and LUMO energies and isocontours were calculated independently for the constituent phthalimide and thiophene components, as well as for the larger chromophore in the center, with Gaussian using density functional theory at the B3LYP/6-31G(d,p) level of theory. The HOMO and LUMO wavefunction isocontours can be interpreted as electron density. The HOMO of the central chromophore has more electron density localized on the thiophenes, while the LUMO of the central chromophore has more electron density distributed to the phthalimides.

Phthalimide is considered to be electron poor. The oxygen atoms also have two lone pair electrons each, however both are in a trigonal planar confirmation and do not have the same symmetry as the HOMO and LUMO orbitals. The main effect that oxygen has is due to its electronegativity, withdrawing π-electron density from the ring system through its double bond. This has the effect of increasing the HOMO and LUMO binding energies. The LUMO of the central chromophore is largely derived from the LUMO of the electron-poor building blocks. In the ground state, the central chromophore has most

of the π-electron density localized on the electron-rich components. Upon excitation, the electron-rich components 'push' electron density, while the electron-poor components 'pull' electron density, as can be seen by the redistribution of π-electron density in the LUMO of the central chromophore.

1.8 Organic Photovoltaic Devices

Photoconductivity in organic semiconductors was observed as early as 1910 in anthracene crystals.[24] However, since organic semiconductors are made from elements with low atomic numbers, the availability of polarizable charge is small, resulting in low dielectric constants. In the absence of charge screening, the Coulomb potential between the photoexcited electron and hole is large, leading to the formation of a Frenkel exciton. The exciton binding energies in organic semiconductors have been measured to be on the order of 0.4 - 1.4 eV,[25] significantly larger than the average thermal energy (k_BT) available at room temperature. Thus, unlike typical inorganic photovoltaic materials with exciton binding energies on the order of k_BT, the free carrier yield in neat organic materials is low. To overcome the large exciton binding energies and produce free charge carriers, a bilayer heterojunction was first implemented by Tang in 1986, achieving a PCE of 1 %.[26] This is shown schematically in Figure 1.13. In an organic heterojunction, an exciton will randomly hop between molecules until it reaches the donor/acceptor (D/A) interface or recombines. If it reaches the D/A interface, transfer of the excited electron from the electron-donating material to the electron-accepting material or transfer of the excited hole from the electron-accepting material to the electron-donating material is expected to take place when an energetically favorable state is available. The offset in energy between donor and acceptor HOMO levels, Δ_{HOMO}, for electron transfer, or the offset in energy between donor and acceptor LUMO levels, Δ_{LUMO}, for hole transfer, should be larger than the exciton binding energy.

Immediately upon transfer across the interface, the electron on the acceptor material and the hole on the donor material form a charge-transfer (CT) exciton. This CT exciton still experiences a Coulomb potential that has been measured to be on the order of 0.2 – 0.4

eV.[27,28] From the CT state, the electron and hole can either recombine or separate into free charge carriers. There has been some debate about the exact nature of charge separation at the D/A interface. Initially it was proposed that upon transfer to the CT state, the CT exciton would be in a vibrationally excited state, allowing this 'hot' exciton to overcome the CT exciton binding energy.[27] However, Lee *et al.* demonstrated that excitation directly into the CT state without excess energy had the same free carrier yield as above-bandgap excitation of the donor material.[29] Vandwal *et al*. further generalized this result to eight high-performance OPV systems with energy-independent carrier yield,[30] indicating that 'hot' CT excitons thermalize to the lowest vibrational state on time scales of less than 1 ps before separating into free carriers.[28] In lieu of 'hot' excitons, there is evidence that suggests CT states are delocalized over many molecules, allowing electron and holes to access band-like states that aid in charge separation.[31] However, conclusive experiments have yet to unambiguously confirm this model.

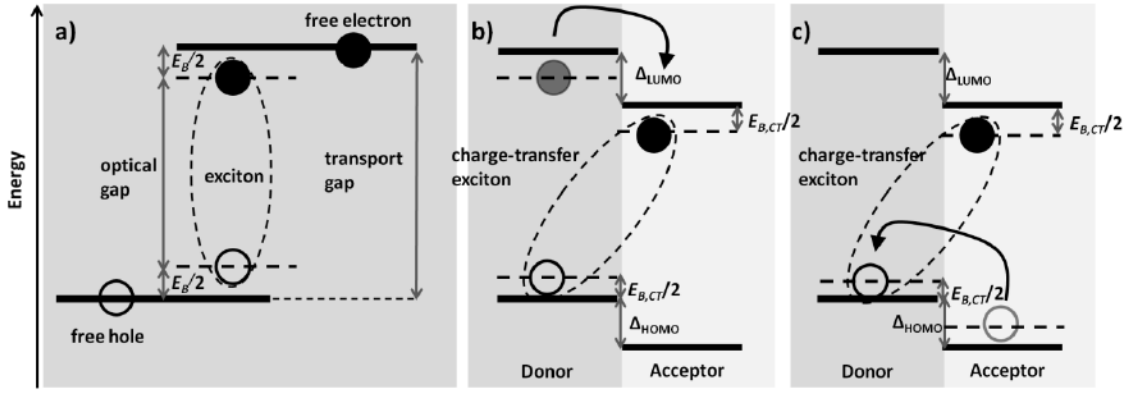

Figure 1.13. Energy level diagram showing a) the difference between an optically excited exciton and free charge carriers, b) electron transfer from an excited donor to an acceptor, and c) hole transfer from an excited acceptor to a donor. E_B is the exciton binding energy, $E_{B,CT}$ is the charge-transfer exciton binding energy, and Δ_{LUMO} and Δ_{HOMO} are the energy offsets between donor and acceptor LUMO and HOMO levels, respectively.

Since the advent of the organic heterojunction, two main fabrication techniques have been utilized. Thermal evaporation under vacuum was initially used to make bilayer devices. The drawback of the bilayer device is that the thickness of donor and acceptor layers is limited by the exciton diffusion length, typically measured to be around 10

nm,[32,33] however this value has been shown to be highly dependent on crystallinity, with single-crystal diffusion lengths generally being 3-4 times larger.[34] The requisite film thickness for an optical density of one is approximately 100 nm. To make thicker evaporated devices capable of absorbing more light, co-evaporation of donor and acceptor materials has been used to form quasi-bulk heterojunction devices with three dimensional, interconnected grains.[35] More complex trilayer schemes utilizing long-range Förster resonant energy transfer, where an excited chromophore transfers the excitation to another chromophore initially in the ground state through non-radiative dipole-dipole coupling, have also resulted in high PCE devices.[36]

The other dominant fabrication technique utilizes solution processing and spin coating to form bulk heterojunctions (BHJs). In a BHJ, donor and acceptor dyes are dissolved into a common solvent. The solution is spin-cast onto a device substrate, where the donor and acceptor dyes undergo spontaneous phase separation while the film dries. Under optimal casting conditions, donor and acceptor domain sizes are comparable to the exciton diffusion lengths, and most excitons reach a D/A interface.

In both evaporated and solution-processed devices, tandem architectures can be made by stacking multiple heterojunctions. These device architectures are shown schematically in Figure 1.14. Note that standard architectures are shown, with the light entering the hole-selective contact. Inverted architectures, with the light entering the electron-selective contact are also commonly made. In PV devices, the designation of anode and cathode follows the same convention as a diode, even though the photocurrent flows in an opposite direction to the current through a diode under forward bias.

1.9 Non-Fullerene Acceptors

The vast majority of solution-processed BHJ OPVs utilize either a C_{60} or C_{70} fullerene derivative as the acceptor material. Figure 1.15 shows the progression of high-performance solution-processed BHJ OPV systems reported until 2012, prior to the beginning of the work presented in this dissertation.

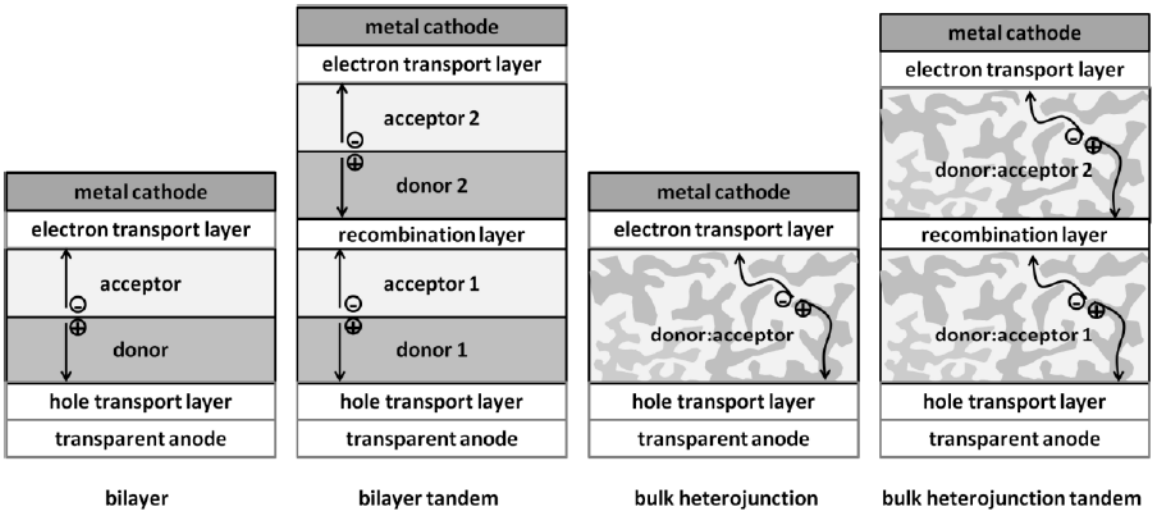

Figure 1.14. Schematics of OPV device architectures. Arrows indicate the directions of travel of photoinduced electrons and holes. Note in bulk heterojunctions, percolation paths to the anode and cathode are required for donor and acceptor domains, respectively, for separated charges to be collected.

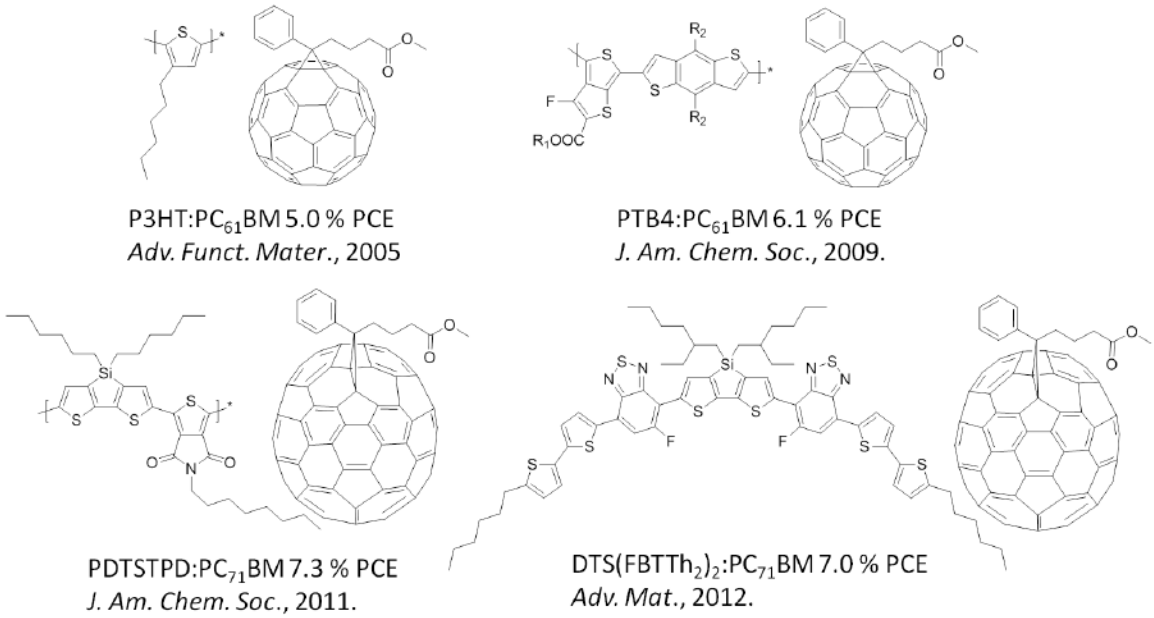

Figure 1.15. High performance solution-processed bulk heterojunction OPV systems utilizing fullerene acceptors prior to 2012.[37–40]

Fullerenes are unique conjugated materials, in that their spherical shape allows the π-orbitals to wrap around the molecules in a spherical shell. This allows for nearly isotropic charge transport to occur between neighboring fullerenes, as opposed to the requisite π-stacking in planar molecules. The small lateral dimensions (~ 1 nm) also allow many fullerene derivatives to intercalate between polymer chains and form intimately mixed heterojunctions.[41] The weaknesses of fullerenes relate to their relatively weak absorption in the solar spectrum and their synthesis. Figure 1.16 shows the absorption of $PC_{61}BM$, a commonly used soluble fullerene derivative, plotted against the AM1.5G spectrum. It is desirable for both the donor and acceptor components to have strong, complementary absorption within the solar spectrum. In terms of synthesis, fullerenes are predominantly made by burning aromatic hydrocarbons. The low yielding synthesis and solvent-heavy purification leads to an embodied energy 10-100 times greater than most organic dyes currently in use.[42,43] The few known chemical synthetic methods for producing fullerenes have so far been shown to be less economically viable.[44]

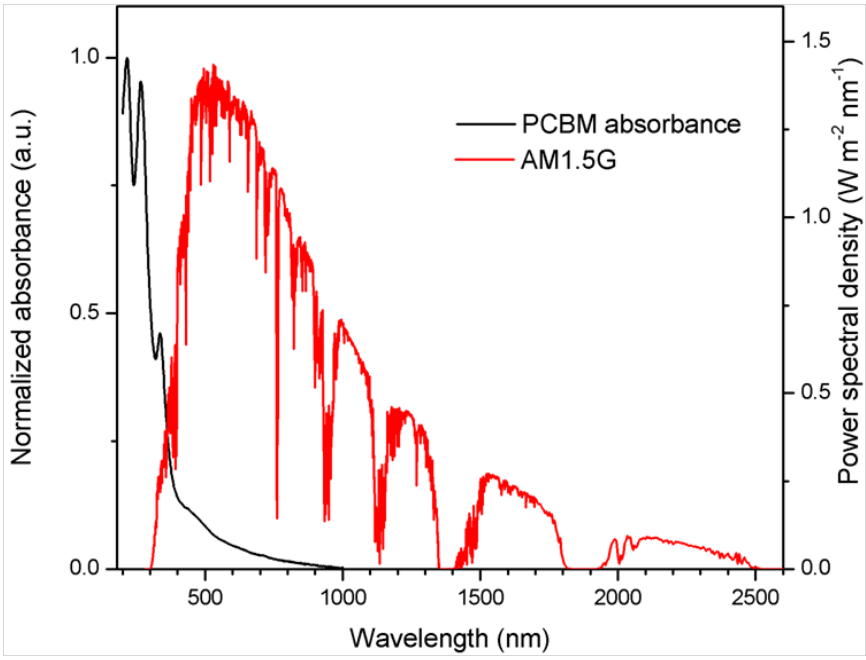

Figure 1.16. Absorbance of $PC_{61}BM$ compared to the AM1.5G spectrum.

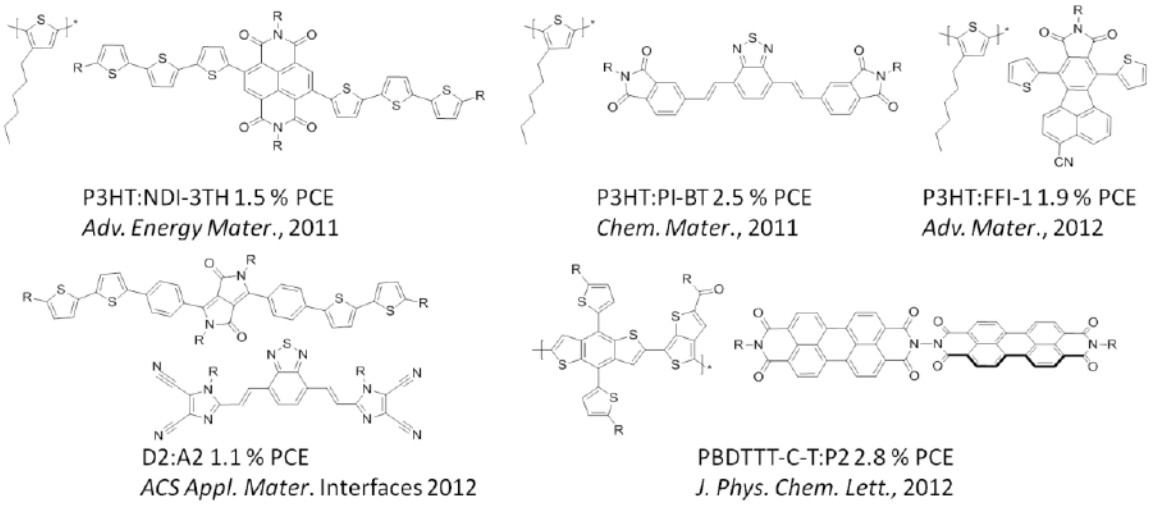

Figure 1.17. Best-performing solution-processed bulk heterojunction OPV systems utilizing non-fullerene acceptors prior to 2012.[45–49]

Due to the inherent drawbacks of fullerene acceptors, recent interest has been focused on the development of non-fullerene acceptors. Figure 1.17 shows some of the best-performing OPV systems utilizing non-fullerene acceptors reported until 2012. Note that the overall PCEs of these systems are significantly less than those of fullerene systems developed in the same era, that are presented in Figure 1.15.

1.10 Thesis Goals and Outline

The main goals of this thesis are to investigate the integration of novel small-molecule non-fullerene acceptors into solution-processed BHJ OPVs. The ideal non-fullerene acceptor candidate will fulfill the following criteria:

- Strongly absorbing in the solar spectrum
- Electron mobility of at least 10^{-2} $cm^2 \cdot V^{-1} \cdot s^{-1}$
- Large ionization energy and electron affinity to drive charge separation at the donor/acceptor interface
- Made in high yield in a low-cost synthesis

These criteria are discussed in more detail in Chapter 3. This work has been undertaken in collaboration with the Welch research group formerly at Dalhousie University and currently at the University of Calgary, who synthesized the non-fullerene acceptors.

Chapter 2 presents the relevant experimental methods used in fabricating and characterizing OPV devices and materials.

Chapter 3 presents the device performance and characterization of a family of related push-pull chromophores utilizing phthalimide and naphthalimide end-groups.

Chapter 4 presents the device performance and characterization of rigid, extended chromophores utilizing perylene diimide moieties.

Chapter 5 makes some concluding remarks about the work carried out in **Chapters 3** and **4**, and presents some initial work on utilizing a nanoembossing technique for fabricating solution-processed OPVs.

Chapter 6 discusses some possible future directions for the progression of this work.

CHAPTER 2 EXPERIMENTAL METHODS

This chapter outlines the experimental methods use to fabricate and test organic thin-films transistors (TFTs), and OPVs. Ultraviolet photoelectron spectroscopy (UPS), atomic force microscopy (AFM), and density functional theory (DFT) are also described in this chapter.

2.1 THIN-FILM TRANSISTORS

Throughout the work presented in this dissertation, TFTs were fabricated to measure charge carrier mobilities of neat materials. A schematic of the TFTs used in this dissertation is shown in Figure 2.1.

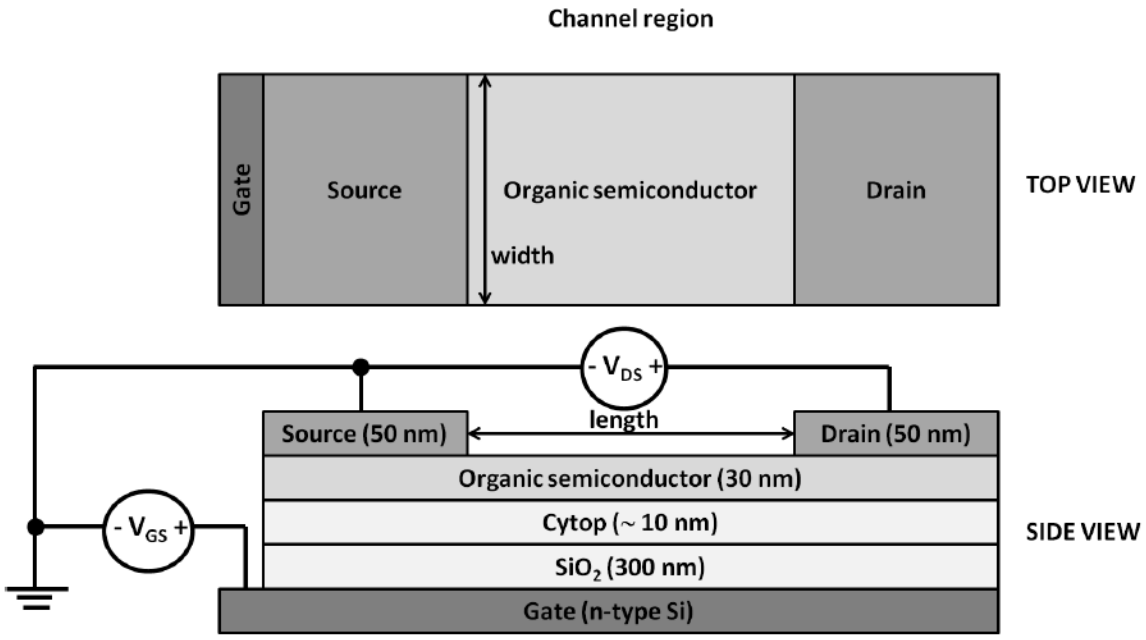

Figure 2.1. Schematic of TFTs used in this dissertation.

In the TFT configuration shown above, the field effect mobility can be measured by applying a bias between the drain and source, and sweeping the bias between the gate and source. When a positive bias is applied to the gate, electrons from the source contact will populate the channel region at the organic-dielectric interface, forming an n-channel. Conversely, a negative bias will create a p-channel with holes from the source. The

number of charge carriers per unit area in the channel is defined by the gate-source bias (V_{GS}), and the capacitance per unit area of the dielectric, C_{ox}. Applying a bias between the drain and source (V_{DS}) will cause charge carriers to flow from the source to the drain. A positive V_{DS} is used for n-channel devices, whereas a negative V_{DS} is used for p-channel devices. Depending on the relative magnitude of the biases, there are various operating regimes for TFTs. In an ideal TFT, the device is said to be in saturation mode when $|V_{GS}| > |V_t|$ and $|V_{DS}| > |V_{GS} - V_t|$, where V_t is the threshold voltage for populating the channel with free charge carriers. Under these conditions, it can be shown that the current from the drain to the source is given by

$$I_D = \frac{1}{2}\mu \cdot C_{ox} \cdot \left(\frac{W}{L}\right) \cdot (V_{GS} - V_t)^2 \qquad [\text{A}] \qquad (6)$$

where μ is the charge-carrier field-effect mobility, and W and L are the width and length of the channel. Typically, $I_D^{1/2}$ is plotted against V_{GS} and a linear fit is used to determine both μ and V_t, when C_{ox}, W, and L are known. An example of a saturation-transfer curve for an n-channel TFT is shown in Figure 2.2.

The TFTs presented in this dissertation were made on heavily doped n-type silicon wafers (arsenic doping, $\rho < 0.035$ Ω·cm) with 300.0 nm of thermal SiO_2. The wafers were cut into coupons approximately 5 x 15 mm in size. Silicon wafers are typically clean when purchased and only require ultrasonication (10 minutes) in ethanol, drying with compressed air, followed by UV-ozone treatment for 20 minutes. Since SiO_2 is known to form electron traps at the surface, Cytop (amorphous fluoropolymer; Asahi Glass) dielectric was coated on top of the SiO_2.[50] The Cytop dielectric coating was prepared by spin-coating 3 parts Cytop CTL-809 M dissolved in 14 parts CTSolv-180 at 5000 rpm for 60 s on top of the SiO_2. Following dielectric preparation, the samples were transferred to a vacuum deposition system (base pressure 10^{-6} mbar). 30 ± 3 nm of organic semiconducting material was deposited through a stencil mask at 0.02-0.05 nm·s^{-1} onto the coupons held at 100 ± 2 °C. The thicknesses of all vacuum-deposited materials were determined using a quartz crystal microbalance deposition monitor. The samples were

allowed to cool to < 40 °C before vacuum was broken, and a source-drain stencil mask was aligned with the active semiconductor. Aluminum (n-channel) or gold (p-channel) source-drain contacts were deposited at a rate of 0.1 $nm \cdot s^{-1}$ to a thickness of 50 ± 1 nm. Each coupon contained an array of 24 transistors with channel lengths ranging from 25 ± 10 μm to 250 ± 10 μm, and channel widths between 500 ± 10 μm and 1500 ± 10 μm. The larger channel dimension devices were used due to the lower relative uncertainty in device area. After metal deposition, the samples were briefly exposed to air again for a few minutes before transferring to an Ar-filled glove box for testing. Two Kiethley 236 source-measure units were used to measure the current-voltage characteristics of the devices.

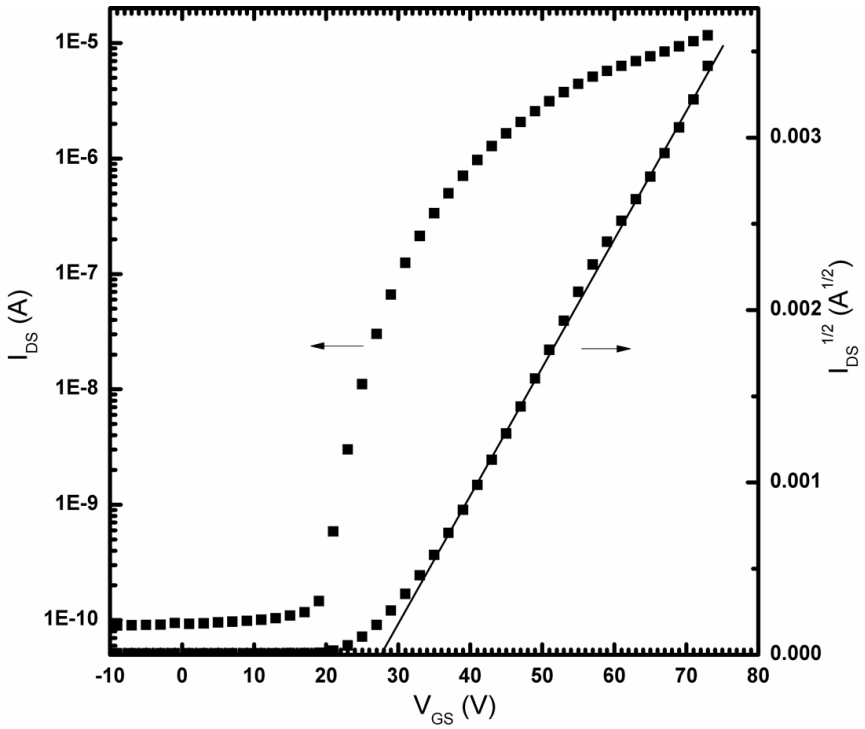

Figure 2.2. Sample n-channel TFT saturation-transfer curve, showing the drain current as a function of gate-source bias. The drain current is plotted on a log scale on the left axis. The square root of the drain current is plotted on the right axis.

In addition to TFT devices, capacitors were fabricated by depositing metal electrodes through a stencil mask directly on top of the Cytop dielectric. This allowed the specific

capacitance to be measured using an LCR meter, which was found to be 10.7 ± 0.1 $nF \cdot cm^{-2}$ for frequencies between 100 Hz to 100 kHz, independent of frequency within experimental uncertainty. Given the dielectric constant reported by the manufacturer of Cytop to be 2.1, this is consistent with a Cytop thickness of 12 nm.

2.2 Organic Photovoltaic Devices

The fabrication of solution-processed OPV devices is a complicated procedure, with the light-absorbing dye layer being the most critical component. To properly account for the criteria used in making and testing OPV devices, this section will first give a general overview of fabrication, followed by spin-coating of organic bulk heterojunction films, and finally describe the testing of devices.

2.2.1 General Overview of OPV Device Fabrication

Organic photovoltaic devices presented in this dissertation were made on top of patterned indium tin oxide (ITO) coated glass (Thin Film Devices, R_s ~ 15-20 Ω/□). The glass substrates were 25 x 25 mm in area and 1.1 mm thick, with approximately 100 nm of ITO. The ITO substrates were first cleaned with Sparkleen detergent in Nanopure deionized (DI) water using a toothbrush. This was done to mechanically remove any grease or dust particles. The substrates were then ultrasonicated (10 minutes each) in detergent/DI water, DI water twice, acetone, and ethanol. After ultrasonication the substrates were blown dry with compressed air and then underwent 20 minutes of UV-ozone treatment.

In the next fabrication step, either a hole- or an electron-selective transport layer was applied. In standard architecture devices, the transparent electrode (ITO) is the hole-extracting contact (anode). The material used for hole-selective transport is a two component mixture of poly(3,4-ethylenedioxythiophene) and polystyrene sulfonate (PEDOT:PSS, Clevios P VP AI 4083). This hole-transporting polymer mixture is

purchased as a microdispersion in water. Prior to deposition, the PEDOT:PSS microdispersion was first filtered through a 0.45 μm hydrophilic polypropylene syringe filter. Next the PEDOT:PSS microdispersion was spin-cast in air on the clean substrates at 4000 rpm, followed by annealing on a hotplate at 150 ± 2 °C for 60 minutes. The annealing temperature was chosen in accordance with instructions from Clevios. Since PEDOT:PSS films are known to be hygroscopic when cool,[51] the substrates were annealed in a glass petri dish with a cover placed ajar, to prevent dust from depositing without trapping water vapor. Once removed from the hotplate the petri dish was wrapped in aluminum foil and transferred to a N_2-filled glovebox while hot.

For inverted architecture devices, the ITO (cathode) was coated with ZnO prepared from sol-gel solution. Zinc acetate dehydrate (Sigma Aldrich) was dissolved in 2-methoxyethanol (100 $mg \cdot mL^{-1}$) with ethanolamine added as a stabilizer (2.8 % v/v).[52] The ethanolamine acts as a coordinating ligand to the zinc ions, preventing zinc hydroxide precipitates from forming.[53] The ZnO solution was spin-cast in air on the clean substrates at 4000 rpm, followed by annealing on a hotplate at 200 ± 2 °C for 60 minutes.

Solutions of organic dye mixtures were spin-cast in a N_2-filled glovebox. The dye solutions typically have concentrations in the range of 15-40 $mg \cdot mL^{-1}$ in organic solvents. Solutions were either maintained at room temperature or were heated when the dye solubilities were low. All solutions were filtered through a 0.45 μm PTFE syringe filter prior to spin-casting at speeds of 1000-3000 rpm. The active layers were often annealed on a hotplate after casting. For all devices presented in this dissertation, the annealing time was fixed at 10 minutes, while temperatures may vary.

In standard architecture devices, the next layer deposited is either an electron-transport layer or a low work function contact. In this work, the electron-transport layer used was an amino-substituted perylene diimide (PDIN) molecule spin-cast from 1.5 $mg \cdot mL^{-1}$ in methanol with 0.15 % v/v acetic acid, at 3000 rpm.[54] PDIN is shown is Figure 2.3.

For inverted devices, the hole-transport layer was vacuum-deposited MoO_3 (15.0 ± 0.1 nm), deposited at a rate of 0.02 – 0.05 nm·s^{-1}. The thicknesses of all vacuum-deposited materials were determined using a quartz crystal microbalance deposition monitor. At this point, the active layers have either been coated with a uniform charge-transport layer, or the active layer is uncovered if calcium is to be deposited as a low work function contact. Since calcium is a highly reactive metal, it must be deposited just prior to top-metal contact deposition without breaking vacuum. Just prior to loading the devices into the vacuum deposition chamber, the material covering the ITO where the common electrode is located must be scraped away. A few scratches with tweezers are sufficient for the common electrode to contact the ITO. The top metal contacts (aluminum or silver), or a thin calcium layer (15.0 ± 0.1 nm at 0.02 – 0.05 nm·s^{-1}) followed by a thicker, more stable metal were deposited through a shadow mask at a rate of 0.1 nm·s^{-1} to a thickness of 100 ± 1 nm. All top metal contacts were deposited in a vacuum chamber directly connected to an Ar filled glovebox. After contact deposition the devices were transferred into the glovebox without air exposure where they underwent current density-voltage testing while under illumination. Figure 2.4 shows the top-view schematic of the devices at various stages of fabrication. Figure 2.5 shows the side-view schematic of the three device configurations used in this dissertation.

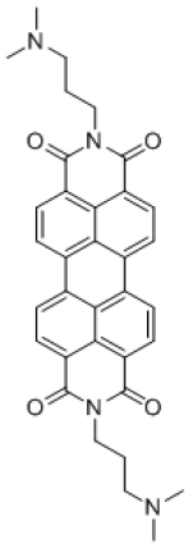

Figure 2.3. Chemical structure of PDIN.

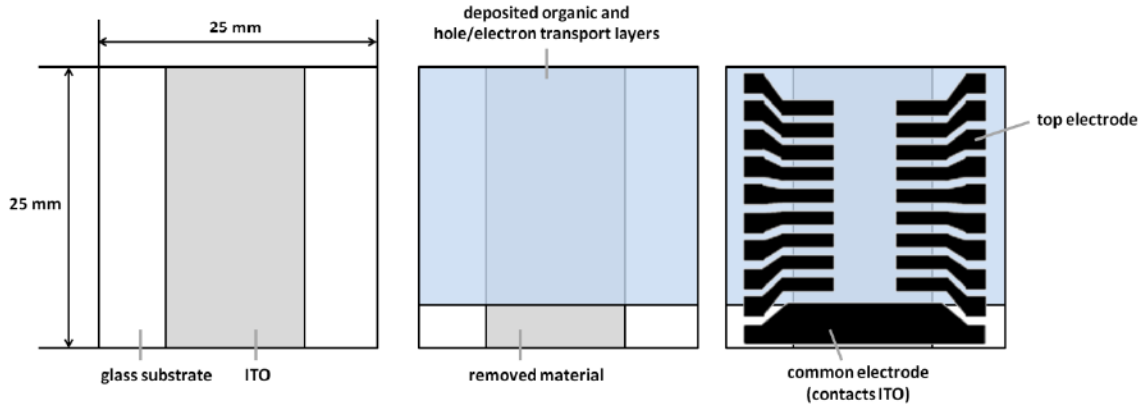

Figure 2.4. Top-view schematic of OPV devices. The dimensions of each device are determined by the area of overlap of the ITO and top electrode, corresponding to 3.3 ± 0.2 mm^2.

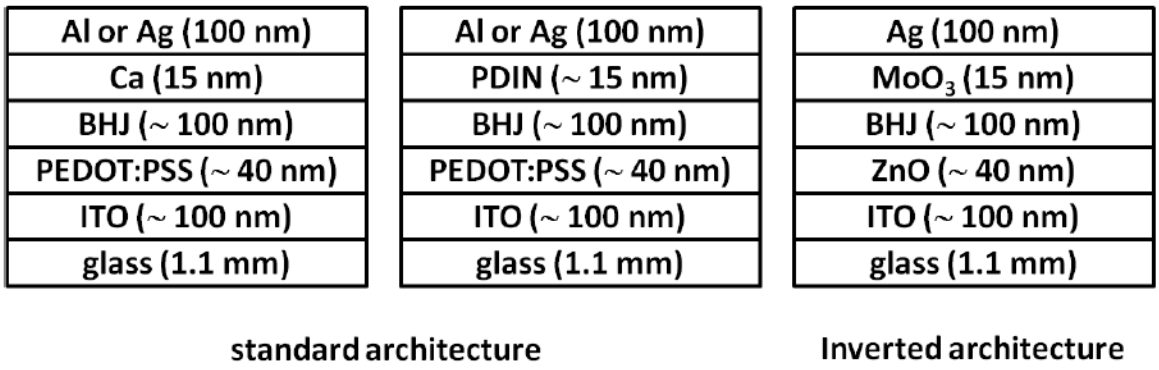

Figure 2.5. Side-view schematic of OPV devices used in this dissertation. The two standard architecture devices shown on the left use a hole transport material (PEDOT:PSS) while the inverted architecture device on the right uses an electron transport material (ZnO) to contact the ITO-coated glass substrate. The bulk heterojunction (BHJ) layer is comprised of a mixture of donor and acceptor dyes cast from a single solution. Either a low work function metal contact (Ca) or an electron transporting material (PDIN) is deposited on top of the BHJ in standard architecture devices, while MoO_3 is deposited as a hole transport material in inverted architecture devices. Al or Ag is used to cap the device and serve as the top contact.

2.2.2 Spin-Coating Organic Bulk Heterojunction Films

The light-absorbing layer in an OPV device is the most critical layer for device performance. The morphology of this layer depends heavily on the processing parameters used to cast the film. In a bulk heterojunction, macroscopically-uniform transparent films with nanoscale domain sizes are the ultimate goal. However, achieving this goal is

usually not an easy task. To begin with, the donor and acceptor dyes need to be soluble in a common solvent. There are a range of organic solvents such as chloroform, chlorobenzene, 1,2-dichlorobenzene, and *o*-xylene that are commonly used. In this dissertation, novel non-fullerene acceptors have been blended with commercially available donors. Since the donor materials are widely used, the solvents that will likely give the best results can be narrowed to one or two candidates. After a solvent has been chosen, the total dye concentration needs to be determined. It is instructive at this point to understand how spin coating works before proceeding. Figure 2.6 shows the four steps that take place when spin-coating. In the first step, the filtered dye solution is pipetted onto the substrate. The volume of deposited solution should be adjusted such that the droplet encircles the total device area. On the substrates used in this dissertation the deposited volume varies between 70-150 µL, and depends on solution viscosity and wetting properties. Immediately after depositing the solution, the spin-coater chuck needs to be ramped up to full speed. All spin-coater recipes used in this dissertation accelerate to full speed within 1 s. The amount of time between depositing the solution and getting the chuck spinning should be less than ~ ¼ s, and is more critical for hot solutions since the substrate is at room temperature and the dyes will begin to precipitate if left sitting too long. This is easier to achieve when the spin cycle is started with a foot pedal.

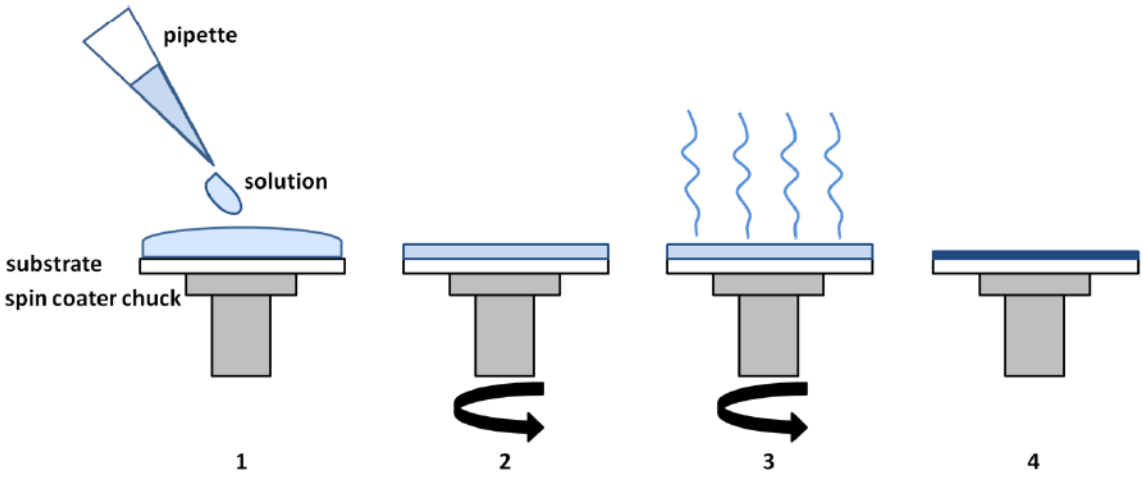

Figure 2.6. Spin-coating dye solutions. 1. The dye solution is deposited onto the substrate using a pipette. 2. The substrate is rotated at a few thousand rpm. 3. The host solvent evaporates. 4. The compact dye film is formed.

In the first second after the substrate starts spinning, the solution will thin to a few μm. In the next 10-100 s, the thinned fluid evaporates and the film dries. For higher boiling point solvents such as chlorobenzene, the thinning and evaporation occur in two distinct stages. For lower boiling point solvents such as chloroform, evaporation and thinning occur on comparable time scales, resulting in much thicker final films for the same dye concentrations. For a constant viscosity, the final film thickness t varies as

$$t \propto \frac{c}{\sqrt{\omega}} \quad [\mathrm{m}] \tag{7}$$

where c is the solution concentration, and ω is the spin speed.

As a starting point, the spin speed is usually set to 1000 rpm, and the total dye concentration is adjusted to achieve a desired optical density, typically around 20 $mg \cdot mL^{-1}$. However, dyes that are more crystalline tend to over-phase-separate during the film drying process, forming donor and acceptor phases that are significantly larger than an exciton diffusion length. This can easily be seen by eye as the film will be opaque due to light scattering from crystalline domains. With macroscopic phase separation, a common remedy is to increase both the solution concentration (thicker film) as well as the spin speed (thinner film) to maintain the final film thickness. Since the solvent:dye ratio in the solution is lower, the film dries quicker, giving the materials less time to phase separate. Once macroscopic phase separation has been remedied and the total dye concentration and spin speed determined, a series of devices with varying weight ratios of the donor and acceptor are made. The best performing weight ratios are then selected to move on to the next stage of optimization.

At this stage, if microscopic phase separation as observed by an optical microscope is evident, the casting conditions need to be adjusted to further drive domain sizes to the nanoscale. If microscopic phase separation is not evident, then thermally annealing films may increase performance as it drives crystallinity, enhancing charge carrier and exciton diffusion lengths. An alternative to thermal annealing, the addition of high boiling-point

solvent additives can be used to enhance crystallinity in cast films. A few of the more commonly used additives are shown in Figure 2.7.

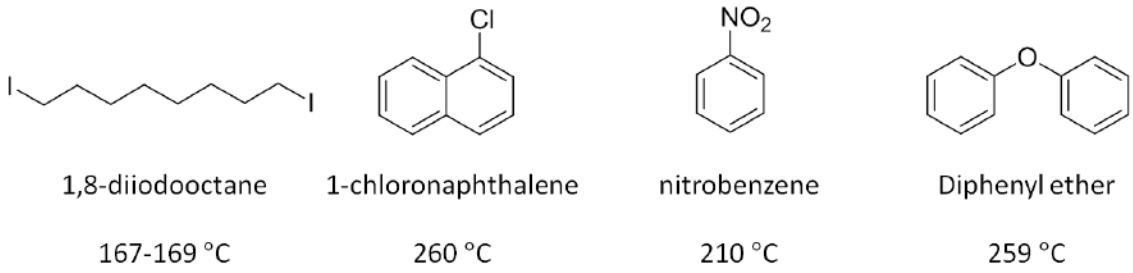

Figure 2.7. Commonly used high boiling-point solvent additives and their boiling points.

Solvent additives usually account for 0.2-4 % v/v of total solvent, and tend to be on the higher end for polymer donors as opposed to small molecules. During the film drying process, the solvent additives evaporate slower than the host solvent, enriching the solvent with additive. The role of the additive depends on the solubility of the donor and acceptor dyes in the additive-enriched solvent. Some additives are good solvents for both donor and acceptor dyes, allowing the film to dry slower. This can be beneficial for some polymer/fullerene systems because it allows the polymer more time to crystallize, while allowing the fullerene to intercalate between the polymer chains. Some additives are good solvents for one dye, while being poor solvents for the other. Other additives are poor solvents for both dyes. In the case of the additive being a poor solvent, this can cause one or both dyes to precipitate faster, acting as a nucleating agent for a larger number of grains of smaller size. The exact mechanisms of the additives are difficult to predict, and a variety are often tested. Furthermore, due to the low vapor pressure of these additives, even after the film is nominally dry some of the additive remains in the film until the devices are placed under vacuum for top metal contact deposition.[55] As long as the additive remains in the film, it can cause changes to the morphology. For this reason, all active layers were allowed to rest in multiwell containers, covered but with the

lid ajar, for approximately 30 minutes between spin-coating and being placed under vacuum.

2.2.3 Current Density-Voltage Testing of OPV Devices

Once fabricated, the figures of merit for an OPV device are derived from the current density-voltage (JV) curve. This is measured by applying a bias across the device and measuring the current. Without illumination, an OPV device should behave as a diode. The energy band diagram for this situation is shown in Figure 2.8. Under short-circuit conditions the organic layer behaves as an insulator and no current flows through the device. When a forward bias is applied, electrons are injected into the conduction band of the acceptor, and holes are injected into the valence band of the donor. A small fraction of electrons and holes can recombine at the D/A interface and emit a photon, while the majority propagate through the device. This current is labeled J_{diode} in Figure 2.8.

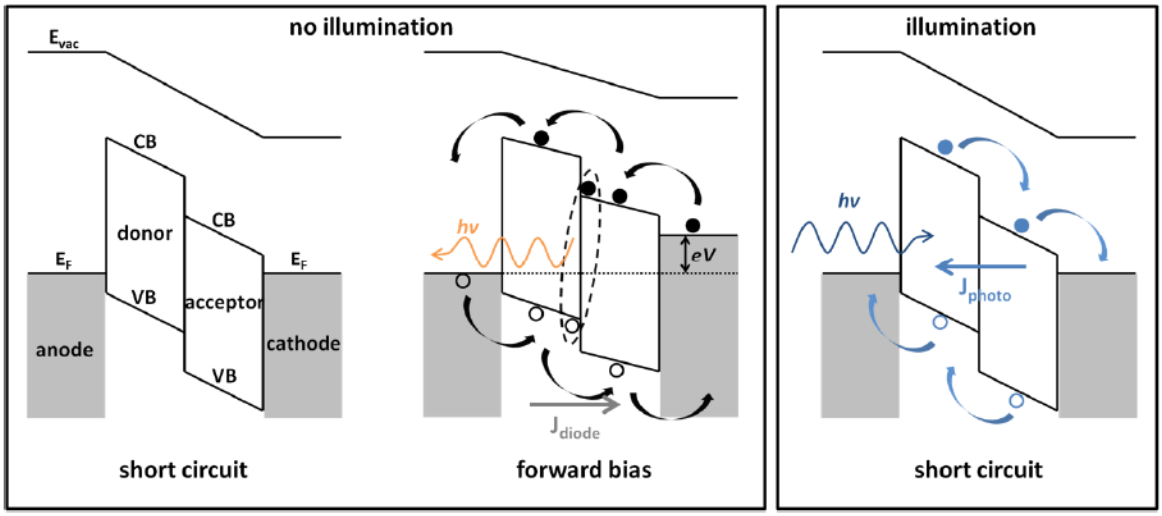

Figure 2.8. Energy band diagram of an OPV device without illumination, and with illumination. CB and VB denote the conduction and valence band, respectively. E_F is the Fermi level and E_{vac} represents the local vacuum level. *hv* is the energy of incoming or outgoing photon, while J_{diode} and J_{photo} indicate the diode current and photocurrent densities.

Under illumination, photoexcited electrons and holes can separate at the D/A interface and be collected by the cathode and anode, respectively. This establishes a photocurrent, denoted as J_{photo}. The short-circuit condition is shown in Figure 2.8. During forward bias with illumination, the total current can be thought of as a superposition of the diode current and the photocurrent, or $J_{net} = J_{diode} + J_{photo}$.

Figure 2.9 illustrates the JV curves of an OPV device in the dark and under illumination. In this figure it is apparent that the net current through the device under illumination is the diode current, shifted down by the opposing photocurrent. The figures of merit that are derived from this plot are the open circuit voltage (V_{oc}), where the JV curve of the illuminated device crosses the voltage-axis; the short-circuit current density (J_{sc}), where the JV curve of the illuminated device crosses the current density-axis; the power conversion efficiency (*PCE*), which is the ratio of the maximum generated power density (P_{max}) to the illumination power density; and the fill factor (*FF*). The formula for fill factor is given by

$$FF = \frac{P_{\max}}{J_{sc} \cdot V_{oc}} \tag{8}$$

From (8), the FF corresponds to the ratio of the two shaded regions in Figure 2.9.

The JV curve and any figures of merit derived from it are meaningless when the illumination spectrum and power are not standardized. The solar simulator (ScienceTech SS0.5K) uses a xenon arc lamp to produce a spectrum similar in shape to the AM1.5G spectrum. Special filters are used to reshape the Xe spectrum to match the AM1.5G spectrum, although due to the large intensity spikes in the infrared, the matching is not very good beyond 800 nm. However, since the dyes used in this dissertation do not absorb beyond 800 nm, we ignore that part of the spectrum and calibrate to the portion below 800 nm. This is done using a calibrated photodetector with a KG5 filter (Thorlabs NENIR60) in front. The KG5 filter removes all power beyond 800 nm, allowing for the total power density in the visible region to be matched to the expected power density in

the visible region at 1 sun illumination. Figure 2.10 shows a typical filtered Xe lamp spectrum, the AM1.5G spectrum, and the transmission profile of a KG5 filter.

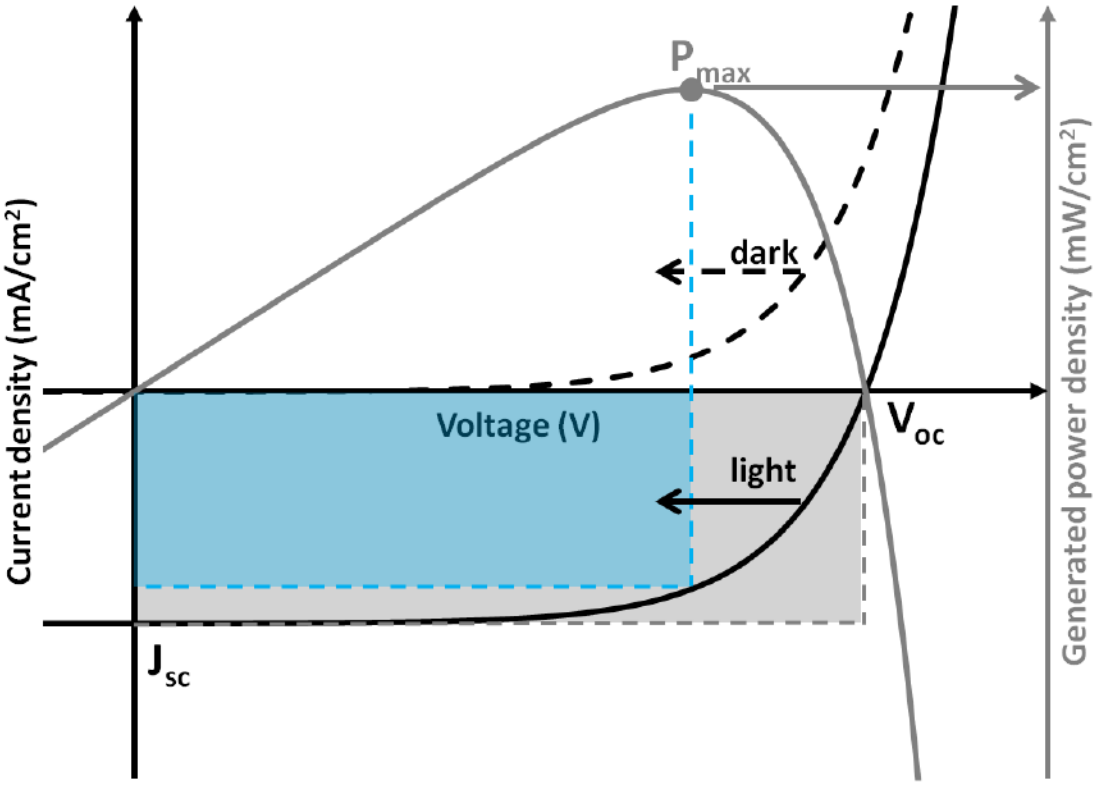

Figure 2.9. Current density-voltage curves of an OPV device in the dark (dashed-black) and under illumination (solid-black), and the power density-voltage curve under illumination (grey). J_{sc} indicated the short-circuit current density, V_{oc} is the open-circuit voltage, and P_{max} the maximum generated power density.

2.2.4 Incident Photon Conversion Efficiency of OPV Devices

The incident photon conversion efficiency (IPCE), also known as external quantum efficiency (EQE) produces a wavelength-dependent plot of the percentage of incident photons that result in collected electrons. All IPCE/EQE data presented in this dissertation were taken under short-circuit conditions. The setup of the testing apparatus

is shown in Figure 2.11, next to a sample spectrum. The white light from a solar simulator (Newport 66902) is coupled into the monochromator (Newport 74125).

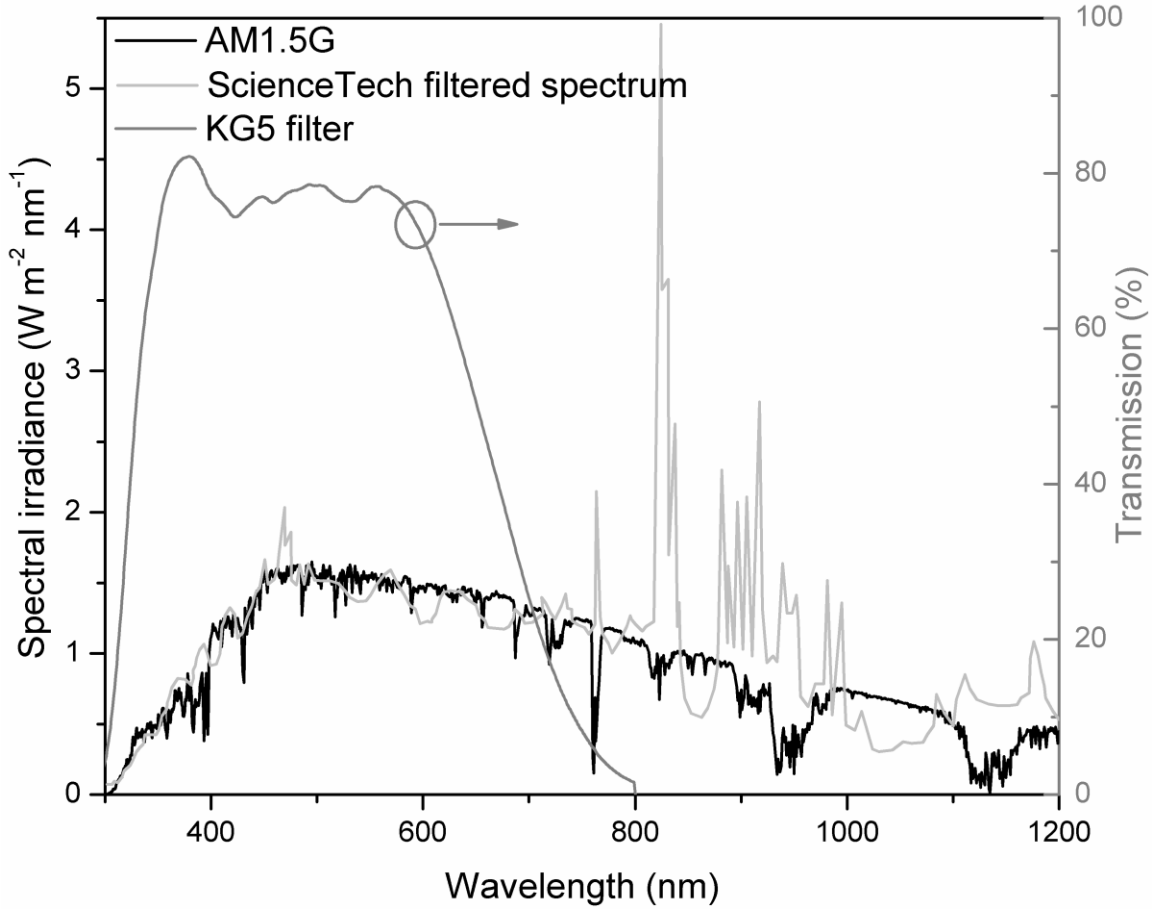

Figure 2.10. AM1.5G and a typical filtered Xe lamp spectrum, compared to the transmission of a KG5 filter.

The monochromatic light spot that illuminates the device has a rectangular shape, 0.6 ± 0.1 mm wide and 2.1 ± 0.1 mm high at the focus of the focusing lens. This rectangular light spot is oriented in the same direction as the rectangular devices, which are 1.00 ± 0.05 mm wide and 3.25 ± 0.05 mm long. The current from the device under test (DUT) is collected by the current-sensitive input of the lock-in amplifier (Signal Recovery 7265), which is modulated by a chopper wheel at 30 Hz. Since the monochromator also passes higher order wavelengths (i.e. λ/2, λ/3, etc…), a series of order-sorting longpass filters

between the light source and the monochromator are used throughout the experiment to filter out wavelengths shorter than the first-order wavelength. The wavelength-dependent current is compared to a calibrated photodiode (Newport 818-UV-L), enabling a determination of EQE.

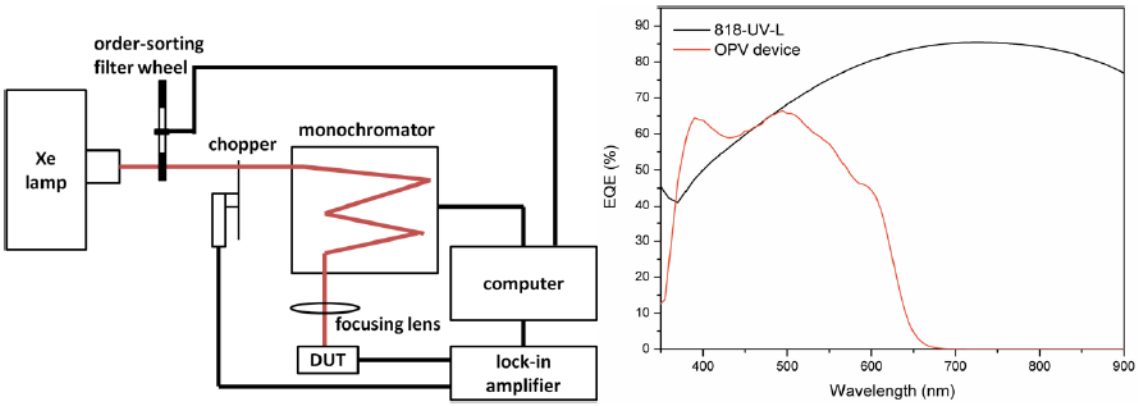

Figure 2.11. IPCE/EQE testing setup and sample output spectra.

2.3 Ultraviolet Photoelectron Spectroscopy

UPS is a technique that measures the kinetic energy of photoexcited electrons from a material illuminated by an ultraviolet source. The source used in this dissertation is a helium discharge lamp, connected to an ultrahigh vacuum system equipped with a SPECS Phoibos 150 hemispherical analyzer. From conservation of energy, the kinetic energy (*KE*) of the photoexcited electron just outside the surface being studied is given by

$$KE = h\nu - BE - \Phi \quad \text{[eV]} \tag{9}$$

where $h\nu$ is the excitation source (21.22 eV for He I), *BE* is the binding energy of the electron with respect to the Fermi level, and Φ is the difference in energy between the Fermi level and the local vacuum level. Electrical contact exists between the analyzer and sample such that the Fermi levels are aligned. Figure 2.12 shows the energy-level

diagram of a photoexcited electron in a UPS experiment. Since the work function of the analyzer is not necessarily the same as the sample, the vacuum levels are not aligned and the kinetic energy measured by the analyzer is not the same as the kinetic energy of the electron once it escapes the surface. To correct for this, a freshly sputtered silver reference sample is periodically measured to determine the analyzer work function and correct the measured kinetic energy.

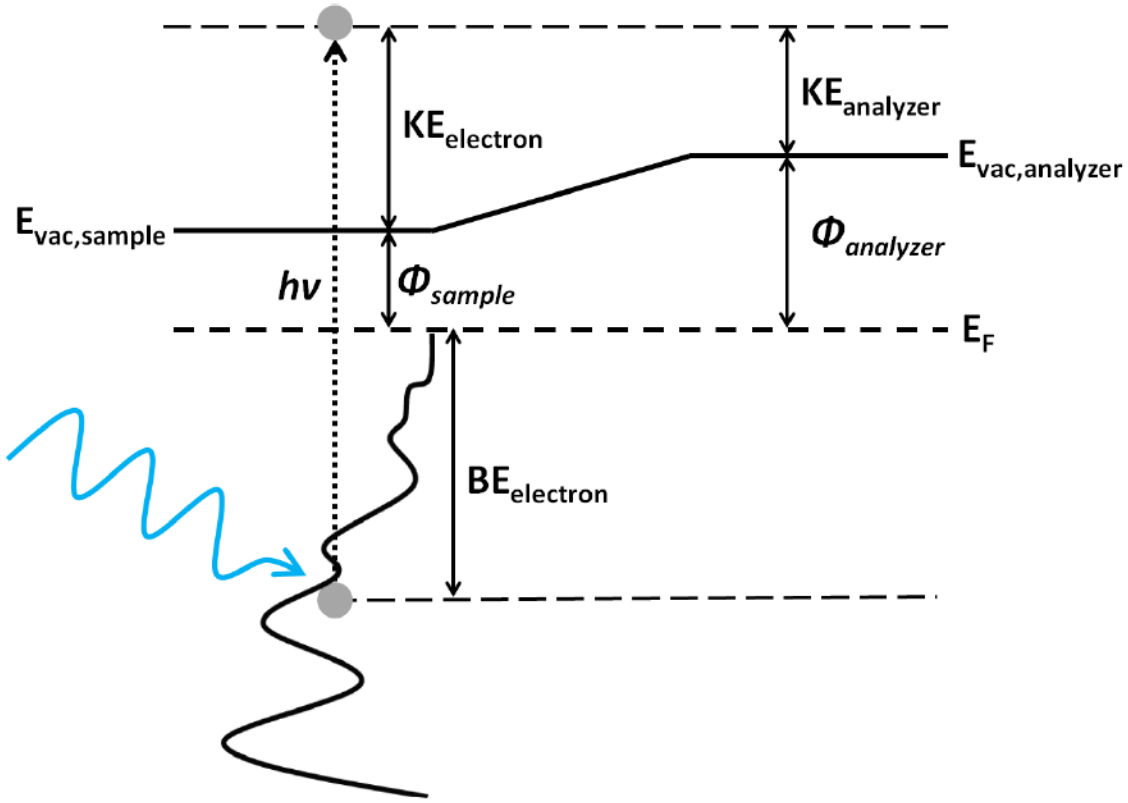

Figure 2.12. UPS energy level diagram. $E_{vac,sample}$ and $E_{vac,analyzer}$ represent the local vacuum levels outside the sample and analyzer, respectively. KE and BE are the kinetic and binding energies of the electron, and Φ indicates the energy difference between the loacel vacuum level and the Fermi level (in metals this corresponds to the work function). $h\nu$ is the energy of the ultraviolet photon.

The number density $N(E_f,h\nu)$ of photoexcited electrons is proportional to

$$N(E_f,h\nu) \propto \left|\left\langle \varphi_f(E_f)\middle|H\middle|\varphi_i(E_i)\right\rangle\right|^2 \delta(E_f - E_i - h\nu) \text{ [eV}^{-1}\text{]} \qquad (10)$$

where $\varphi_f(E_f)$ is the final state of the outgoing photoelectron, $\varphi_i(E_i)$ is the initial state of the electron, and H is the Hamiltonian describing the interaction of the UV photons with the sample. The kinetic energies of photoexcited electrons range from approximately 5-20 eV, with inelastic mean free paths of the photoexcited electrons of approximately 5-20 Å, making UPS a very surface sensitive technique. However, since the ultraviolet light penetrates deeper into the sample, inelastically-scattered secondary electrons contribute to the background signal intensity. Figure 2.13 shows the valence band structure of primary electrons superimposed on the inelastically-scattered secondary electron background.

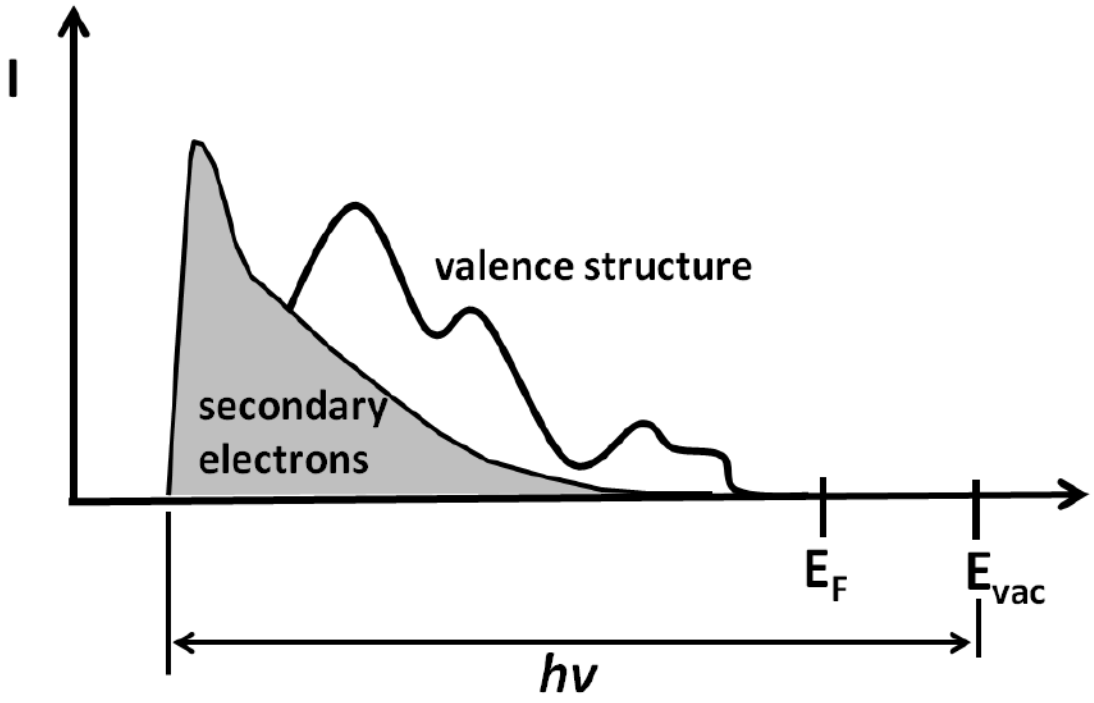

Figure 2.13. UPS signal showing contributions of primary and secondary electrons.

The onset of secondary electrons corresponds to electrons escaping at the energy of the local vacuum level outside the sample surface, with zero kinetic energy. In order to allow these electrons to pass into the analyzer and be collected, a bias of -3 V has been used throughout this dissertation to give these electrons sufficient kinetic energy to make it

into the analyzer. All UPS spectra presented have been corrected to account for this bias. Finally, UPS has been used in this dissertation to measure ionization energies of organic compounds. The ionization energy (*IE*) can be determined if the corresponding binding energies of the onset of secondary electrons E_{onset}, and the valence band maximum E_{VBM} are known

$$IE = h\nu - (E_{onset} - E_{VBM}) \qquad \text{[eV]} \tag{11}$$

Figure 2.14 shows an example UPS spectrum with E_{onset} and E_{VBM} corresponding to binding energies of 17.1 and 1.7 eV, with a calculated ionization energy of 5.8 eV. The locations of the secondary onset and valence band maximum are determined by the intersection of a tangent line drawn on the leading edge of the feature and a flat background. This is a standard method used for determining the ionization energy of organic molecules.[56] Fitting the valence band maximum is typically the largest source of error using this method, with an uncertainty of 0.1 eV when a tangent line can clearly be assigned.

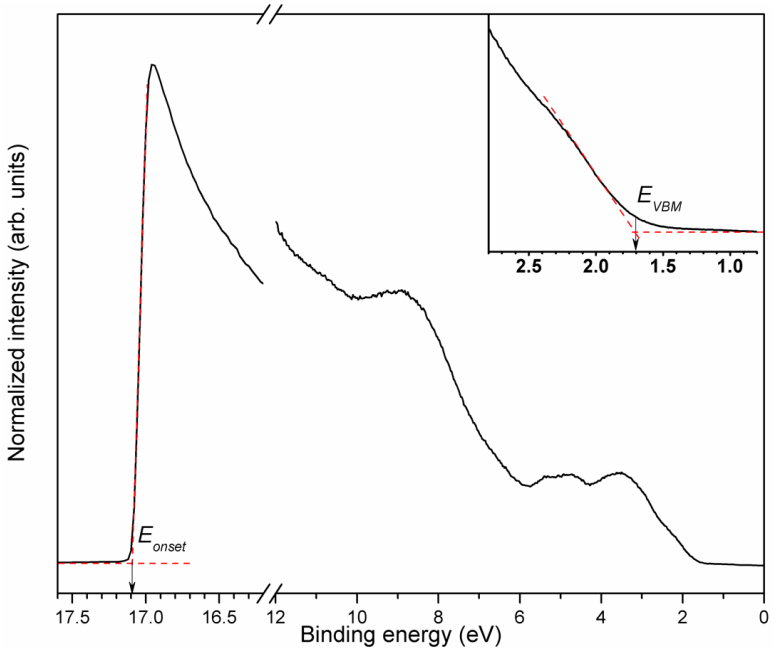

Figure 2.14. Sample UPS spectra showing tangent line determination of E_{onset} and E_{VBM}.

2.4 Atomic Force Microscopy

AFM has been used throughout this dissertation to image the surface of bulk heterojunction films for an indication of the degree of phase separation. A Bruker Innova AFM has been used in tapping mode, equipped with Bruker NTESPA cantilevers with a resonant frequency of 300 kHz, spring constant of 40 $N \cdot m^{-1}$, and a nominal tip radius of 8 nm. The experimental schematic of AFM is shown in Figure 2.15. A cantilever with a sharp tip is oscillated above the sample surface using a piezoelectric actuator. The amplitude of the oscillations is kept constant in tapping mode. When the tip approaches the sample surface, interaction forces between the surface and the tip act to change the oscillation amplitude of the cantilever. The oscillation amplitude of the cantilever is measured by reflecting a laser beam off the top of the cantilever and detecting on a photodiode. This oscillation amplitude is fed back to an electronic servo that adjusts the cantilever height above the sample surface to keep the oscillation amplitudes constant. The vertical adjustments made by the servo as the tip scans across the sample surface are used to make a topographical image of the surface.

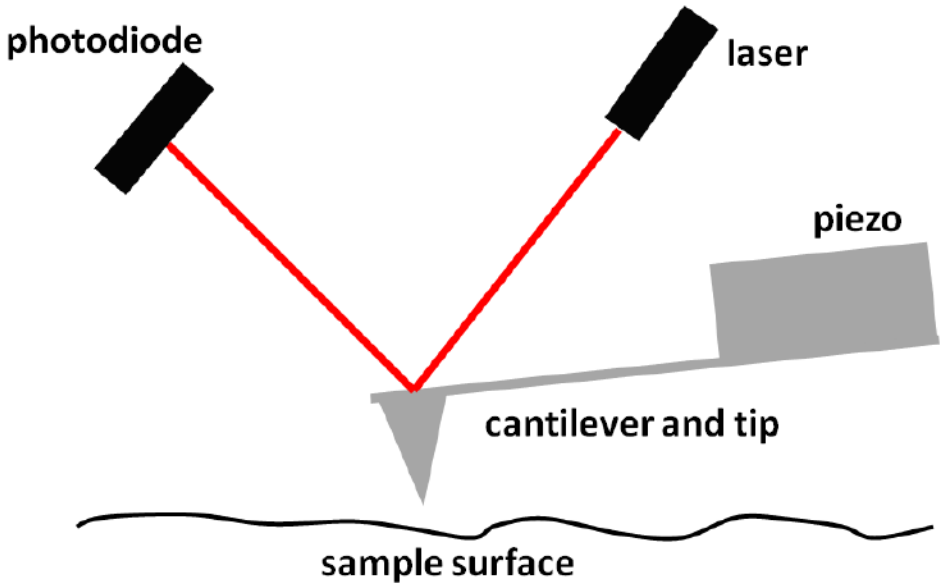

Figure 2.15. Schematic of AFM imaging.

2.5 DENSITY FUNCTIONAL THEORY

When designing dyes, it is often useful to calculate their expected electronic structure prior to synthesis. DFT is a computational tool that is based on the theory by Hohenberg and Kohn that the electronic properties of a molecule can be calculated if the electron density is known.[57] According to this theory the ground state energy of a molecule with N electrons can be written as a functional of the electron density

$$E_0[\rho(\vec{r})] = T_e[\rho(\vec{r})] + V_{en}[\rho(\vec{r})] + V_{ee}[\rho(\vec{r})] + E_{xc}[\rho(\vec{r})] \quad \text{[hartrees]} \quad (12)$$

where

$$\rho(\vec{r}) = \sum_{i=1}^{N} \left| \psi_i(\vec{r}) \right|^2 \quad \text{[electrons·bohr}^{-3}\text{]} \quad (13)$$

and T_e is the electron kinetic energy, V_{en} is the electron-nuclear potential energy, V_{ee} is the electron-electron potential energy, and E_{xc} is the exchange-correlation energy which accounts for all non-classical effects. The exact form of E_{xc} is typically unknown and needs to be approximated. In this dissertation all DFT calculations have been performed by specialists with backgrounds in computation chemistry (Lesley Rutledge, Dalhousie University, and Teresa McCormick, Portland State University), and not by the author. The level of theory used is B3LYP 6-31G(d,p). This corresponds to the Becke-3 parameter-Lee-Yang-Parr hybrid functional that uses three fitting parameters to combine Becke's exchange energy functional with the correlation energy functional of Lee, Yang, and Parr.[58–60] Each molecular orbital ψ_i used to calculate the electron density is made up of a linear combination of atomic orbitals

$$\psi_i = \sum_{j=1}^{M} c_{ji} \phi_j \quad \text{[electrons}^{1/2}\text{·bohr}^{-3/2}\text{]} \quad (14)$$

where each φ_j is expressed as a linear combination of Gaussian functions. At the 6-31G(d,p) level of theory each core atomic orbital is comprised of one basis set of six Gaussian functions, while each valence atomic orbital is comprised of a basis set of three contracted Gaussian functions (quickly decaying) and one basis set of a single diffuse Gaussian function (slowly decaying). The d and p denote additional basis sets of six d-type Gaussian functions for heavy atoms (Li to Ca) and three p-type Gaussian functions for H atoms, to account for polarization effects.

The commonly used information from DFT calculations are the lowest energy nuclear coordinates of the gas-phase molecule, and HOMO and LUMO energies. Since the exchange-correlation functional is an approximation, the energies calculated are used as a guide to compare new compounds to reference compounds with known properties. Surface plots of the HOMO and LUMO wavefunctions are typically generated with an isovalue of 0.02 $(\text{electrons})^{1/2}\cdot(\text{bohr})^{-3/2}$, corresponding to an electron density of 0.0004 $(\text{electrons})\cdot(\text{bohr})^{-3}$. Figure 2.16 shows an example of the HOMO wavefunction of pentacene, with different colored lobes indicating the phase of the wavefunction.

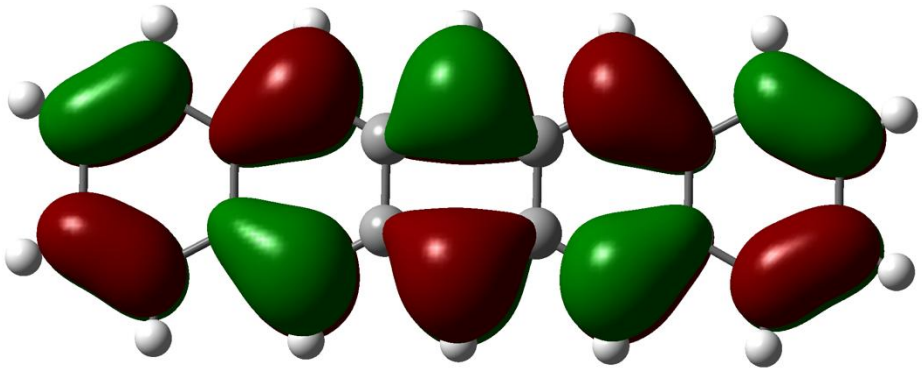

Figure 2.16. HOMO wavefunction isosurface plot of pentacene calculated using DFT.

CHAPTER 3 PUSH-PULL NON-FULLERENE ACCEPTORS

This chapter describes the characterization and integration into devices of a family of related push-pull chromophores utilizing either phthalimide or naphthalimide end groups.

3.1 DIKETOPYRROLOPYRROLE-BASED ACCEPTORS

Diketopyrrolopyrrole (DPP) has been used as a building block in industrial pigments since first being reported in 1974 by Farnum *et al*.[61] This electron deficient unit can be easily synthesized, is thermally stable, and has two locations on the amide-nitrogen atoms where solubilizing groups can be attached.[62] These desirable properties have resulted in DPP being utilized in both TFT and OPV materials.[63,64] Furthermore, DPP-based small molecules have been used as electron-accepting materials, achieving a PCE of 2% when blended with P3HT.[65–67] As a starting point for investigating small molecule non-fullerene acceptors, a series of four molecules with DPP as the central building block was synthesized. Figure 3.1 shows the DPP building block and the four molecules used in this study. Arthur Hendsbee synthesized the molecules and Lesley Rutledge performed DFT calculations. This study has been published in the Journal of Materials Chemistry A.[68]

The UV-vis absorbance spectra of thin films of compounds 1-4 are shown in Figure 3.2. Compounds 1-3 show a broad absorbance feature between 500-750 nm, with a strong shoulder extending to 900 nm. Compound 4 has much sharper features in the absorbance spectra with reduced intensity in the low-energy shoulder.

The alkyl chains attached to the DPP chromophore in compounds 2-4 were adjusted to modify the solubilities of the dyes. Unfortunately, the solubilities of all compounds in this series were too low in common organic solvents (chloroform, chlorobenzene) to be used in bulk heterojunctions. Generally, a solubility of 20 mg·mL-1 is required to cast films 100 nm thick.

3.1.1 Electronic Properties

At the donor/acceptor interface in an OPV heterojunction, sufficiently large energy offsets between donor and acceptor LUMO, for electron transfer, and donor and acceptor HOMO, for hole transfer, are required to overcome the exciton binding energy. However, since the HOMO and LUMO are theoretical states of a single electron wavefunction in an isolated molecule, the solid-state ionization energies and electron affinities are used to provide an experimental method of estimating differences in HOMO and LUMO energies.

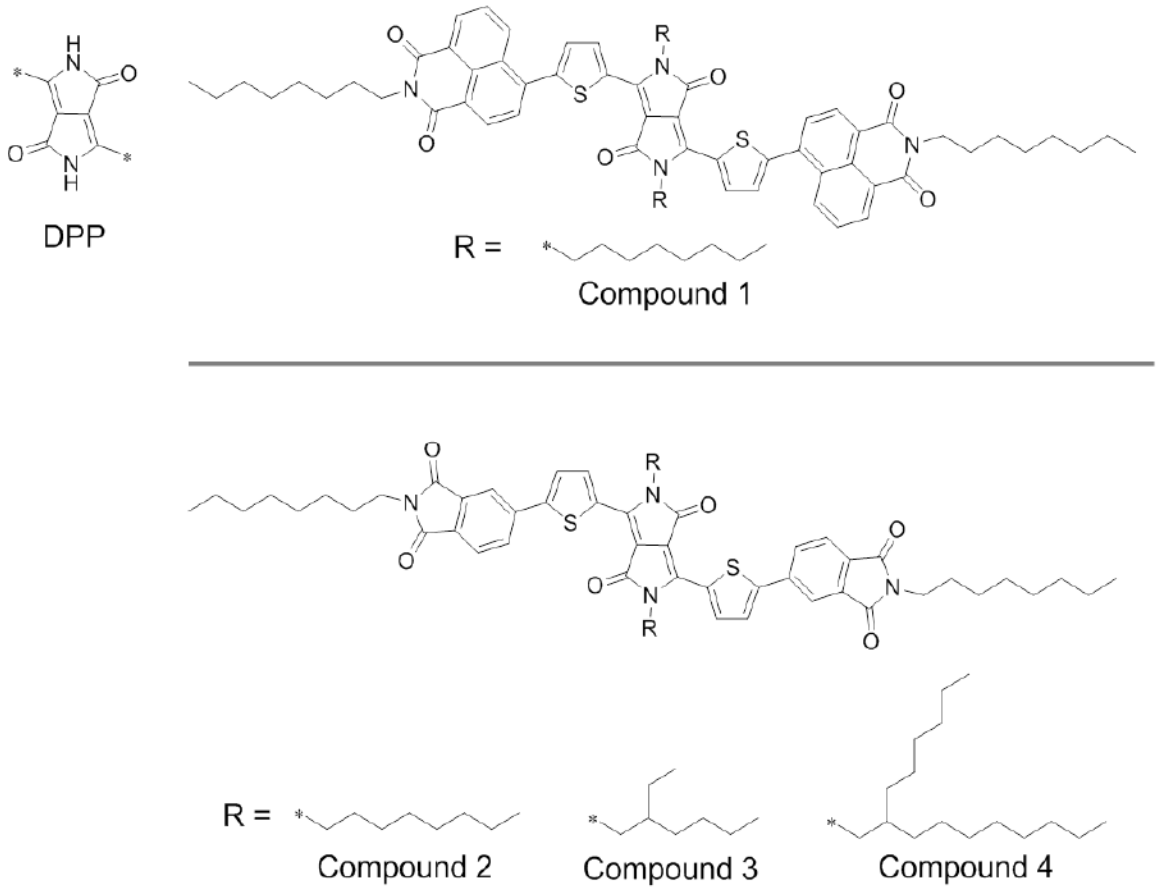

Figure 3.1. DPP building block and compounds used in this study. Reproduced from[68] with permission from the Royal Society of Chemistry.

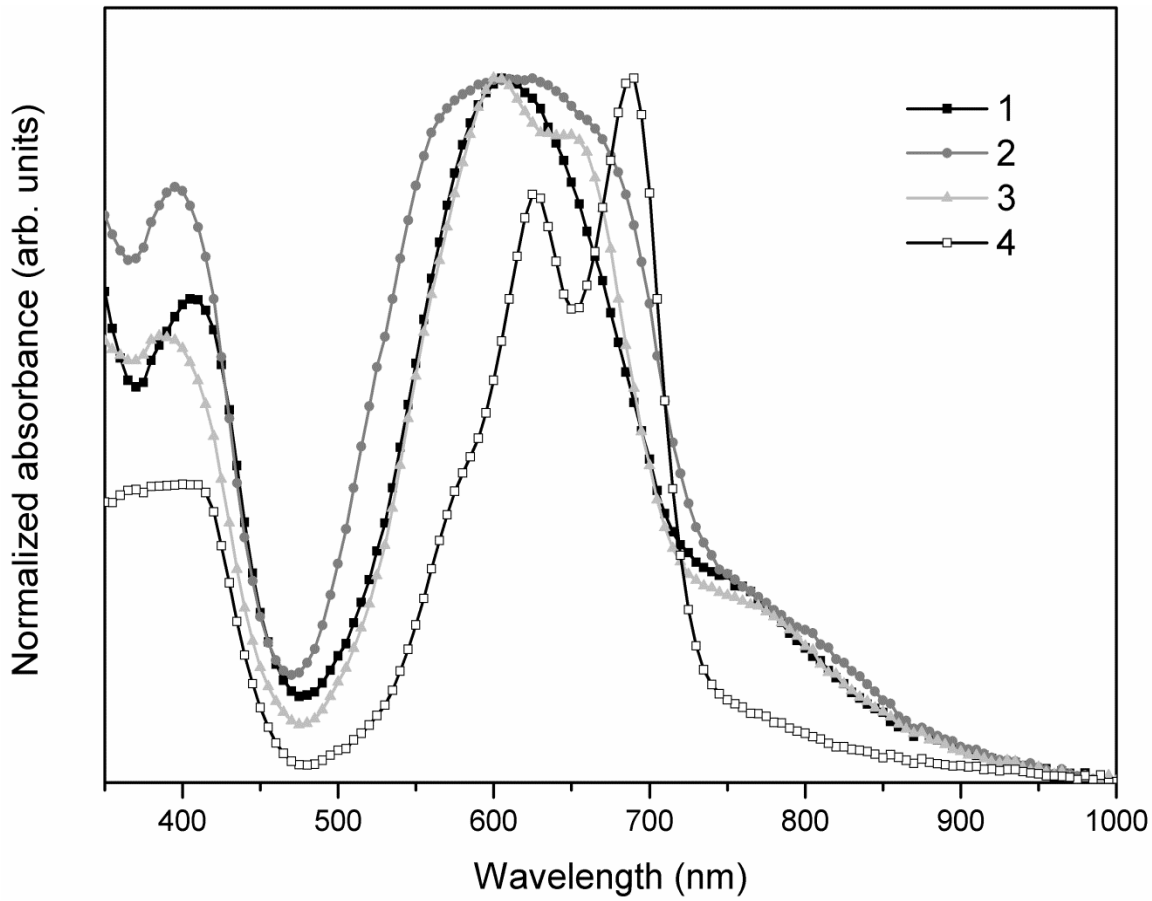

Figure 3.2. UV-vis absorbance spectra of thin films of compounds 1-4, normalized to the peak absorbance in the visible spectrum. Reproduced from[68] with permission from the Royal Society of Chemistry.

Note that the difference in energy between the local vacuum level and the HOMO should be larger than the ionization energy due to the polarization response of the surrounding molecules that stabilize the ionized molecule. Similarly, the difference in energy between the local vacuum level and the LUMO should be smaller than the electron affinity.[69] The offsets in ionization energies and electron affinities between donor and acceptor dyes are typically required to be at least 0.3-0.5 eV for charge separation to occur,[56] although, offsets as low as 0.1 eV have been documented in working, but low-performance devices.[70] Most donor materials have ionization energies in the vicinity of 4.5-5 eV, therefore acceptor molecules should have ionization

energies of at least 5.3 eV. Note that these are the requirements if currently available donor molecules are used.

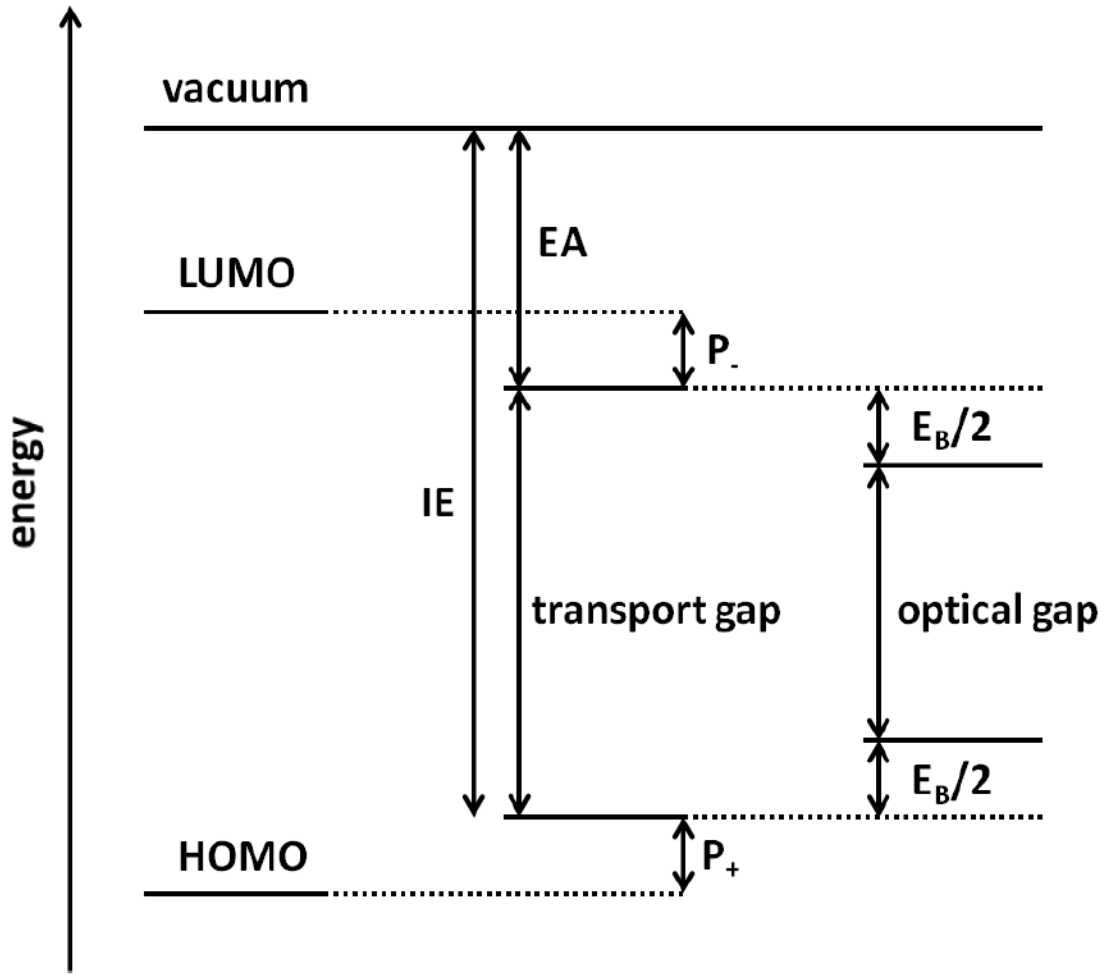

Figure 3.3. Energy diagram showing relationships between the HOMO and LUMO levels of a gas-phase molecule, ionization energy (IE) and electron affinity (EA) in the solid-state, shifted by the polarization energies of the surrounding media (P_+ and P_-), and the optical gap in relation to the transport gap, shifted by the exciton binding energy (E_B).

One of the main photodegradation mechanisms in OPVs is due to oxidation from O_{2^-} radicals, which can form after O_2 molecules accept an electron from an excited dye molecule or an acceptor anion. The reduction potential of O_2 dissolved in chlorobenzene has been measured to be 3.75 eV below vacuum via cyclic voltammetry. In an OPV device this reduction potential will likely change due to differences in the polarization

response of the organic film.[71] However, these findings are consistent with n-channel organic TFTs that tend to be stable in air when the reduction potential of the organic molecule is below -4.0 eV with respect to vacuum, as measured via cyclic voltammetry.[72]

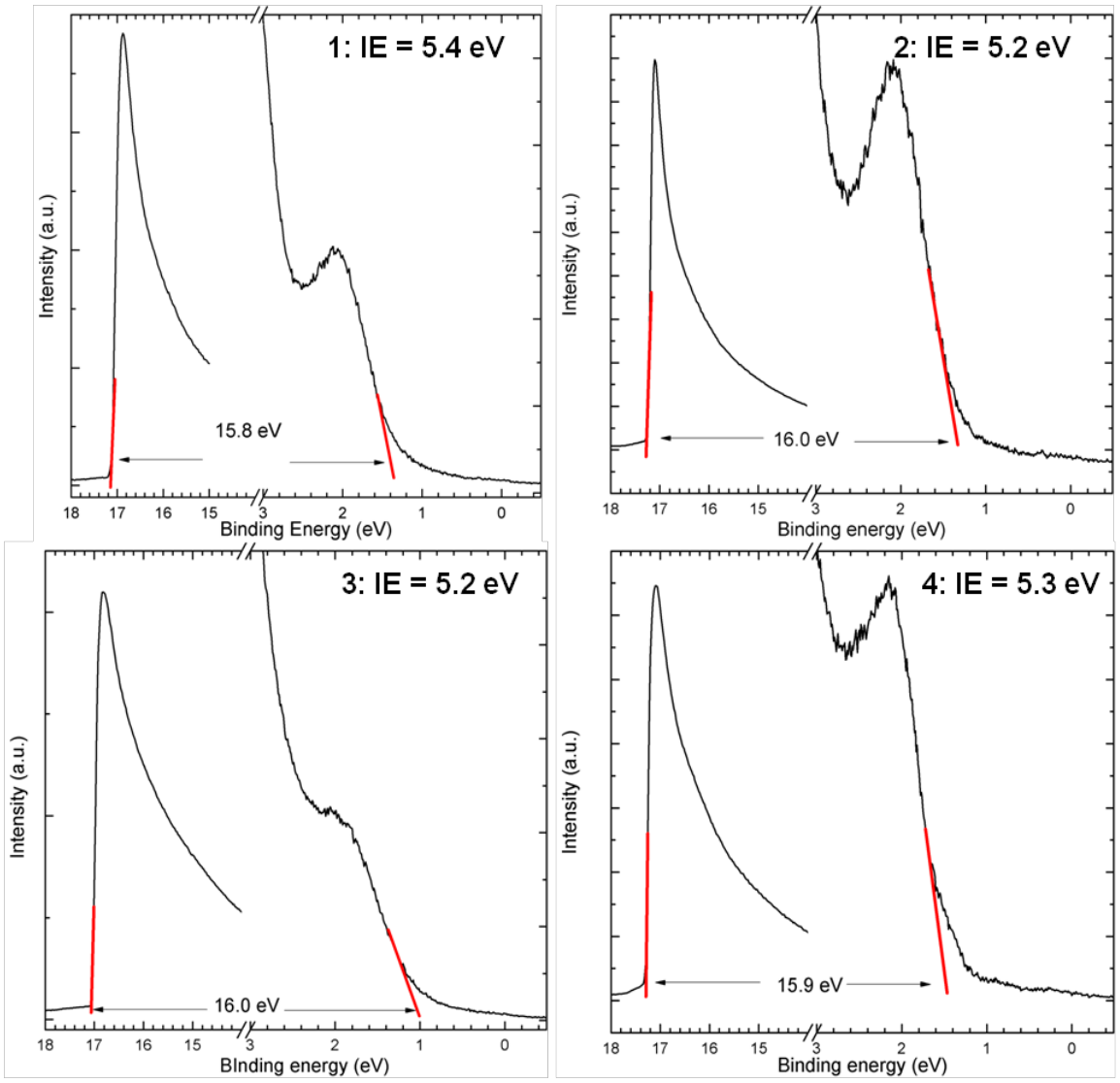

Figure 3.4. UPS spectra of compounds 1-4 with the calculated ionization energies. The uncertainty in calculated ionization energies are ± 0.1 eV. Reproduced from[68] with permission from the Royal Society of Chemistry.

Ideally, an accurate measurement of the electron affinities in the solid-state would provide a better guide to tuning the electronic properties to avoid photooxidation. Inverse photoelectron spectroscopy can be used to measure the electron affinity, although this technique has not been widely adopted and tends to suffer from poor resolution. In lieu of a direct measurement of the electron affinities, differences between electron affinities of donor and acceptor molecules can be estimated from ionization energies and optical bandgaps when the exciton binding energies are assumed to be approximately equal. Figure 3.3 shows an energy diagram indicating the relationship between HOMO and LUMO levels, ionization energy and electron affinity, and the optical bandgap.

Figure 3.4 shows the UPS spectra of compounds 1-4 with calculated ionization energies. Within experimental uncertainty (± 0.1 eV), all four compounds exhibit similar ionization energies near 5.3 eV. This value should be sufficient for hole transfer from the acceptor to donor at the D/A interface for a wide range of donor materials.

3.1.2 Charge-Transport Properties

In an OPV device under operation, the built-in electric field sweeps photogenerated carriers to the contacts. However, if the carrier density becomes large the space charge distributed throughout the device will screen this built-in field and limit charge collection. The built-in electric field in an OPV device is on the order of 1 V over a film thickness of 100 nm, or 10^5 V·cm^{-1}. The carrier density required to screen a field of this magnitude can be estimated by approximating an OPV device as a bilayer structure with positive free charge carriers on one side and negative free charge carriers on the other. This structure would look remarkably similar to the depletion region in a pn-junction, as illustrated in Figure 1.4. The electric field at the junction can be expressed by the following relation

$$E = \frac{enx_n}{\varepsilon} = \frac{epx_p}{\varepsilon} \quad [\mathrm{V \cdot m^{-1}}] \tag{15}$$

where e is the unit of elementary charge, n and p are the electron and hole concentrations, x_n and x_p are the widths of the depletion regions away from the junction, and ε is the permittivity. Considering the low dielectric constant of organic semiconductors and a 100 nm wide depletion region, hole and electron carrier densities on the order of 10^{16} cm^{-3} would be required to completely screen an electric field of 10^5 $V \cdot cm^{-1}$. High performing OPVs have current densities on the order of 10 $mA \cdot cm^{-2}$. The current density is related to the mobility μ through the drift equation

$$J = en\mu E \quad [A \cdot m^{-2}] \tag{16}$$

Assuming the carrier density is low enough to have a minimal impact on the built-in electric field of the device ($< 10^{15}$ cm^{-3}), a mobility of $> 10^{-3}$ $cm^2 \cdot V^{-1} \cdot s^{-1}$ would be required to achieve current densities of 10 $mA \cdot cm^{-2}$ under field strengths of 10^5 $V \cdot cm^{-1}$. A more rigorous device modeling study performed by Bartelt *et al*. that included bimolecular recombination with experimentally determined recombination rate constants concluded that mobilities on the order of 10^{-2} $cm^2 \cdot V^{-1} \cdot s^{-1}$ were required to achieve high fill factors.[73]

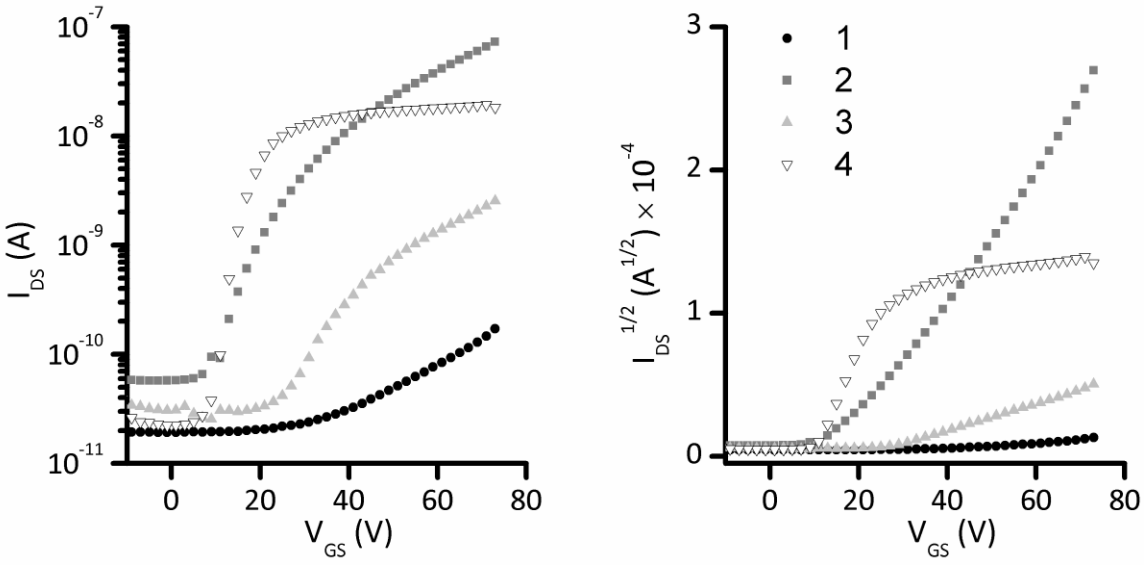

Figure 3.5. Saturation transfer curves of compounds 1-4, for bottom-gate, top-contact n-channel TFTs with C_{ox} = 10.7 $nF \cdot cm^{-2}$, W/L = 6, V_{DS} = 75 V. Reproduced from[68] with permission from the Royal Society of Chemistry.

To determine if compounds 1-4 were capable of transporting electrons, n-channel TFTs were fabricated as detailed in section 2.1 to measure the field-effect electron mobilities. The saturation transfer curves are shown in Figure 3.5, with TFT characteristics listed in Table 3.1.

Table 3.1. TFT characteristics of compounds 1-4, for bottom-gate, top-contact n-channel TFTs with C_{ox} = 10.7 nF·cm^{-2}, W/L = 6, V_{DS} = 75 V. Reproduced from[68] with permission from the Royal Society of Chemistry.

Compound	μ_e (cm^2·V^{-1}·s^{-1})	I_{on}/I_{off}	V_T (V)
1	(1.1 ± 0.4) x 10^{-6}	10^1	40 ± 4
2	(1.2 ± 0.6) x 10^{-3}	10^3	15 ± 3
3	(3.4 ± 0.2) x 10^{-5}	10^2	25 ± 2
4	(1.9 ± 0.6) x 10^{-3}	10^3	11 ± 1

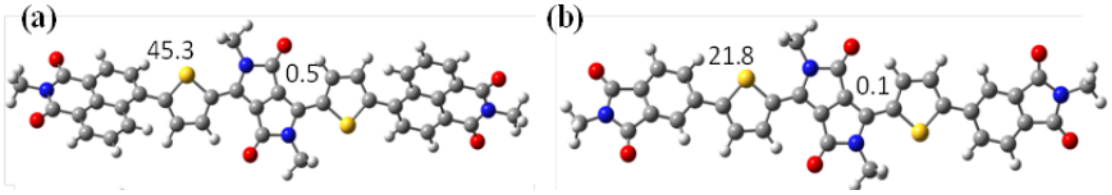

Figure 3.6. DFT optimized geometries of gas-phase molecules with a) naphthalimide and b) phthalimide end groups. Dihedral angles between aromatic units are indicated. Reproduced from[68] with permission from the Royal Society of Chemistry.

The electron mobilities of compounds 1-4 were found to be lower than those of $PC_{61}BM$, which typically achieves electron mobilities on the order of 10^{-2} cm^2·V^{-1}·s^{-1} in TFTs.[74] Compound 1, with naphthalimide end groups was found to have the lowest mobility. The bulkier naphthalimide end groups are expected to have a larger dihedral angle with the adjacent thiophene unit, compared to the less bulky phthalimide groups. This can result in reduced crystallinity and lower charge-carrier mobilities. Figure 3.6 shows the DFT-optimized geometries of the gas-phase naphthalimide and phthalimide end-capped molecules, with dihedral angles of 45.3° and 21.8°, respectively. Compound 4 exhibited the largest electron mobility, however the mobility significantly decreased when V_{GS} was larger than ~ 20 V. This behavior has previously been observed by Bittle *et al.*, who

attributed the apparent change in mobility to gated-Schottky source and drain contacts.[75] At low V_{GS} a charge injection barrier between the metal and semiconductor can result in the contact resistance being larger than the channel resistance. With increasing V_{GS}, injection barrier height lowering can lead to exponentially decreasing contact resistance.

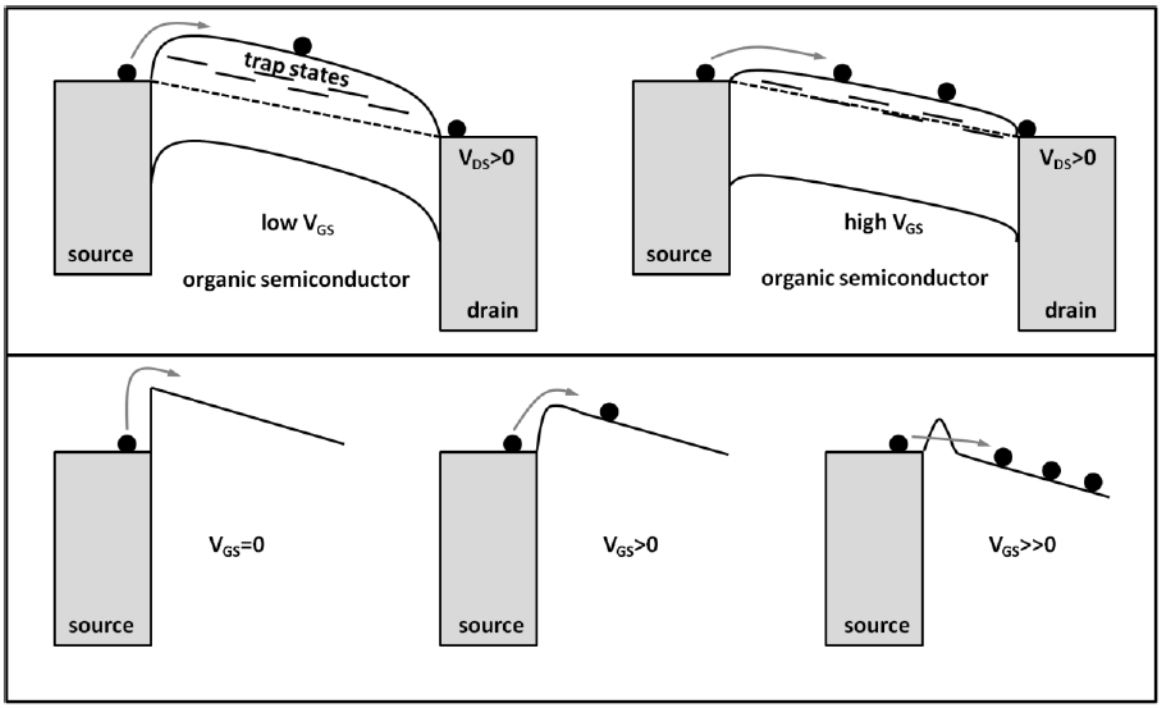

Figure 3.7. Possible scenarios where an apparent change in electron mobility could be observed. In the top panel a large density of trap states occurs near the conduction band of the organic semiconductor. At low gate bias the Fermi level lies below the trap state energies. As the gate bias is increased, injected electrons increase the carrier concentration and raise the Fermi level. As the Fermi level approaches the trap state energy, it becomes pinned and no longer moves with the gate bias. Thus the change in carrier concentration with increasing gate bias significantly reduces. In the lower panel, a Schottky barrier between the source contact and the organic semiconductor results in a large contact resistance at low gate bias, limiting the current through the device. As the gate bias is increased and electrons fill the channel, the positive image charge on the contact lowers the injection barrier. The positive gate bias also pulls down the conduction band energy, allowing electrons to tunnel through the injection barrier, significantly lowering the contact resistance. At some positive gate bias the contact resistance becomes lower than the channel resistance and the current becomes channel limited.

At higher V_{GS} the channel resistance can begin to dominate and limit the mobility, producing two distinct linear regions on the $I_D^{1/2}$ vs. V_{GS} saturation transfer curves. Alternatively, a large density of trap states within the bandgap of the semiconductor could result in the same behavior. As V_{GS} increases, the carrier concentration in the organic semiconductor increases, moving the Fermi level through the bandgap. As the Fermi level reaches the trap state energy, it becomes pinned and no longer moves with increasing V_{GS}. Therefore increasing V_{GS} beyond this point has a significantly reduced effect on the carrier concentration, appearing as a kink in the drain current. These two possible scenarios are illustrated in Figure 3.7.

Evidence of contact resistance can be seen in output curves of TFTs, where V_{GS} is held constant while V_{DS} is varied. In this scenario a positive gate bias populates the channel with negative charge carriers. When a small V_{DS} is applied, the device should behave as a resistor when ohmic contacts are present. The resulting output curves should go through the origin of the plot in a linear fashion. However, when Schottky barriers are present the contacts behave as diodes, causing the output curve to have a diode-like turn on before transitioning to the linear region. Figure 3.8 shows the output curves of TFTs made from compounds 1-4. Output curves of compounds 2 and 4 cross linearly through the origin and do not exhibit evidence of contact resistance. Output curves of compounds 1 and 3 do exhibit a diode-like hook at low V_{DS}, however the overall drain currents are an order of magnitude lower, and the data suffers from significant noise. The drain current of compound 1 also becomes negative at low V_{DS} before turning around and becoming positive. When a positive bias is applied to the drain contact, the electric field in the vicinity of the drain decreases and the channel loses carriers in response. This small displacement current with opposite sign can become dominant when the overall drain current is small, as in the case of compounds 1 and 3.

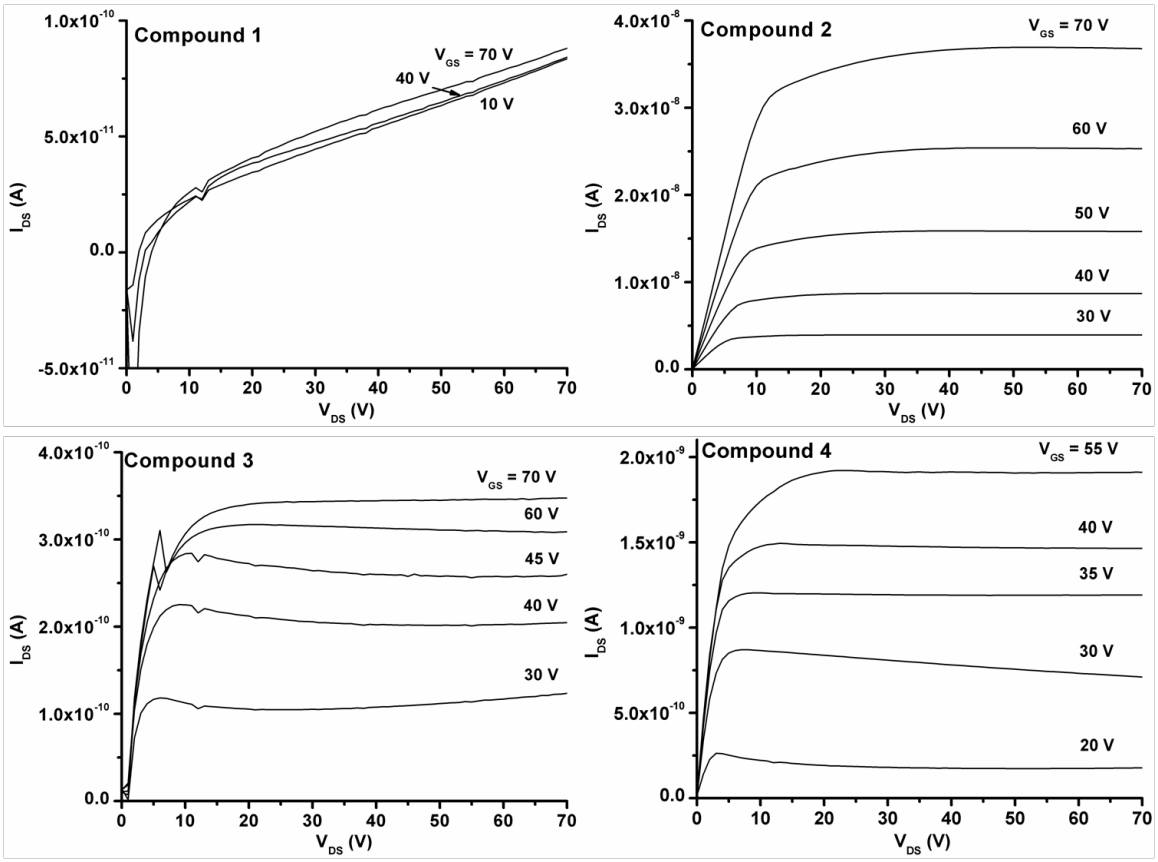

Figure 3.8. Output curves of compounds 1-4, for bottom-gate, top-contact n-channel TFTs with C_{ox} = 10.7 nF·cm^{-2}, W/L = 6.

3.1.3 Concluding Remarks

As a first attempt at making small molecule acceptors, compounds 1-4 showed sufficiently large ionization energies for use in OPV devices. However, the field-effect electron mobilities were found to be lower than $PC_{61}BM$. While these mobilities were not prohibitive for use in OPV devices, the solubilities of compounds 1-4 in chloroform and chlorobenzene were found to be too low to incorporate into solutions for casting bulk heterojunction devices. Due to the combination of low mobility and low solubility, this series of molecules was not investigated further.

3.2 Phthalimide-Thiophene Acceptors

Following the DPP-based acceptor study, a series of five new molecules without the central electron-deficient core were synthesized to study the inherent properties of phthalimide-thiophene-based molecules. Arthur Hendsbee synthesized the molecules and performed single crystal x-ray diffraction (XRD). This study has been published in the Journal of Materials Chemistry C.[76] The number of thiophene units was varied between 1-3, as well the length of the terminal alkyl chain was varied from 4 to 6 to 8 carbons for the two-thiophene version. This series of molecules is shown in Figure 3.9. Figure 3.10 shows the thin-film UV-vis absorbance spectra of the five compounds, with absorbance maxima near 400 nm.

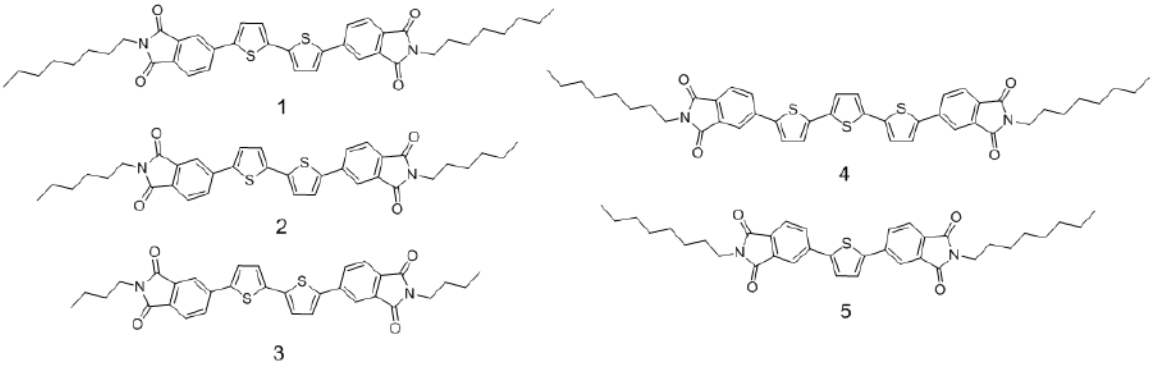

Figure 3.9. Phthalimide-thiophene compounds used in this study. Reproduced from[76] with permission from the Royal Society of Chemistry.

3.2.1 Electronic Properties

The UPS spectra of compounds 1-5 are shown in Figure 3.11. Going from compound 5 to 1 to 4, the ionization energies decrease by 0.4 eV with each additional thiophene unit. This behavior is expected since the ratio of electron rich to electron poor building blocks increases. However, the changes in ionization energy with alkyl chain variation between compounds 1-3 is less obvious. Previous studies on ultrathin films of pentacenes and sexithiophenes have demonstrated that molecular orientation on the substrate (flat versus upright) can lead to changes in ionization energy of similar magnitude.[77–80]

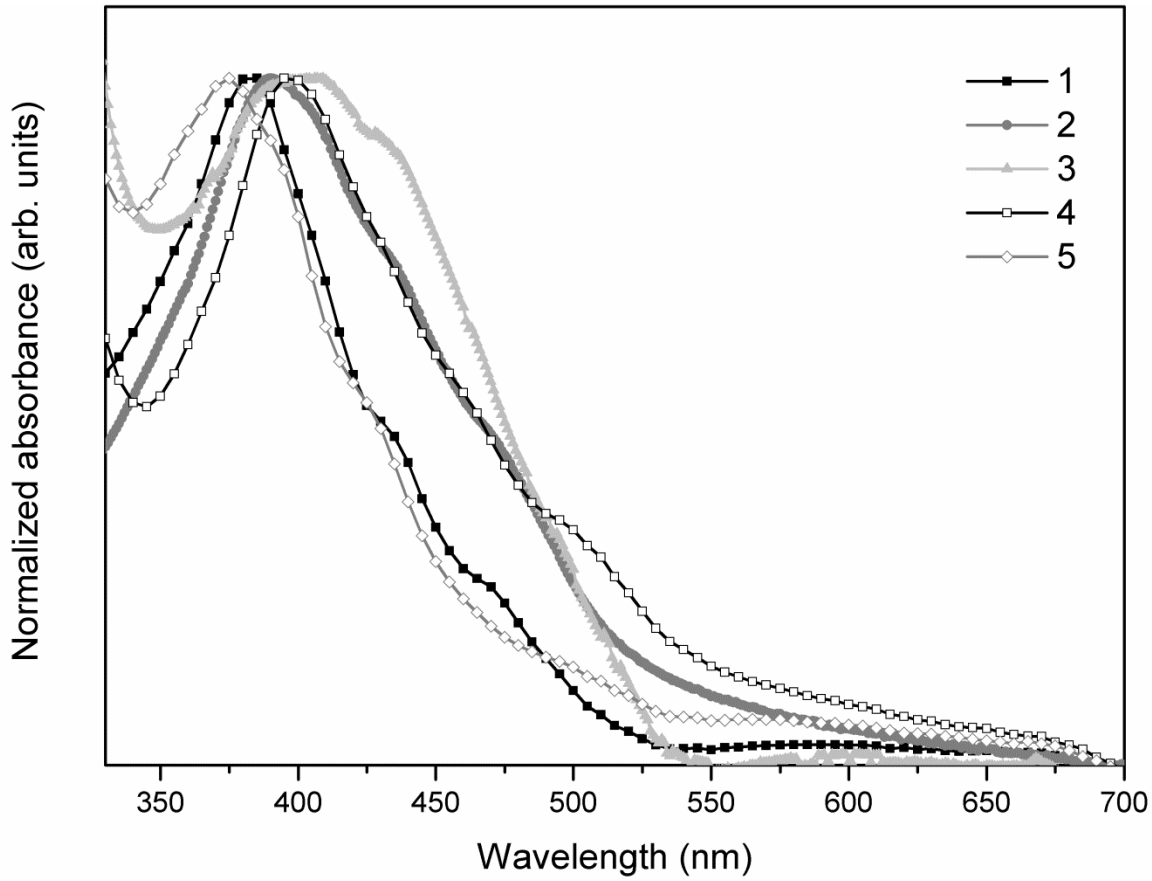

Figure 3.10. UV-vis absorbance spectra of thin films of compounds 1-5, normalized to the peak absorbance in the visible spectrum. Reproduced from[76] with permission from the Royal Society of Chemistry.

Furthermore, crystalline packing motifs can have a large influence on polarization energies that act to screen net charges, effectively decreasing ionization energies and increasing electron affinities.[81] Single crystals of compounds 1 and 2 were analyzed via single crystal XRD, showing that compound 1 adopts a herringbone-like motif referred to as the γ-structure,[82] while compound 2 arranges in columnar stacks.

3.2.2 Charge-Transport Properties

TFTs of compounds 1-5 were fabricated as detailed in section 2.1 to determine the electron mobilities. Saturation transfer curves are shown in Figure 3.12, with TFT characteristics in Table 3.2. The two-thiophene materials (compounds 1-3) all have similar electron mobilities on the order of 10^{-1} $cm^2 \cdot V^{-1} \cdot s^{-1}$. Compound 5, with three

thiophene units had a slightly lower mobility but comparable to compounds 1-3. Compound 4, with one thiophene unit exhibited much lower electron mobilities. Additionally devices made from compound 4 showed relatively large currents in the off state, with weak field-effect dependence. Both of these observations are consistent with a large density of trap states. If a high density of partially-filled states exists within the gap near the LUMO edge, these states will effectively pin the Fermi level, inhibiting its variation with applied gate bias. Thus, the electron density does not change appreciably with gate bias, preventing the device from turning fully off, and suppressing the macroscopically-observed electron mobility above threshold.

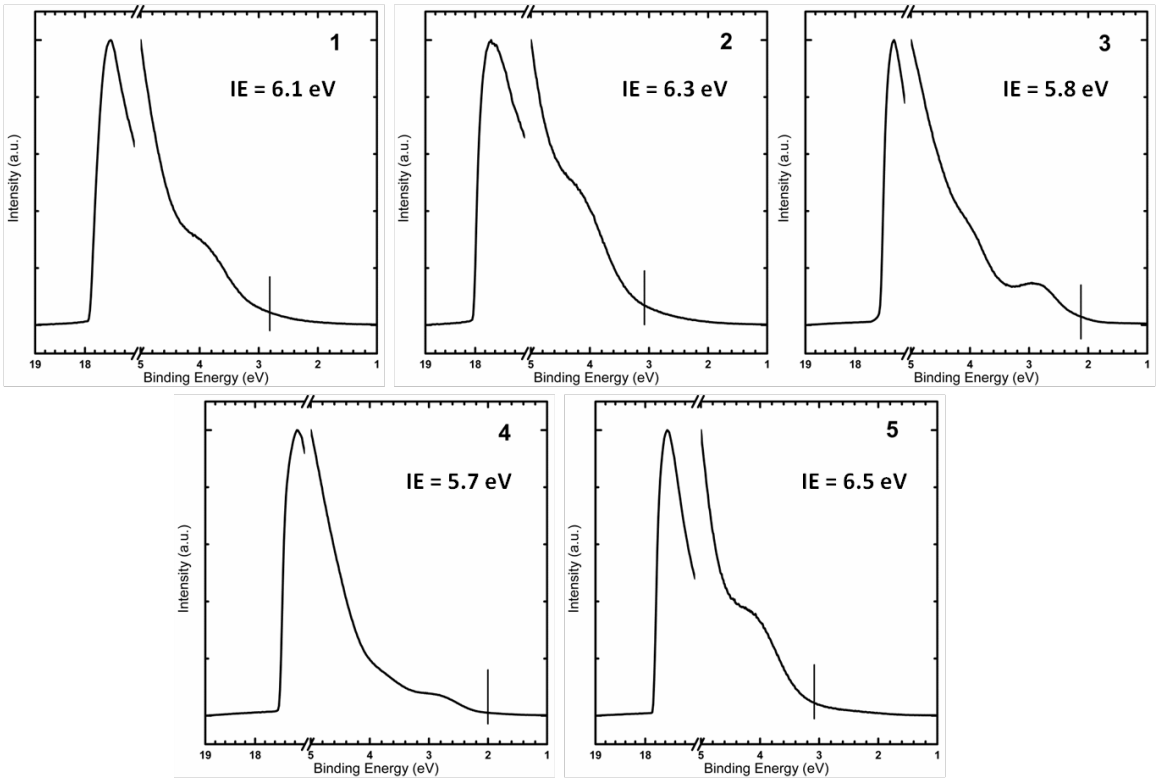

Figure 3.11. UPS spectra of compounds 1-5 with the calculated ionization energies. The vertical lines indicate the locations of the valence band maxima. Uncertainty in the calculated ionization energies are ± 0.1 eV. Reproduced from[76] with permission from the Royal Society of Chemistry.

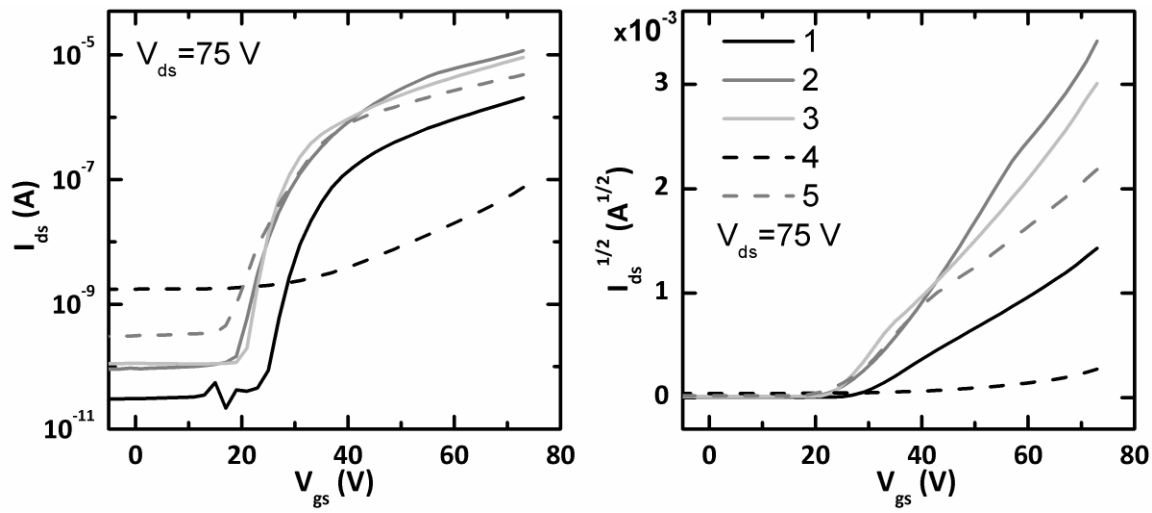

Figure 3.12. Saturation transfer curves of compounds 1-5, for bottom-gate, top-contact n-channel TFTs with C_{ox} = 10.7 nF·cm^{-2}, W/L = 4, V_{DS} = 75 V. Reproduced from[76] with permission from the Royal Society of Chemistry.

Table 3.2. TFT characteristics of compounds 1-5, for bottom-gate, top-contact n-channel TFTs with C_{ox} = 10.7 nF·cm^{-2}, W/L = 4, V_{DS} = 75 V. Reproduced from[76] with permission from the Royal Society of Chemistry.

Compound	μ_e (cm^2·V^{-1}·s^{-1})	I_{on}/I_{off}	V_T (V)
1	(7.6 ± 0.6) x 10^{-2}	10^5	28 ± 1
2	(2.1 ± 0.2) x 10^{-1}	10^5	28 ± 3
3	(1.5 ± 0.1) x 10^{-1}	10^5	23 ± 3
4	(2.3 ± 0.1) x 10^{-3}	10^1	45 ± 4
5	(6.3 ± 0.8) x 10^{-2}	10^4	23 ± 2

Output curves of devices containing compounds 1-5 are shown in Figure 3.13. While contact resistance is not evident from these plots, the saturation regions show a downward slope at high V_{DS}. This behavior can be understood from equation 6, where the drain current depends on the difference between V_{GS} and V_T. If V_T increases as the device operates, the drain current will be reduced. This can occur when a large density of traps are present.

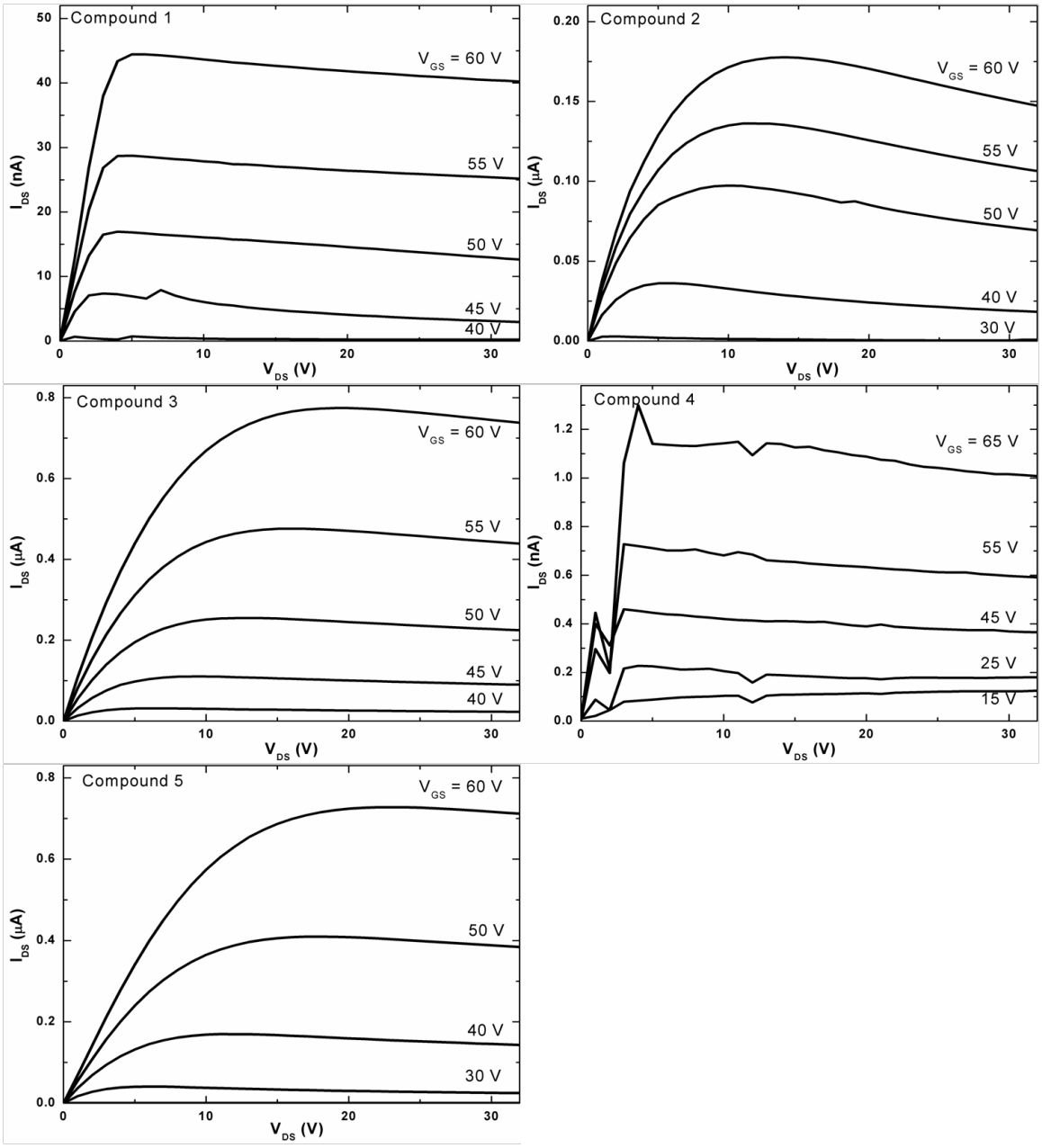

Figure 3.13. Output curves of compounds 1-5, for bottom-gate, top-contact n-channel TFTs with C_{ox} = 10.7 nF·cm^{-2}, W/L = 4.

3.2.3 Concluding Remarks

Due to the large ionization energies and sufficiently high electron mobilities, compounds 1-3 were deemed to be promising candidates for electron acceptors in OPV devices. Since compound 1, with *n*-octyl solubilizing chains had the best solubility in organic

solvents, OPV devices were fabricated by Ala'a Eftaiha. However, this compound was still found to be too crystalline, leading to large micron-sized domains when blended with P3HT. As a result, OPV devices exhibited a PCE of only 0.2 %.[83]

3.3 Phthalimide-Furan Acceptors

Furan is often cited as a more environmentally friendly alternative to thiophene, given its similar structure and availability from agricultural biproducts.[84] To investigate the usefulness of furan in electron-transporting materials, a phthalimide-furan acceptor was synthesized and compared with its thiophene counterpart. Arthur Hendsbee synthesized the materials and performed single crystal XRD and differential scanning calorimetry, Teresa McCormick performed DFT calculations. This study was published in Organic Electronics.[85] Figure 3.14 shows the structures of the thiophene- and furan-containing compounds used in this study.

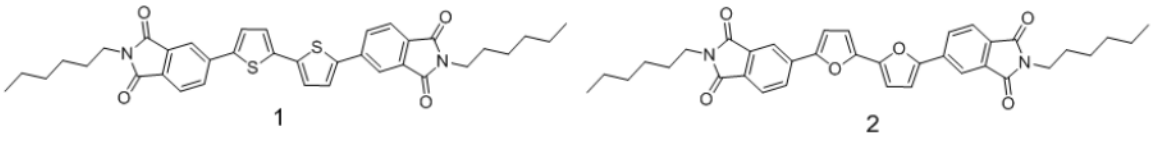

Figure 3.14. Phthalimide-thiophene and phthalimide-furan compounds used in this study. Reproduced from[85] with permission from Elsevier.

3.3.1 Optoelectronic Properties

The UV-vis absorbance and photoluminescence emission spectra of compounds 1 and 2 in chloroform and as evaporated films are shown in Figure 3.15. Both materials exhibit very similar optical behavior in solution, with absorbance peaks at 425 nm and 432 nm for compounds 1 and 2, respectively, and emission peaks at 515 nm and 530 nm. The solid-state absorbance peaks are also close, at 384 nm and 377 nm. However, the solid-state emission peaks are further red-shifted in compound 1 (549 nm vs. 518 nm), where the larger Stokes shift indicates a greater degree of structural reorganization upon photoexcitation. This is consistent with increased steric repulsion due to the larger sulfur

atom, causing a greater degree of twisting between conjugated units along the molecular backbone. Differential scanning calorimetry demonstrated melting and crystallization temperatures 26 and 23 degrees higher for compound 2, consistent with increased molecular planarity and increased π-π interactions in the furan-containing compound.[85]

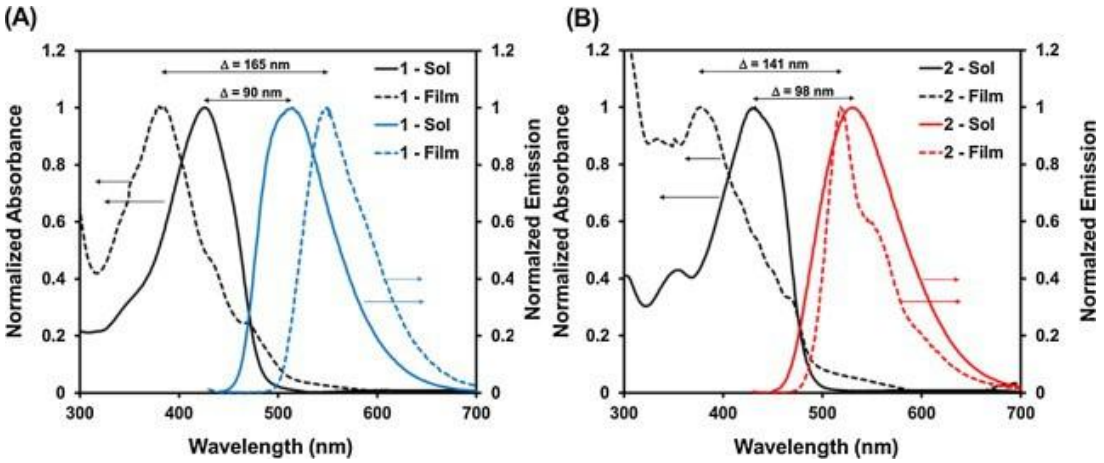

Figure 3.15. Absorbance and emission spectra of solutions in chloroform and evaporated films of a) compound 1, and b) compound 2. Reproduced from[85] with permission from Elsevier.

The UPS spectra of evaporated films of compounds 1 and 2 are shown in Figure 3.16. Both compounds have nearly-overlapping features with equivalent calculated ionization energies of 6.0 ± 0.1 eV.

3.3.2 Charge-Transport Properties

Initially, n-channel TFTs were fabricated using compounds 1 and 2, as detailed in section 2.1. Saturation-transfer curves of these devices are shown in the lower two panels of Figure 3.17, with TFT characteristics in Table 3.3. The interesting thing to note here is that the furan-containing compound 2 completely lacks a measureable electron mobility. To further investigate the differences in charge transfer properties, p-channel TFTs were also fabricated to measure the hole mobilities (Figure 3.17 upper two panels). Interestingly, compound 2 exhibited a hole mobility and order of magnitude larger than compound 1.

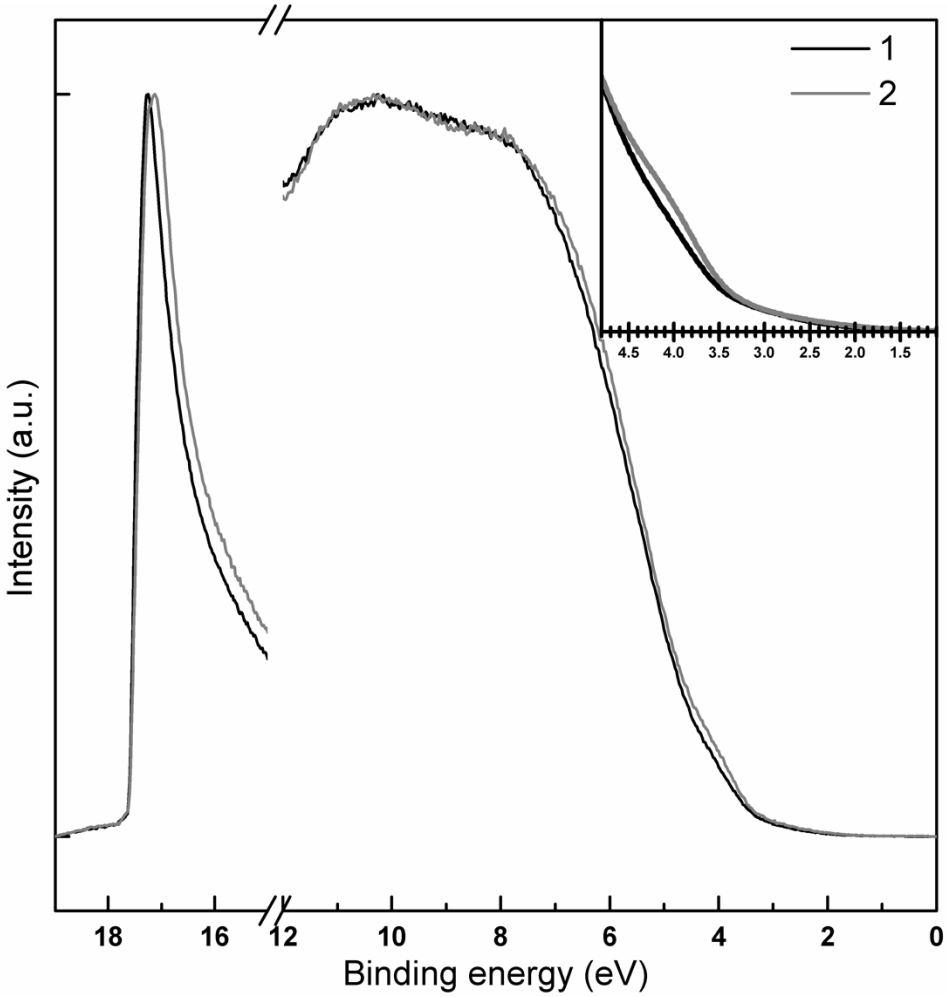

Figure 3.16. UPS spectra of evaporated films of compounds 1 and 2 showing nearly identical features. Reproduced from[85] with permission from Elsevier.

The output curves of p-channel devices of compounds 1 and 2 are shown in Figure 3.18. Compound 1 appears to exhibit a diode-like turn-on at low magnitude V_{DS}, indicating there may be some contact resistance in this device. However, the current also changes sign for $|V_{GS}| < 75$ V, indicative of a displacement current as previously described in section 3.1. Additionally, the saturation current decreases at larger magnitude V_{DS}, demonstrating that a large density of charge traps may be present. Conversely, output curves of compound 2 show none of these detrimental aspects.

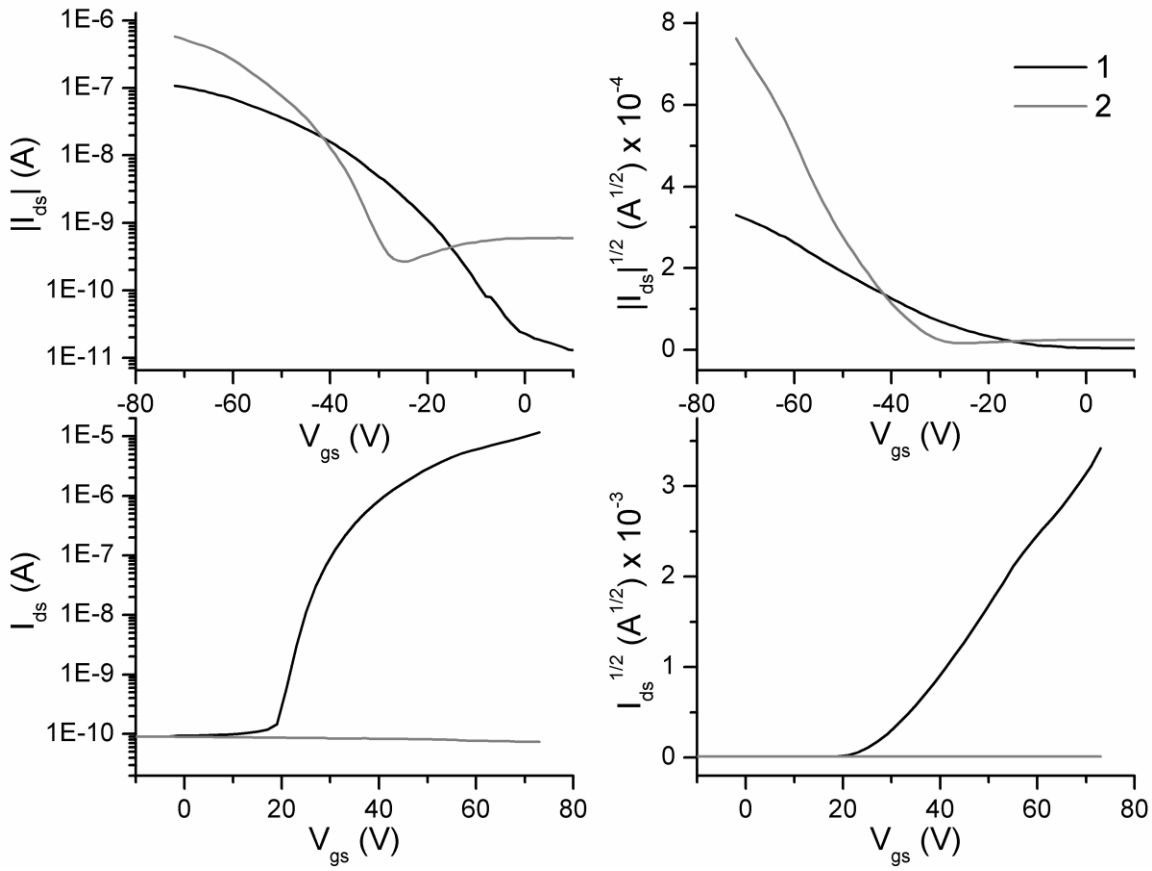

Figure 3.17. Saturation transfer curves of p-channel (top row) and n-channel (bottom row) TFTs of compounds 1 and 2, for bottom-gate, top-contact TFTs with C_{ox} = 10.7 nF·cm^{-2}, W/L = 4, V_{DS} = 75 V. Reproduced from[85] with permission from Elsevier.

Table 3.3. TFT characteristics of compounds 1 and 2, for bottom-gate, top-contact TFTs with C_{ox} = 10.7 nF·cm^{-2}, W/L = 4, V_{DS} = 75 V. Reproduced from[85] with permission from Elsevier.

Compound	μ_h (cm^2·V^{-1}·s^{-1})	I_{on}/I_{off}	V_T (V)	μ_e (cm^2·V^{-1}·s^{-1})	I_{on}/I_{off}	V_T (V)
1	(1.7 ± 0.5) x 10^{-3}	10^4	-20 ± 3	(2.1 ± 0.2) x 10^{-1}	10^5	28 ± 3
2	(2.6 ± 0.8) x 10^{-2}	10^3	-35 ± 3	-	-	-

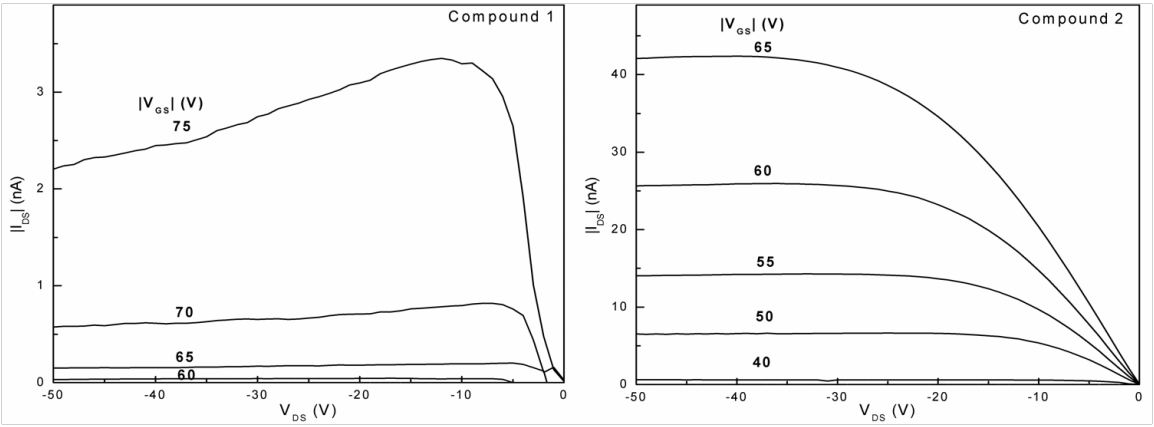

Figure 3.18. Output curves of compounds 1 and 2, for bottom-gate, top-contact p-channel TFTs with C_{ox} = 10.7 nF·cm^{-2}, W/L = 4.

3.3.3 Single-Crystal X-Ray Analysis

To try to identify the origin of the complete loss of electron mobility in compound 2, single-crystal XRD of compounds 1 and 2 was performed by Arthur Hendsbee. The calculated structures are shown in Figure 3.19, with remarkable similarities. Both compounds adopt a columnar stacking motif with similar vertical distances between the π-planes. The largest difference is in the pitch angle (31° vs 11°), where adjacent layers are shifted along the long axes of the molecules.

3.3.4 Computational Analysis

To further understand the nature of the differences in charge transport, DFT calculations of dimers of compounds 1 and 2 were performed, based on the single crystal packing structures. Figure 3.20 shows the DFT-calculated molecular orbitals and electrostatic potential maps of dimers of compounds 1 and 2. Compound 1 was found to have a degenerate LUMO and LUMO+1, which can greatly enhance electron transport as it increases available states for injected electrons to occupy. Compound 2 exhibited nearly-degenerate LUMO levels, separated by approximately 20 meV. The electrostatic potential (ESP) maps also reveal that compound 2 has a larger degree of charge separation, with positive charge localized on the furan units, and negative charge localized on the imide oxygens. Having localized positive charge on the conjugated core may also contribute to inhibited electron transport.

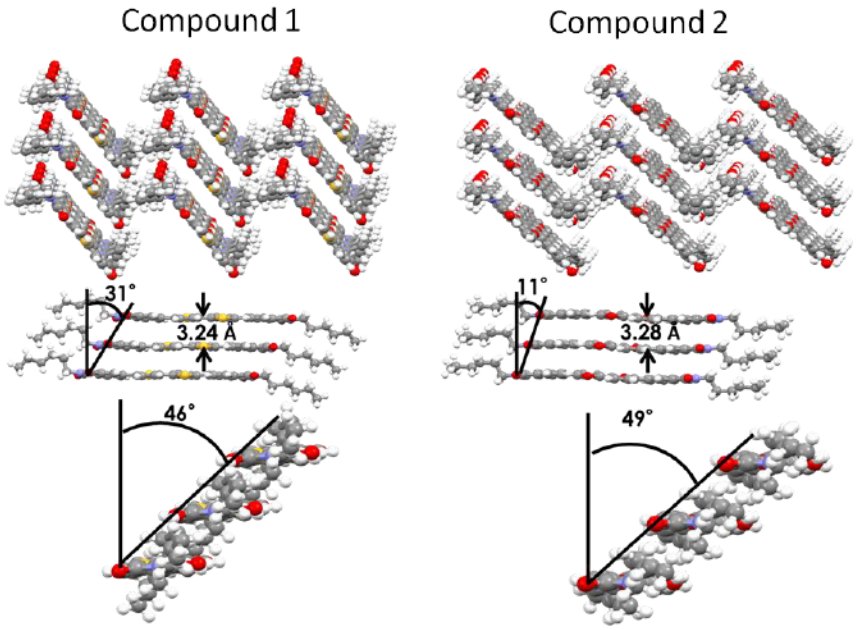

Figure 3.19. Single-crystal structures of compounds 1 and 2. Reproduced from[85] with permission from Elsevier.

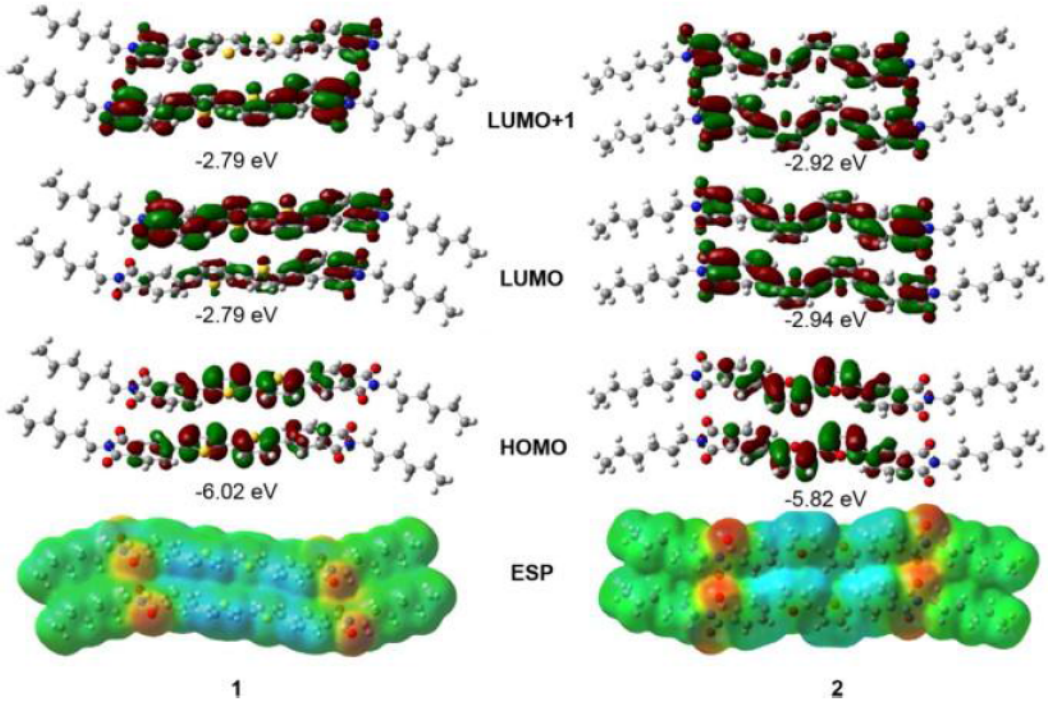

Figure 3.20. DFT calculated molecular orbitals and electrostatic potential maps of the dimer structures of compounds 1 and 2. Reproduced from[85] with permission from Elsevier.

3.3.5 Concluding Remarks

Despite the great extent of similarities between compound 1 and 2, the charge-transport capabilities are significantly different. While single-crystal structures and DFT calculations point to subtle changes in crystal packing and electronic structure, the origin of the complete loss of electron mobility in compound 2 remains unknown. However, as previously discussed in section 1.6, the phase relationship between transport levels has a large impact on mobility. TFTs made from different polymorphs of TIPS-pentacene can have mobilities varing by three orders of magnitude.[23] Despite the unknown mechanism, and the acknowledgement that furan may not be solely responsible, furan was not incorporated into subsequent acceptor molecules.

3.4 Core-Substituted Phthalimide-Thiophene Acceptors

In this round of molecules the phthalimide-thiophene end groups were preserved due to the acceptable electron mobilities previously measured. However, the alkyl chains on the terminal-imide nitrogen were modified to improve solubility. Instead of a straight-chain octyl group, branched ethylpropyl alkyl chains were used. The carbon attached to the imide nitrogen has a trigonal planar confirmation, in the plane of the molecule. Straight carbon chains that extend from this position tend to stay in the plane in the solid state, and have been observed to interdigitate with the alkyl chains from neighboring molecules and enhance crystallinity.[86] The branched ethylpropyl chains prefer to rotate along the N-C bond due to steric repulsion from the adjacent imide-oxygen atoms. This extends the remainder of the alkyl groups above and below the molecular plane, increasing π-π stacking distances and reducing crystallinity. Figure 3.21 shows the seven compounds used in this study, with electron-deficient cores substituted in the central position of the chromophore. Two donor materials that were used to make OPV devices, DTS(FBTTh$_2$)$_2$ and P3HT, are also shown in Figure 3.21. Arthur Hendsbee and Seth McAfee synthesized the acceptor compounds. This study has been published in the Journal of Materials Chemistry C.[87]

The UV-vis absorbance spectra of thin films of each acceptor compound and the two donor compounds are shown in Figure 3.22. From the perspective of complementary absorption, compounds 1,2 and 6 are well-suited to be blended with DTS(FBTTh$_2$)$_2$, while 3 and 7 are well-suited to be blended with P3HT. Compounds 4 and 5 have moderate spectral overlap with both donor compounds.

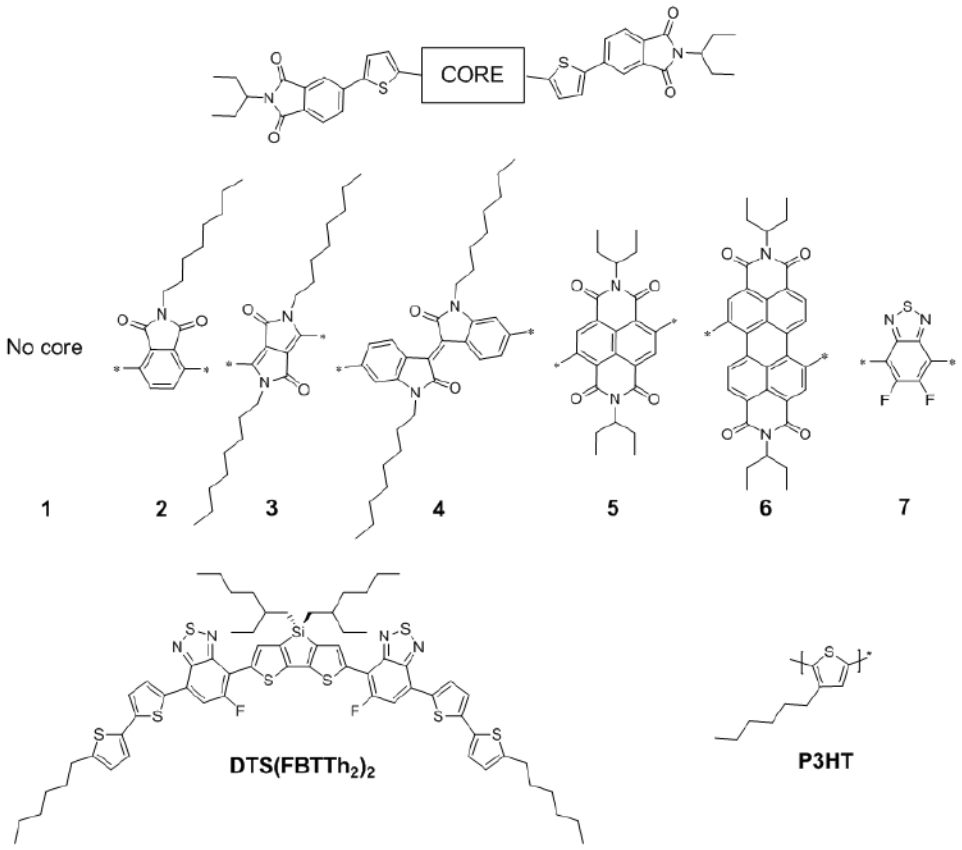

Figure 3.21. Core-substituted phthalimide-thiophene compounds and donor materials used in this study. Reproduced from[87] with permission from the Royal Society of Chemistry.

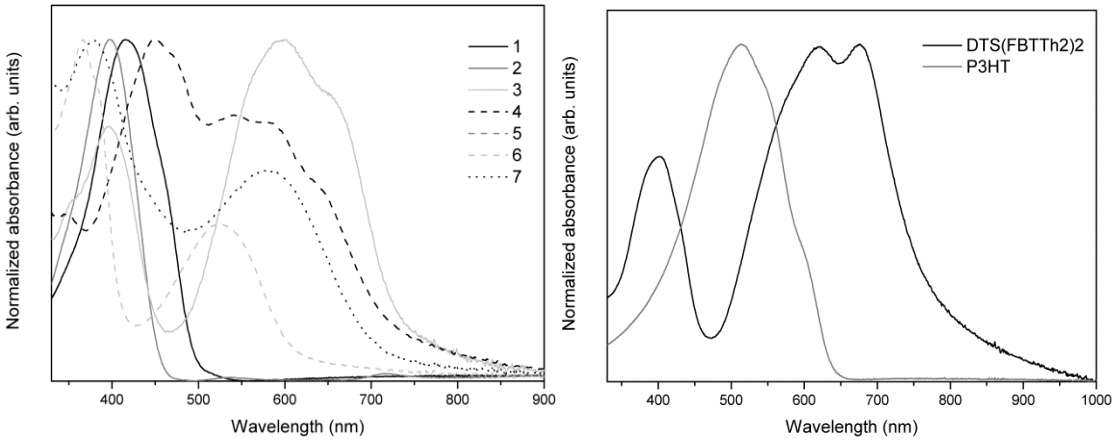

Figure 3.22. UV-vis absorbance spectra of thin films of compounds 1-7 (left panel), and the two donor compounds DTS($FBTTh_2$)$_2$ and P3HT (right panel), normalized to the peak absorbance in the visible spectrum. Reproduced from[87] with permission from the Royal Society of Chemistry.

3.4.1 Electronic Properties

The UPS spectra of compounds 1-7 are shown in Figure 3.23. The ionization energy of compound 1 has an intermediate value of 6.0 eV, compared to the two-thiophene compounds presented in section 3.2. Adding another electron-deficient phthalimide as the core in compound 2 increases the ionization energy to 6.1 eV. In compound 3 with a DPP core, the ionization energy of 5.4 eV is similar to the series of compounds presented in section 3.1. Similar to compound 3, compound 4 with an isoindigo core contains two amide groups. The ionization energy is expected to be similar to compound 3, yet has a larger value of 5.7 eV. Compound 5 with a naphthalene diimide core has an additional electron-withdrawing imide group compared to compound 2, yet also contains more π-electrons with the extra 6-member conjugated ring. The resulting ionization energy is equivalent to compound 2. Going from compound 5 to 6, there is an increase in the number of conjugated rings on the perylene diimide core, slightly lowering the ionization energy to 6.0 eV. Finally compound 7, with a difluorobenzothiadiazole core has an ionization energy of 5.9 eV.

3.4.2 Photovoltaic Devices

Since the acceptor molecules used in this study all had sufficient solubilities in chlorobenzene, bulk heterojunction OPV devices were fabricated by blending compounds 1-7 with a small molecule donor DTS($FBTTh_2$)$_2$, as well as a polymer donor P3HT. TFTs were omitted from this study since the photovoltaic performance was of greater importance to this project. Devices using DTS($FBTTh_2$)$_2$ as the donor were cast from 20 $mg \cdot mL^{-1}$ solutions in chlorobenzene with 1:1 weight ratios of donor and acceptor. 0.4 % v/v DIO was used as an additive. Devices were spun at 1000 rpm and annealed at 70 °C for 10 minutes. Devices using P3HT as the donor were cast under similar conditions, except DIO was omitted and annealing temperatures were optimized in 10 °C increments for each compound. The overall device architecture in all cases was ITO/BHJ/Ca/Al. Figure 3.24 shows the JV curves of the best performing devices. Performance metrics are listed in Table 3.4, along with optimized annealing temperatures for P3HT devices.

There are significant differences in performance for the various acceptor compounds when a different donor is used. Compounds 1 and 2 show almost no PCE with blended with DTS($FBTTh_2$)$_2$, yet achieve modest PCEs of ~ 0.5 % when blended with P3HT. Compounds 3, 6, and 7 showed comparatively-low performance with either donor, and compounds 4 and 5 showed better performance with DTS($FBTTh_2$)$_2$ than P3HT. The best performing compound with DTS($FBTTh_2$)$_2$ is compound 4. From the EQE spectra in panel c) of Figure 3.24, contribution to the short-circuit current can be seen where DTS($FBTTh_2$)$_2$ has a transmission window around 475 nm, indicating that compound 4 is successfully transferring holes to DTS($FBTTh_2$)$_2$ at the D/A interface. Similarly, in panel d) of Figure 3.24, in spectra of compounds 1 and 2 contributions to the short-circuit current can be observed where P3HT does not absorb.

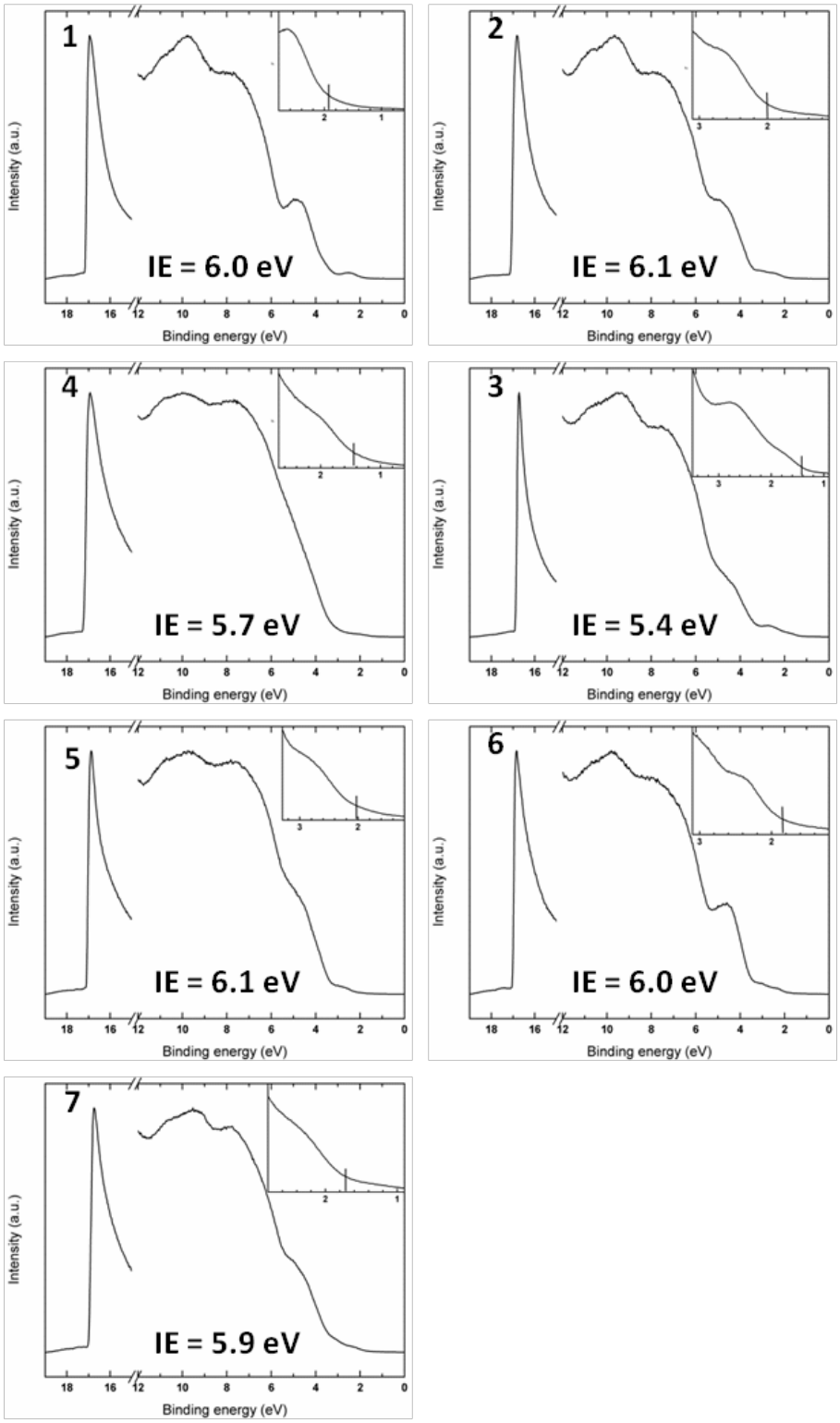

Figure 3.23. UPS spectra of compounds 1-7, with calculated ionization energies. Vertical lines in the insets indicate locations of valence band maxima. Uncertainties in calculated ionization energies are ± 0.1 eV. Reproduced from[87] with permission from the Royal Society of Chemistry.

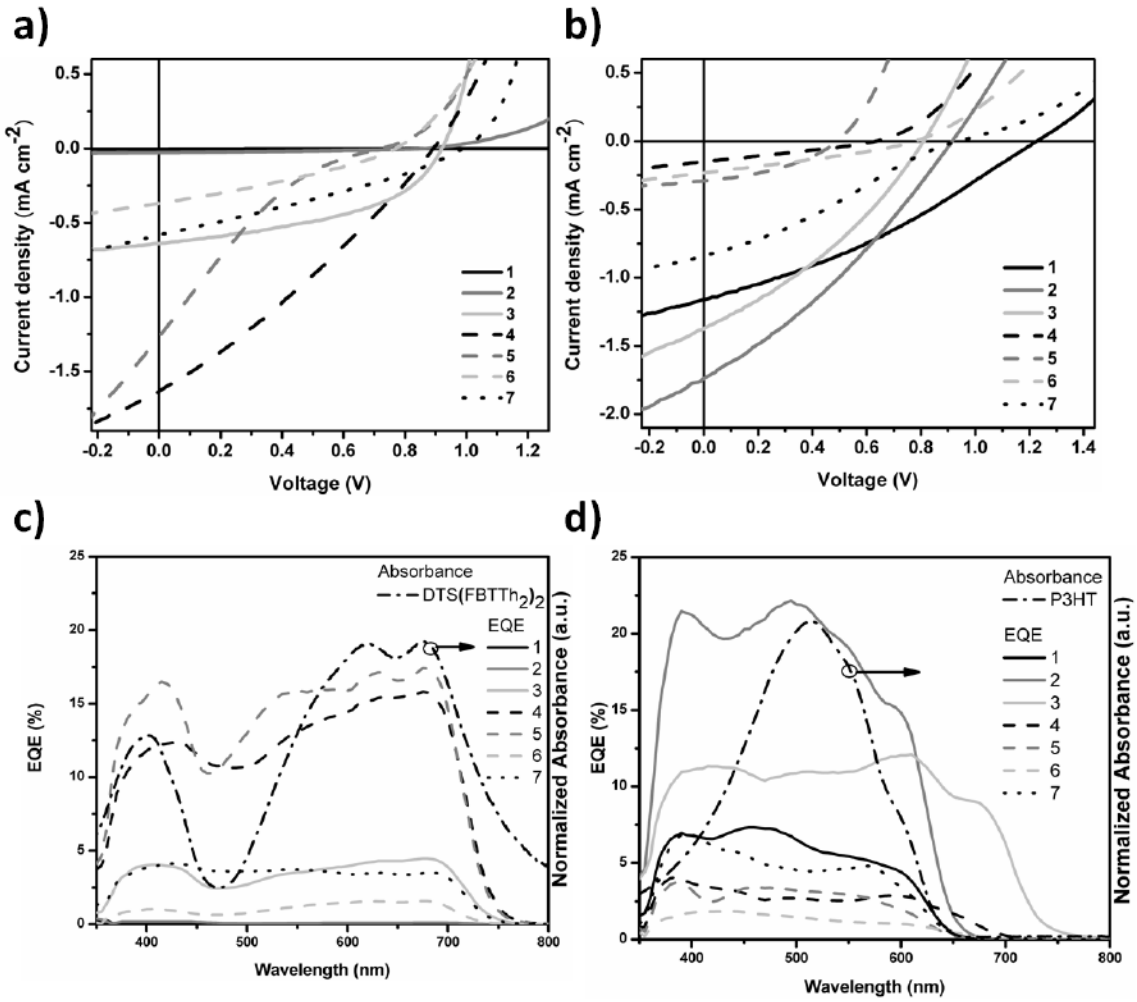

Figure 3.24. JV curves (a-b) and EQE spectra (c-d) of OPV devices made from compounds 1-7 and a,c) DTS(FBTTh$_2$)$_2$ and b,d) P3HT. Reproduced from[87] with permission from the Royal Society of Chemistry.

In principle, the EQE spectra can be integrated to reproduce the short-circuit current density. There are a few cases in Figure 3.24 where these values do not seem to correspond. In panel d) for example, compound 2 appears to have an integrated current density three times larger than compound 1, yet the measured short-circuit current density is only 40 % larger. This is an indication of bimolecular recombination-limited performance, where the recombination rate depends on the carrier density squared. Without a white-light bias, EQE is measured at a much lower intensity since the incident light passes through a monochromator before reaching the device. The resulting carrier

densities are significantly lower and bimolecular recombination becomes less significant in this operating regime.

Table 3.4. JV performance metrics and annealing temperatures of OPV devices made from compounds 1-7 and DTS(FBTTh$_2$)$_2$ and P3HT. The numbers in each performance metric cell represent the best performing device and the (average) values. Reproduced from[87] with permission from the Royal Society of Chemistry.

Donor	Acceptor	Annealing temperature (°C)	V_{oc} (V)	Jsc (mA·cm^{-2})	PCE (%)	FF
DTS(FBTTh$_2$)$_2$	1	70	1.20 (1.13)	-0.0033 (-0.0024)	0.00051 (0.00037)	0.13 (0.14)
	2	70	0.86 (0.85)	-0.028 (-0.025)	0.0086 (0.0072)	0.37 (0.38)
	3	70	0.92 (0.94)	-0.64 (-0.47)	0.27 (0.19)	0.46 (0.42)
	4	70	0.89 (0.84)	-1.6 (-1.4)	0.43 (0.33)	0.29 (0.29)
	5	70	0.72 (0.72)	-1.3 (-1.1)	0.15 (0.13)	0.17 (0.15)
	6	70	0.77 (0.77)	-0.37 (-0.30)	0.089 (0.071)	0.31 (0.30)
	7	70	0.99 (0.97)	-0.58 (-0.54)	0.17 (0.16)	0.30 (0.30)
P3HT	1	130	1.23 (1.18)	-1.2 (-1.1)	0.46 (0.36)	0.32 (0.32)
	2	130	0.92 (0.95)	-1.7 (-1.2)	0.50 (0.32)	0.31 (0.29)
	3	70	0.81 (0.79)	-1.4 (-1.2)	0.37 (0.28)	0.33 (0.31)
	4	70	0.63 (0.60)	-0.15 (-0.14)	0.027 (0.025)	0.28 (0.29)
	5	70	0.49 (0.50)	-0.29 (-0.23)	0.056 (0.049)	0.39 (0.44)
	6	70	0.78 (0.76)	-0.23 (-0.18)	0.054 (0.040)	0.30 (0.29)
	7	130	0.94 (0.94)	-0.84 (-0.80)	0.22 (0.20)	0.28 (0.27)

To understand the origin of the drastic differences in device performance, AFM was used to image the topography of the blend films. Images of blend films with DTS(FBTTh$_2$)$_2$ are shown in Figure 3.25, and images of blend films with P3HT are shown in Figure 3.26.

The goal in making bulk heterojunction films is to create donor and acceptor domain sizes that are comparable to exciton diffusion lengths of ~ 20 nm such that absorbed energy can be separated as free charge carriers at a D/A interface. Referring to Figure 3.24, compounds 1 and 2, which gave close to zero PCE with DTS(FBTTh$_2$)$_2$, show features with length scales on the order of 1 μm. Compound 4 showed the best performance with DTS(FBTTh$_2$)$_2$, and the corresponding AFM images show features with length scales closer to 100 nm. The AFM images in Figure 3.26 show a smaller difference in feature sizes between compounds. However, the devices also exhibited smaller differences in PCE.

3.4.3 Concluding Remarks

From the seven compounds analyzed in this study, compound 4 using isoindigo as the central moiety gave the best performance when blended with DTS(FBTTh$_2$)$_2$. With P3HT, compounds 1 and 2 were found to give the best performance. In all cases the overall PCEs were strongly correlated with the blend film morphology, as determined using AFM. Analysis of the EQE spectra show that contributions to the current density cannot solely be attributed to the donor, indicating that these compounds are fulfilling their role as acceptors by both transporting electrons and undergoing complementary absorption.

3.5 Chapter 3 Summary

Following the results achieved in section 3.4, the isoindigo-containing material (compound 4) was chosen for further optimization by Seth McAfee and Jessica Topple. After extensive structural evolution of the acceptor molecule and optimization of processing conditions using DTS(FBTTh$_2$)$_2$ as the donor, they achieved PCEs of 2 %.[88–90] However, after three years of working with acceptors using phthalimide and naphthalimide end groups with relatively small gains in performance, an alternative strategy of using perylene diimide-based acceptors was adopted. These results are presented in Chapter 4.

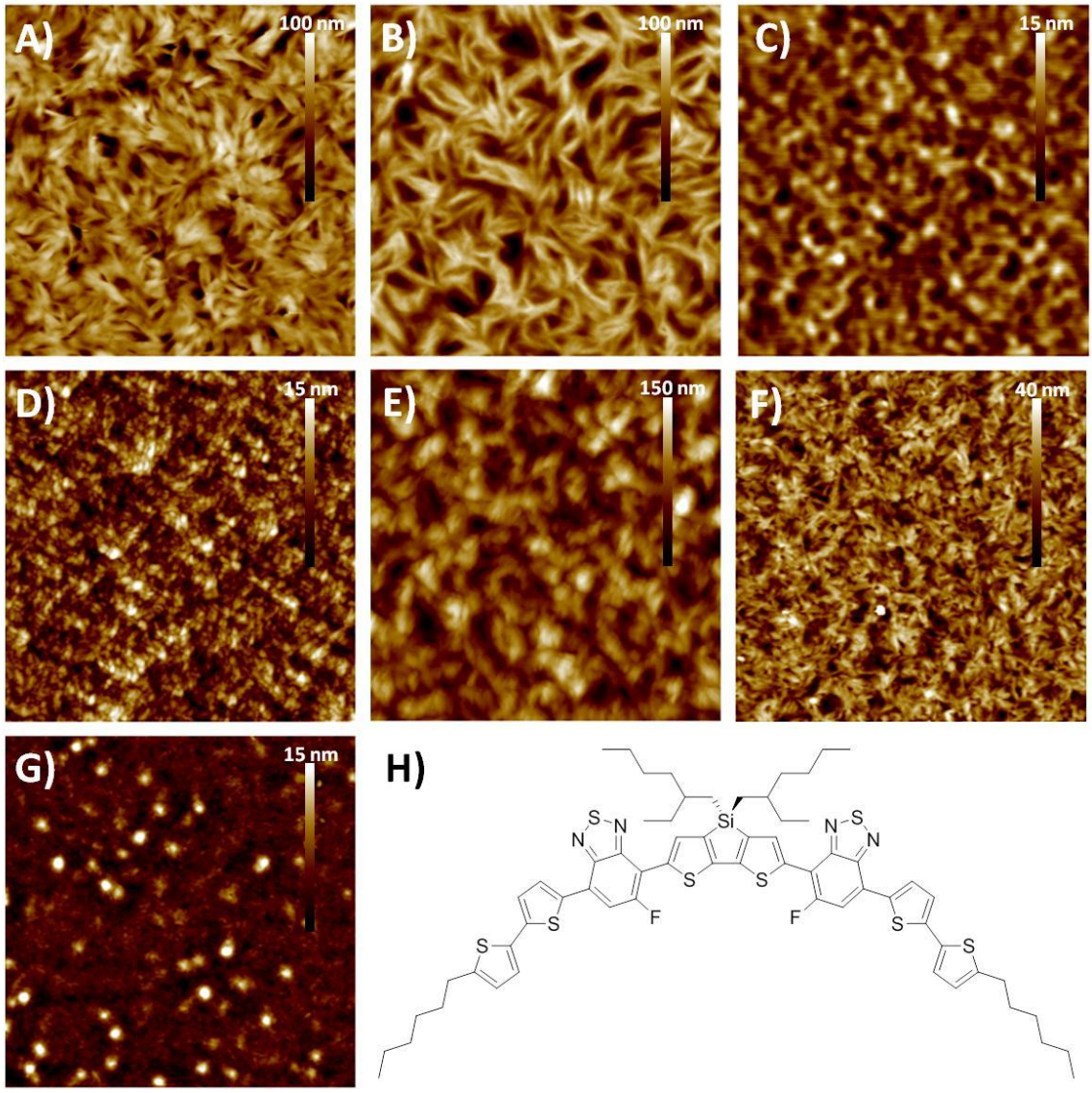

Figure 3.25. a-g) AFM topography images of blend films of compounds 1-7, respectively, with DTS(FBTTh$_2$)$_2$, and h) the chemical structure of DTS(FBTTh$_2$)$_2$. AFM images are 5 µm x 5 µm. Vertical contrast bars show height variations in sample surfaces. Reproduced from[87] with permission from the Royal Society of Chemistry.

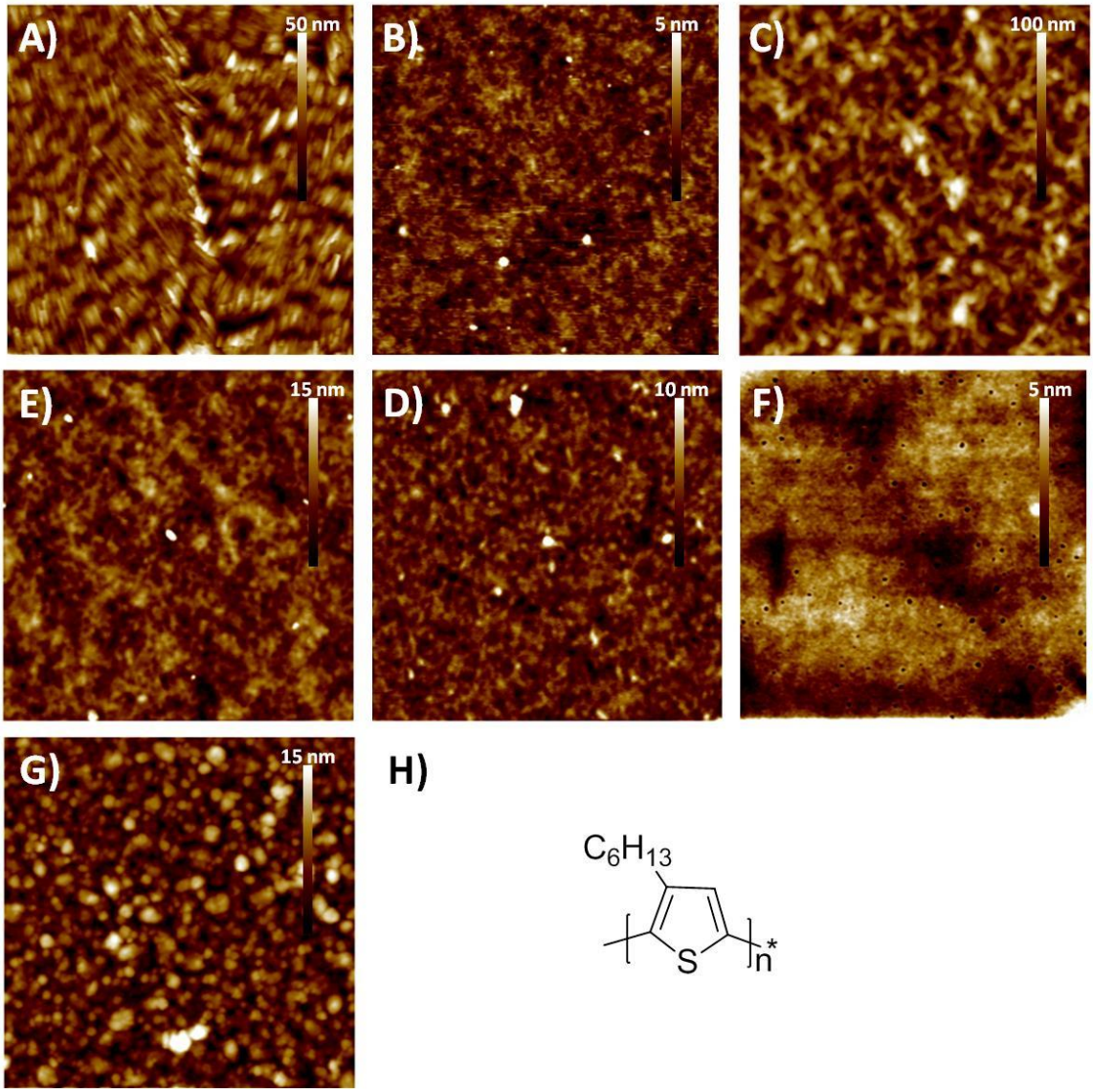

Figure 3.26. a-g) AFM topography images of blend films of compounds 1-7, respectively, with P3HT, and h) the chemical structure of P3HT. AFM images are 5 µm x 5 µm. Vertical contrast bars show height variations in sample surfaces. Reproduced from[87] with permission from the Royal Society of Chemistry.

CHAPTER 4 PERYLENE DIIMIDE NON-FULLERENE ACCEPTORS

This chapter describes the characterization and integration into devices of a family of chromophores utilizing perylene diimide as the main synthetic building block.

4.1 PERYLENE DIIMIDE MONOMERS WITH BRANCHED-ALKYL CHAINS

Perylene-3,4,9,10-tetracarboxylic diimide (PTCDI or PDI, herein referred to as the latter) is an appealing chromophore to use in OPV applications due to its large molar absorption coefficient, large electron affinity, excellent thermal and photochemical stability, and high electron mobility achieved by various PDI derivatives in TFT devices.[91–94] The ionization energy of dimethyl-PDI has previously been measured via UPS to be 6.6 ± 0.1 eV, making it a good candidate for an acceptor molecule.[95] The first reported bilayer OPV device used a PDI derivative as the acceptor,[26] and recent solution-processed BHJ OPV devices have used bay- and ortho-substituted monomers,[96,97] imide-linked dimers,[49,98] and bay-linked dimers,[99–101] trimers,[102,103] and tetramers as acceptor materials.[104] Figure 4.1 shows the available sites for attaching chemical groups on a PDI monomer, as well as the various assortments of alkyl-substituted PDIs and multi-chromophore molecules used as electron acceptors in OPVs.

The simplest PDI monomer derivatives are substituted with alkyl chains at the imide nitrogen position. Yet despite the molecular complexity of the previously-listed PDI acceptor molecules, simply-substituted monomers at the *N*-position are less thoroughly investigated. As of 2016 only *t*-butylphenyl,[105] 1-ethylpropyl,[106–117] 1-hepyloctyl,[109] 1-nonyldecyl,[118] and an asymmetric *N*-1-ethylpropyl-*N'*-1-heptyloctyl substituted-PDI have been reported in OPV devices,[119,120] with 1-ethylpropyl (EP) being the dominant molecule of study. The best-performing donor with EP-PDI is DTS(FBTTh$_2$)$_2$, achieving PCEs of 3 %.[114,116] However, the strong crystalline tendencies of the donor and acceptor lead to large non-uniformities in spin-cast films, resulting in spatially-dependent performance of devices on substrates. To

address this issue, four *N*-alkyl substituted PDIs were investigated to determine the effect of alkyl-chain substitution on device performance and film uniformity, shown in Figure 4.2. Alexander Dobson and Arthur Hendsbee synthesized the PDI materials used in this study, and measured the solubilities in chloroform. This study has been published in Organic Electronics.[121]

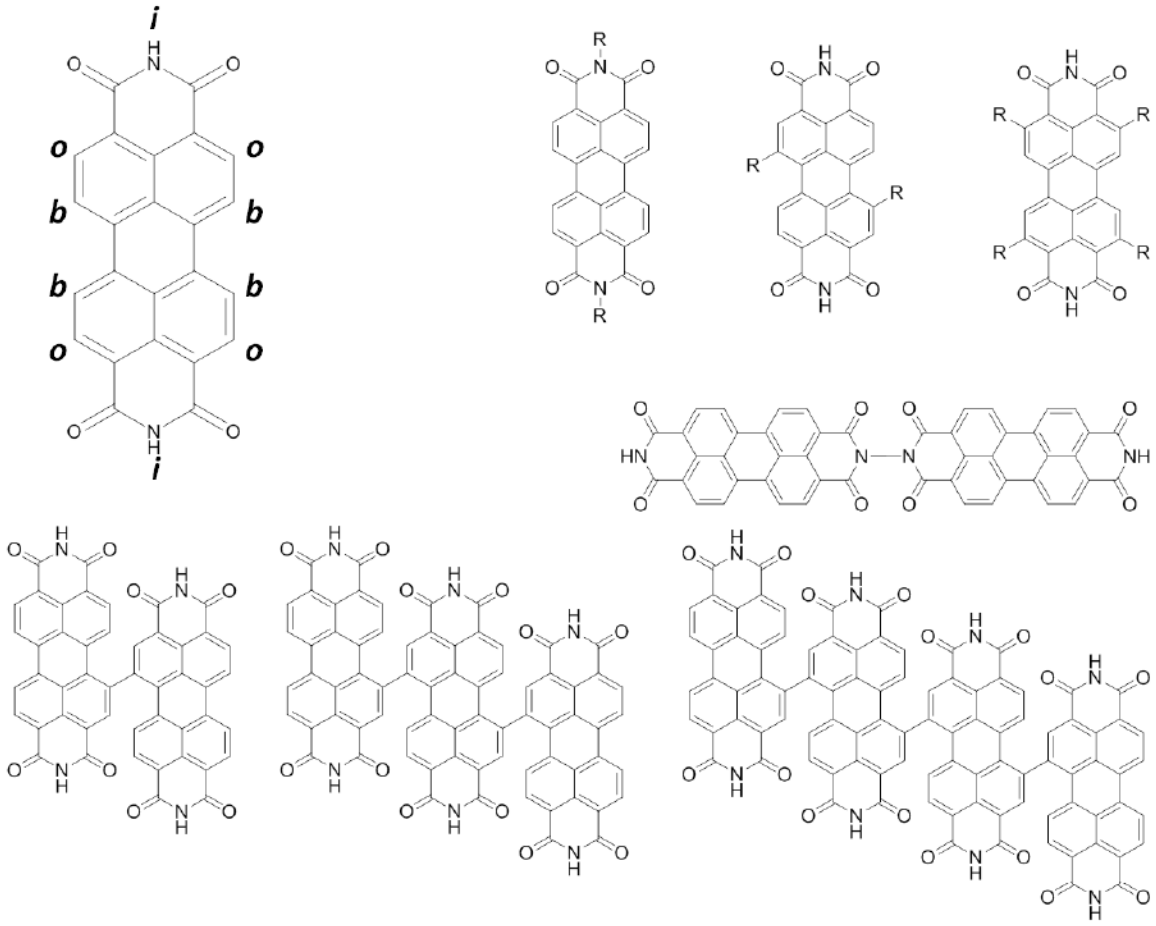

Figure 4.1. PDI monomer showing imide (*i*), bay (*b*), and ortho (*o*) positions; PDI monomers with various alkyl substitutions; and dimer, trimer, and tetramer PDI arrangements.

4.1.1 PDI Solubilities

UV-vis spectroscopy was used to determine the solubilites of the four PDI molecules in chloroform by filtering saturated PDI solutions, diluting by a known amount, and comparing the peak absorbance of each solution to a calibration curve of peak absorbance versus concentration. The resulting solubilities were EP: 7.0, PB: 60, EH: 6.6, and HO: 40 $mg \cdot mL^{-1}$. Despite the significantly larger alkyl chains on EH versus EP, the solubilities were approximately the same. The branching point at carbon 2 on EH allows the alkyl chains to diverge in-plane with the molecule. When the branching point occurs on carbon 1, the alkyl chains diverge out of plane, due to steric repulsion from the adjacent imide oxygens. Out-of-plane divergence hinders π-π interactions between adjacent chromophores, thus decreasing the tendency to crystallize and increasing solubililty.[122] This can be seen in the change in solubility between EP and PB, where PB is expected to result in larger steric repulsion between chromophores. However, when using significantly larger chains that branch at the first carbon, the solubility of HO is reduced compared to PB. It is expected that at some alkyl-chain length, attractive interchain interactions will begin to dominate solution behavior.

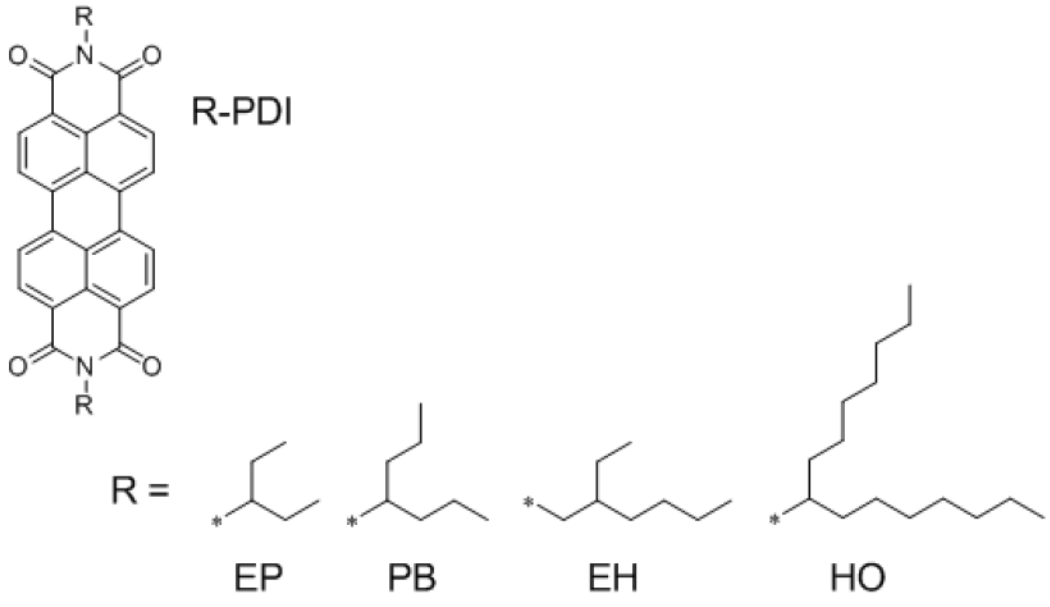

Figure 4.2. *N*-alkyl substituted PDIs used in this study. Reproduced from[121] with permission from Elsevier.

4.1.2 Film Properties

The UV-vis spectra of solutions in chloroform, and thin films spun from 10 mg·mL^{-1} solutions in chloroform are shown in Figure 4.3. The solution spectra are all nearly identical, with absorbance maxima at 526 nm corresponding to the 0-0 vibronic transition.[123] This is not surprising given that the imide nitrogens lie on nodal planes of both the HOMO and LUMO, so alkyl-chain substitutions at this atoms should not affect the optical properties in dilute solutions.[124,125] The thin-film spectra of the three PDIs with branching points on carbon 1 (EP, PB, HO) have similar features. The absorbance onsets are red shifted to approximately 600 nm, with the 0-1 vibronic peak at ~ 500 nm having the largest intensity. EH, with the branching point at carbon 2, has a noticeably different thin-film absorbance spectrum. The additional peak at ~ 575 nm has been previously observed in PDI aggregates and is attributed to electronic coupling between closely-spaced adjacent chromophores.[126,127] For reference, the thin-film absorbance spectrum of DTS(FBTTh$_2$)$_2$ can be seen in Figure 3.22.

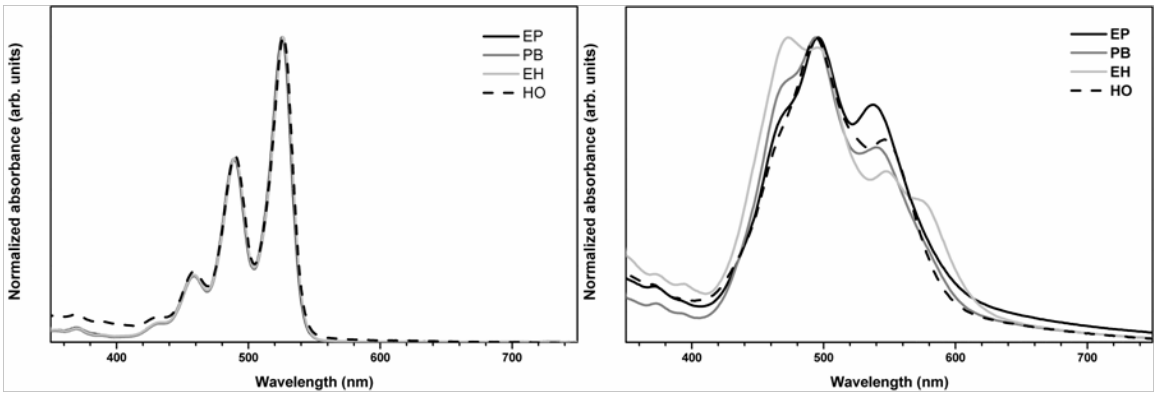

Figure 4.3. Solution (left panel) and thin-film (right panel) UV-vis spectra of PDI molecules used in this study. Reproduced from[121] with permission from Elsevier.

4.1.3 Photovoltaic Devices

Each PDI molecule was blended with DTS(FBTTh$_2$)$_2$ using previously reported conditions for EP.[114] 1:1 weight ratio solutions with total dye loading of 30 mg·mL^{-1} in chlorobenzene with 0.4 % v/v 1,8-diiodooctane additive were cast at 90 °C at 1500 rpm on top of PEDOT:PSS-coated substrates. Figure 4.4 shows photographs (top row),

circularly-polarized transmission optical microscopy (*c*-pol-TOM) (middle row), and AFM topography images (bottom row) of the blend films. Panel a) shows the aforementioned heterogeneity of films with EP.

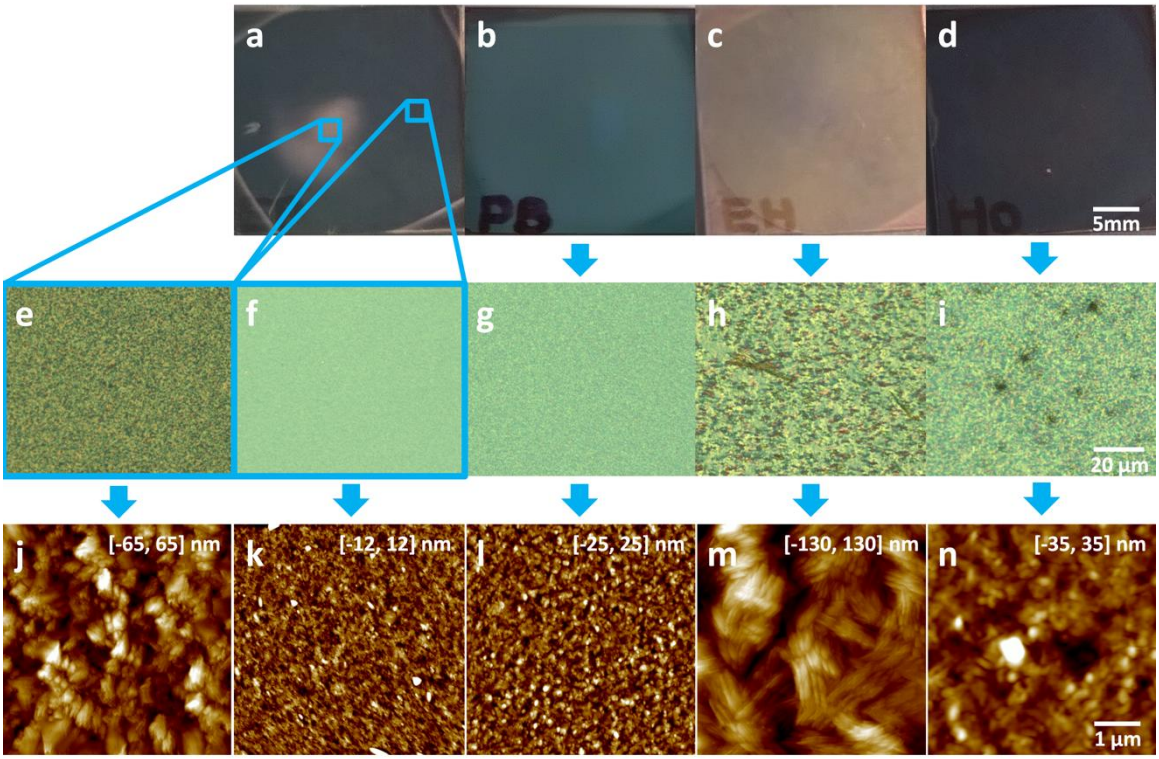

Figure 4.4. Photographs (top row), *c*-pol-TOM images (middle row), and AFM topographical images (bottow row) of blend film of DTS(FBTTh$_2$)$_2$:R-PDI. The white scale bar indicates lateral scale of all images in the same row. The "[-x,x] nm" on each AFM image indicates the height range of topographical features, with darker regions corresponding to negative height regions. R = EP: a, e, f, j, k. PB: b, g, l. EH: c, h, m. HO: d, i, n. Reproduced from[121] with permission from Elsevier.

The transparent region AFM images (panel k) show features with 25-50 nm length scales, while the opaque region AFM images (panel j) show features on the order of 100-300 nm. The other three PDIs form blend films (panels b-d) that are macroscopically more uniform, although only PB had AFM images with features with moderately acceptable length scales (50-70 nm, panel l) for OPV devices. EH, which showed the strongest crystalline tendencies of the group, showed elongated grains approximately 60 x 300 nm

in size with a large surface roughness (panel m). HO, while producing relatively smoother films than EH, also exhibited large features approximately 200-300 nm in size (panel n).

OPV devices were fabricated using identical casting conditions, with a device architecture of ITO/PEDOT:PSS/BHJ/PDIN/Ag. The role of PDIN has been discussed in section 2.2. JV curves of the best-performing devices are shown in Figure 4.5, with device metrics listed in Table 4.1. EP devices had the best performance. However, the PCE depended strongly on where the device was located on the film. In the transparent regions, the average PCE was ~ 3 %. In the center of the opaque regions the devices behaved as shorts, similar to the JV curve of EH in Figure 4.5. In the regions around the perimeter of the opaque areas, the devices had a lower average PCE of ~ 2.2 %. EH devices all behaved as shorts with a very low V_{oc} (~ 2 mV), due to the rough crystalline film morphology resulting in shunt paths between the cathode and anode. PB and HO had the best uniformity among devices, reflective of the smooth, uniform blend films shown in Figure 4.4.

4.1.4 Concluding Remarks

This study highlighted the strong dependence of the film-forming properties of PDI monomers on the alkyl chains at the imide nitrogen positions. To reduce crystallinity, the branching point of the alkyl chain should be at carbon 1 to enhance steric repulsion between adjacent PDI molecules. The macroscopic film uniformity improved with longer alkyl chains at the cost of reduced performance. However, crystalline donor and acceptor domains are desirable for enhanced charge and exciton transport,[22,34] so long as the domain sizes are small enough for excitons to reach a D/A interface. This balance between crystallinity and domain size in all small-molecule blends has proven to be a difficult obstacle in achieving high-performance non-fullerene systems.

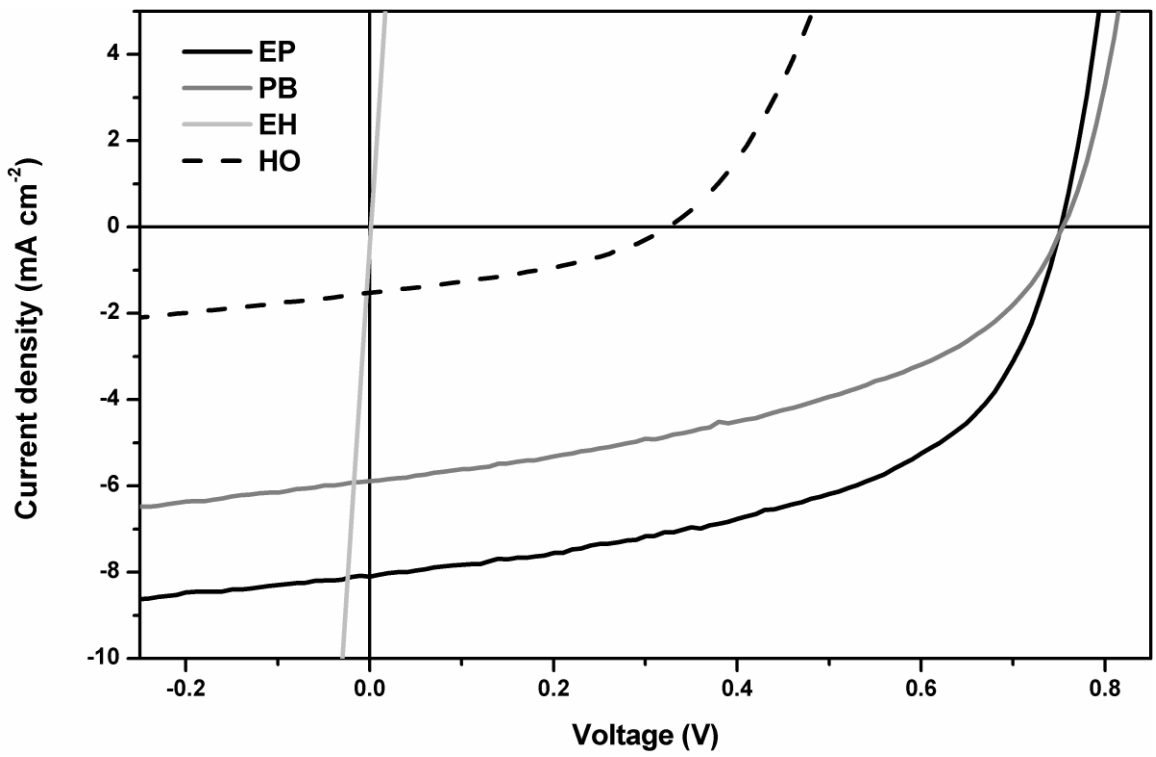

Figure 4.5. JV curves of OPV devices made from DTS(FBTTh$_2$)$_2$ and the PDI molecules used in this study. Reproduced from[121] with permission from Elsevier.

Table 4.1. JV performance metrics of OPV devices made from DTS(FBTTh2)2 and the PDI molecules used in this study. The numbers in each cell represent best and (average) values. EH devices showed negligible PCE and FF. Reproduced from[121] with permission from Elsevier.

PDI	V_{oc} (V)	J_{sc} (mA·cm^{-2})	PCE (%)	FF
EP	0.75 (0.75)	-8.1 (-7.2)	3.2 (2.8)	0.53 (0.51)
PB	0.75(0.75)	-5.9 (-5.6)	2.0 (1.7)	0.45 (0.42)
EH	0.002 (0.002)	-0.42 (-0.35)	-	-
HO	0.32 (0.32)	-1.5 (-1.4)	0.19 (0.17)	0.38 (0.37)

4.2 Bay-Linked Perylene Diimide Dimers

Based on the results of the previous section, PDI monomers were deemed to be too crystalline to be used directly as acceptors. Increasing the solubility by adjusting the alkyl chains led to reduced performance. Another strategy that has been shown to be useful for improving the film-forming behavior of PDIs is creating dimers by linking two PDI

monomers at the bay position.[99–101] Steric repulsion between the linked monomers results in a large dihedral angle between the monomer molecular planes, reducing crystallinity and improving film morphologies. In this study, bay-linked PDI dimers were synthesized to address the issue of over crystallization in donor:acceptor blend films. To further exploit available positions for functionalization, nitrogen atoms were annulated on the outer bay positions of the dimers to tether additional alkyl chains. Additionally, polymer donors PTB7 and PTB7-Th (Figure 4.6) were used in place of a small molecule donor. Polymers tend to phase separate in blend films on longer time scales than small molecules, resulting in films with smaller domain sizes upon drying. Figure 4.6 illustrates the materials used in this study. Arthur Hendsbee synthesized the PDI materials. This study was published in Chemistry of Materials.[128]

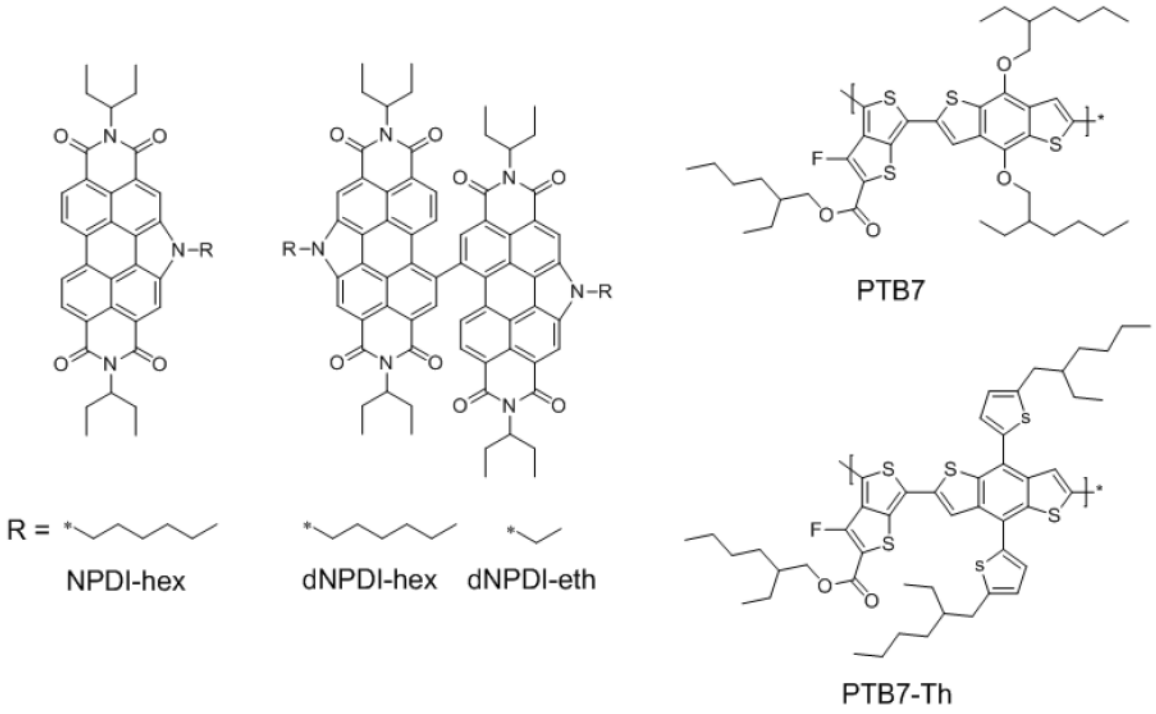

Figure 4.6. N-annulated acceptors and polymer donors used in this study. Reprinted with permission from[128]. Copyright 2016 American Chemical Society.

The thin-film absorbance spectra of donor and acceptor dyes used in this study are presented in Figure 4.7, showing complementary absorbance across most of the visible spectrum. The UPS spectra of the three acceptor molecules are presented in Figure 4.8, with sufficiently large calculated ionization energies ranging between 5.7-6.0 eV.

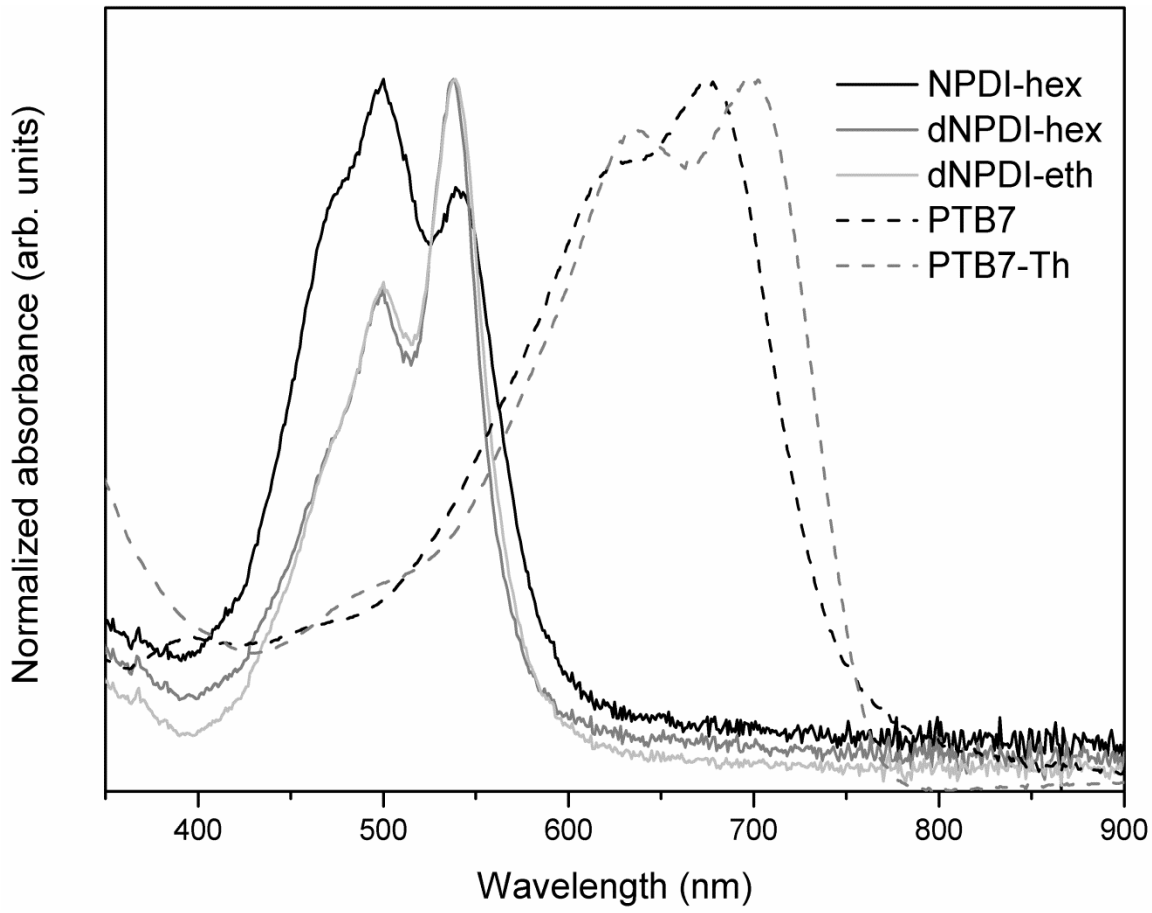

Figure 4.7. UV-vis absorbance spectra of thin films of N-annulated PDI molecules and the two donor polymers PTB7 and PTB7-Th, normalized to the peak absorbance in the visible spectrum. Reprinted with permission from[128]. Copyright 2016 American Chemical Society.

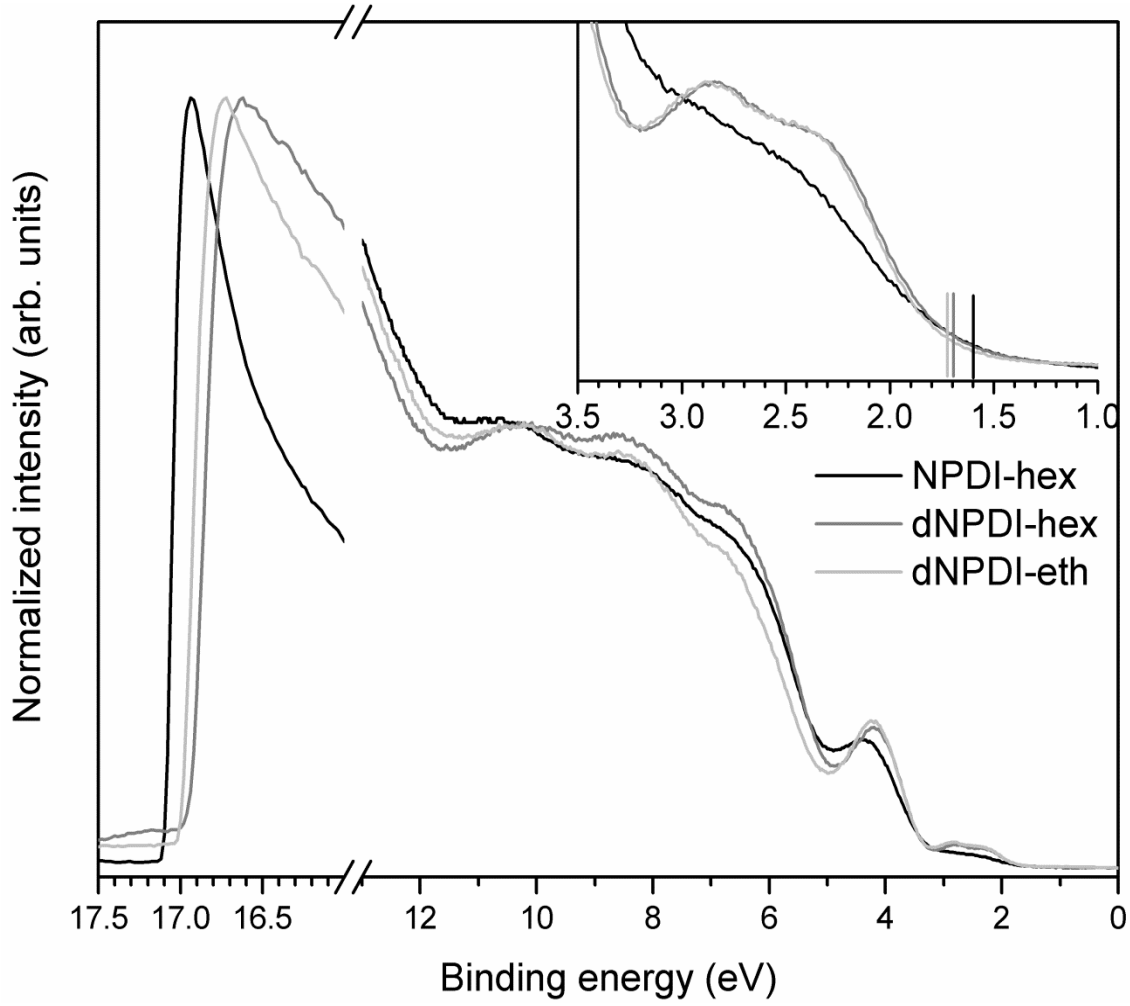

Figure 4.8. UPS spectra of NPDI-hex, dNPDI-hex, and dNPDI-eth with calculated ionization energies of 5.7 ± 0.1, 6.0 ± 0.1, and 5.9 ± 0.1 eV, respectively. Vertical lines denote the locations of the valence band maxima. Reprinted with permission from[128]. Copyright 2016 American Chemical Society.

4.2.1 Photovoltaic Devices

dNPDI-hex was blended with PTB7 with a dye loading of 25 mg·mL^{-1}, spun at 1500 rpm. An inverted architecture of ITO/ZnO/BHJ/MoO_3/Ag was chosen since recent work has shown that PDIs tend to enrich at the PEDOT:PSS interface in standard architecture devices, while adopting a more uniform vertical distribution on ZnO-coated substrates in inverted architecture devices.[129] A donor:acceptor weight ratio of 50:50 produced better performance, and when 8 % v/v DIO was added the devices achieved 2.2 % PCE.

This is a relatively large amount of solvent additive. Since the DIO remains in the film until the devices are placed under vacuum for MoO_3 deposition,[55] the amount of time between film casting and evaporation needs to be precisely controlled to achieve reproducible results. Otherwise the residual solvent additive in the film promotes reorganization and phase separation. Following this result, the monomer version NPDI-hex was blended with PTB7 under similar conditions, and a 40:60 weight ratio with only 4 % v/v DIO achieved a similar PCE of 1.9 %. Since DIO is a poor solvent for both PTB7 and the PDI chromophore,[116] it was rationalized that the long hexyl chains at the bay-nitrogen position hindered PDI dimer crystalline domain formation, requiring large amount of DIO. A second derivative of the dimer with shorter ethyl chains was synthesized, dNPDI-eth. This time the best performing devices used a weight ratio of 50:50 with only 3 % v/v DIO, achieving a PCE of 3.1 %. The JV curves of these devices are shown in Figure 4.9, with performance metrics listed in Table 4.2.

Another commonly used polymer with PDI acceptors is PTB7-Th. dNPDI-hex and dNPDI-eth devices were fabricated using PTB7-Th as the donor, using the same casting conditions as above. In addition, DIO-free solutions were also investigated. The JV curves of these devices are shown in Figure 4.10, with performance metrics listed in Table 4.3. Substituting the donor material had a significant effect on device performance, with both dimer molecules achieving PCEs better than 5 %. Interestingly, DIO had a very subtle effect on performance, slightly lowering overall PCEs.

To understand the significant performance increase upon substituting the donor material, EQE spectra and AFM images of the blend films for dNPDI-eth with PTB7 and PTB7-Th are shown in Figure 4.11. The shape of the EQE spectra are nearly identical, with overall efficiency higher for PTB7-Th films, reflective of the larger magnitude J_{sc}. Comparing the AFM topography images in panels b) and c), the PTB7-Th blends show finer structure than PTB7 blends. This is an indication that the overall performance of these devices is morphology limited, with domain size restricting the number of excitons reaching a D/A interface.

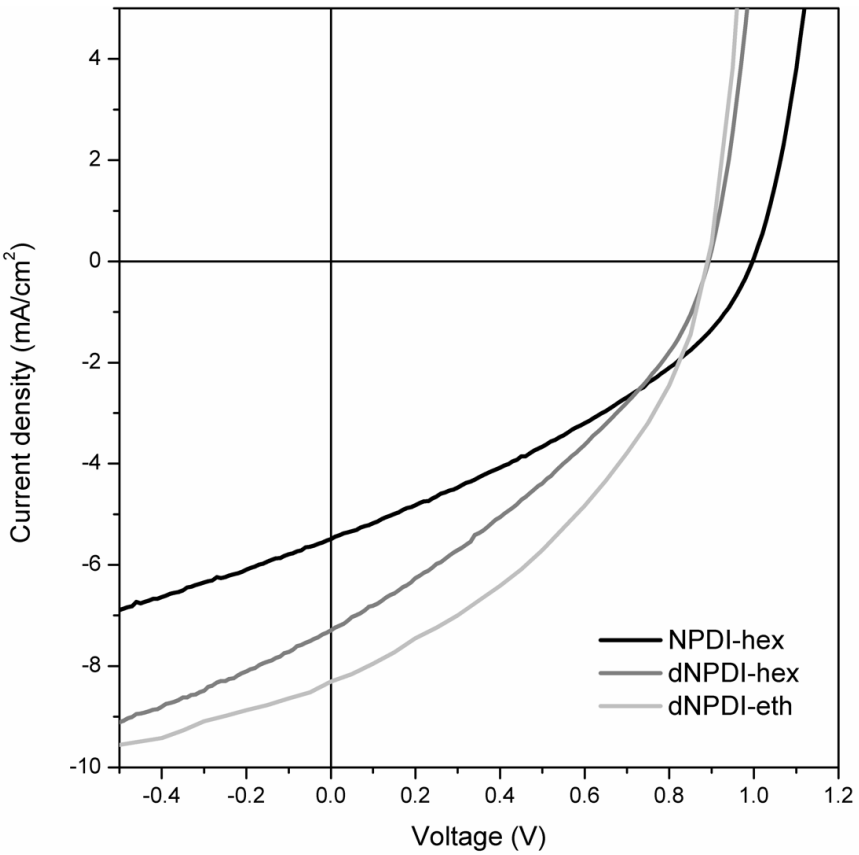

Figure 4.9. JV curves of OPV devices made from PTB7 and the PDI molecules used in this study. Reprinted with permission from[128]. Copyright 2016 American Chemical Society.

Table 4.2. JV performance metrics of OPV devices made from PTB7 and the PDI molecules used in this study. The numbers in each cell represent best and (average) value. Reprinted with permission from[128]. Copyright 2016 American Chemical Society.

Acceptor	Weight ratio	DIO (% v/v)	V_{oc} (V)	Jsc (mA·cm^{-2})	PCE (%)	FF
NPDI-hex	40:60	4	1.00 (1.00)	-5.49 (-5.18)	1.9 (1.8)	0.35 (0.35)
dNPDI-hex	50:50	8	0.89 (0.90)	-7.29 (-6.87)	2.2 (2.1)	0.34 (0.34)
dNPDI-eth	50:50	3	0.91 (0.90)	-8.55 (-8.24)	3.1 (3.0)	0.40 (0.40)

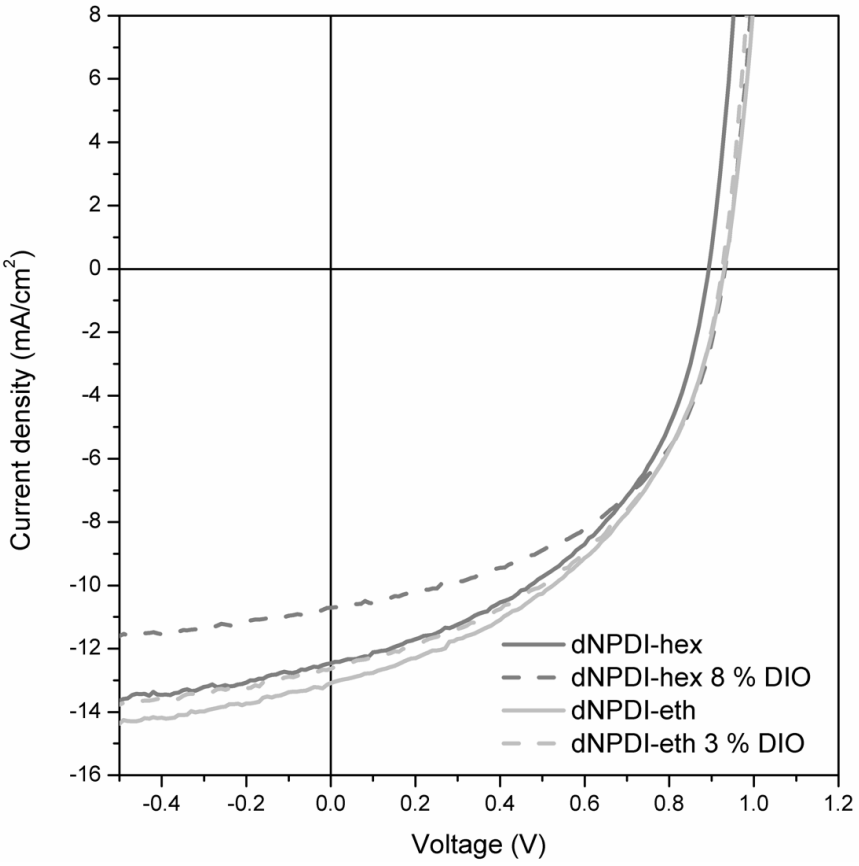

Figure 4.10. JV curves of OPV devices made from PTB7 and the PDI molecules used in this study. Reprinted with permission from[128]. Copyright 2016 American Chemical Society.

Table 4.3. JV performance metrics of OPV devices made from PTB7-Th and the PDI molecules used in this study. The numbers in each cell represent best and (average) value. Reprinted with permission from[128]. Copyright 2016 American Chemical Society.

Acceptor	Weight ratio	DIO (% v/v)	V_{oc} (V)	Jsc (mA·cm^{-2})	PCE (%)	FF
dNPDI-hex	50:50	0	0.89 (0.90)	-11.8 (-11.6)	5.1 (5.0)	0.49 (0.47)
dNPDI-hex	50:50	8	0.93 (0.92)	-10.5 (-10.7)	5.0 (4.8)	0.51 (0.50)
dNPDI-eth	50:50	0	0.93 (0.93)	-13.1 (-12.5)	5.5 (5.3)	0.45 (0.45)
dNPDI-eth	50:50	3	0.93 (0.92)	-12.6 (-12.2)	5.4 (5.2)	0.47 (0.46)

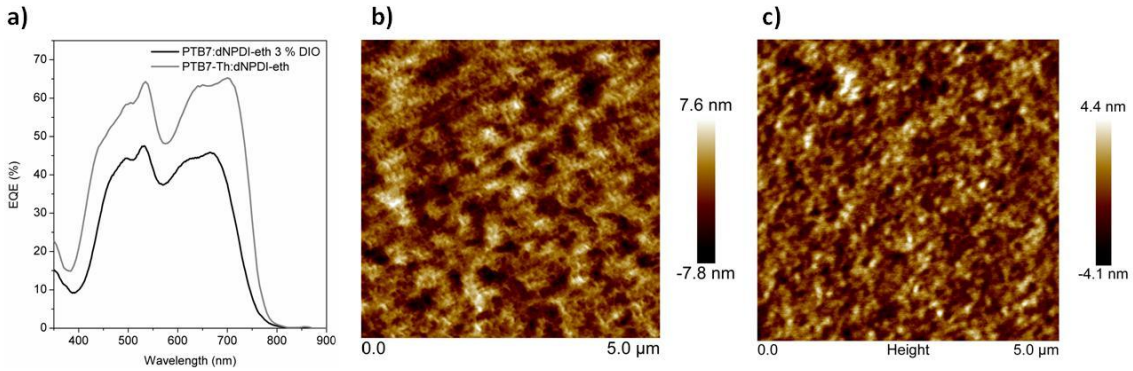

Figure 4.11. a) EQE spectra and AFM topography images of dNPDI-eth blends with b) PTB7 and c) PTB7-Th. AFM images are 5 µm x 5 µm. Vertical contrast bars show height variations in sample surfaces. Reprinted with permission from[128]. Copyright 2016 American Chemical Society.

4.2.2 Concluding Remarks

Linking two PDI monomers at the bay position creates a kink in the molecule, reducing π-π interactions between neighboring molecules and lowering crystallinity. Additionally, substituting the small molecule donor for polymers aides in producing uniform blend films with smaller domain sizes. However, donor selection is critical for achieving high performance. Ideally, several donor materials should be tested with each new acceptor to identify the best D/A pairing. But each additional donor expands the optimization landscape, increasing the number of devices that need to be fabricated. This can become cost prohibitive, since many commercially available donors retail for 1000-2000 $\$\cdot g^{-1}$, as they are not yet manufactured in large quantities.

4.3 Chapter 4 Summary

PDIs make good building blocks for acceptor molecules. However, the extended conjugated core results in large π-π interactions between PDI units, lowering solubility and enhancing crystallinity. To address this, creating twisted dimers seems to be the simplest method for reducing crystallinity. Additionally, using polymer donors instead of small molecule donors reduces the challenge of forming nanosized domains. Although among polymer donors there exist a long list of viable candidates, and the complex

interactions that take place during spin coating are not well understood, requiring a trial-and-error approach to device optimization.

CHAPTER 5 NANOEMBOSSED HETEROJUNCTIONS

The work presented in Chapters 3 and 4 highlight the challenges associated with optimizing the performance of non-fullerene acceptors. When research groups make new donor materials, the acceptor used is typically $PC_{61}BM$ or $PC_{71}BM$. As previously discussed in Chapter 1, fullerenes have good film-forming behavior and keeping the acceptor constant drastically reduces the amount of work required to optimize the chemical structures of the donors and the casting conditions. With non-fullerene acceptors, the donor material is usually unknown at the time the acceptor material is designed. There are several commercially-available donor polymers that routinely achieve greater than 7 % PCE when blended with fullerenes. These polymers typically cost 1000-2000 $\$\cdot g^{-1}$, and for a given acceptor molecule some will work well and some will not. Since most of these polymers have low bandgaps with panchromatic absorption across the visible spectrum, there is no a priori reason to choose one over another. However, testing several donors for each new acceptor can become cost and time prohibitive.

During the time period that this work took place (2012-2017), the solution-processed OPV field has experienced significant gains in performance. When blended with $PC_{71}BM$, small molecule donors achieve PCEs of 9 %,[130–133] and polymer donors achieve higher PCEs of 10-12 %.[21,134,135] The referenced donor materials are shown in Figure 5.1.

Additionally, non-fullerene acceptors have experienced significant increases in performance. When blended with polymer donors, PCEs of 9-12 % have recently been achieved.[136–138] With small molecule donors, the same issues with phase separation have been experienced by other research groups, and the best PCEs are only around 5 %.[139] The referenced donor and acceptor systems are shown in Figure 5.2.

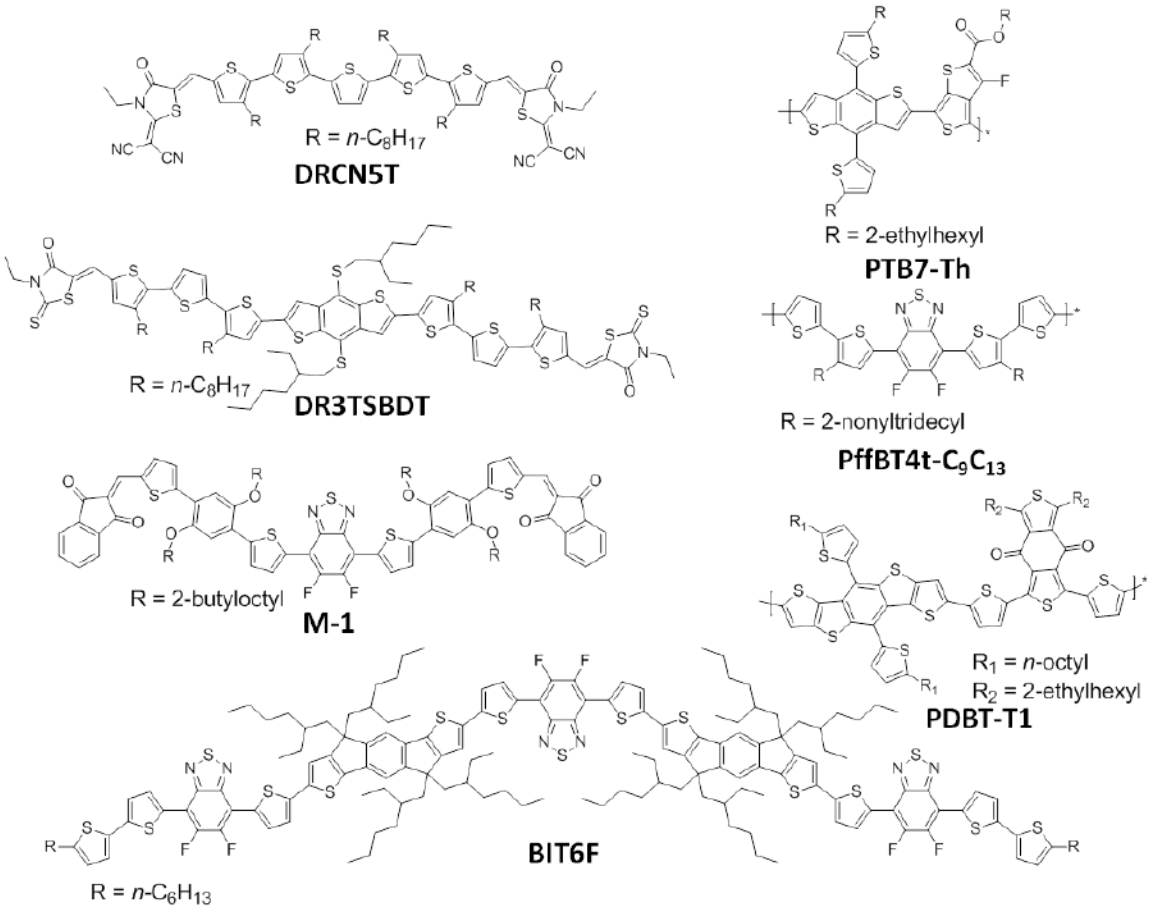

Figure 5.1. Recent high-performance donor materials achieving > 9 % PCE with $PC_{71}BM$.

As discussed in Chapter 2, the goal of chemical and film-casting optimization is to achieve a nanostructured film morphology such that every absorbed photon results in a harvested electron. Since organic synthesis is infinitely tunable, and casting conditions cover an immense parameter space, the best-performing donor:acceptor systems have resulted from brute-force engineering. This is reflected in both the structural evolution of donors and acceptors shown in Figure 5.1-5.2, as well as the highly tailored casting recipes found in experimental sections of journal articles. Unfortunately, these systems also tend to suffer from high sensitivity to chemical structure and processing conditions. Subtle modifications such as adding or removing a carbon atom, or changing the weight ratios of the dye solutions can result in dramatic reductions in PCE.

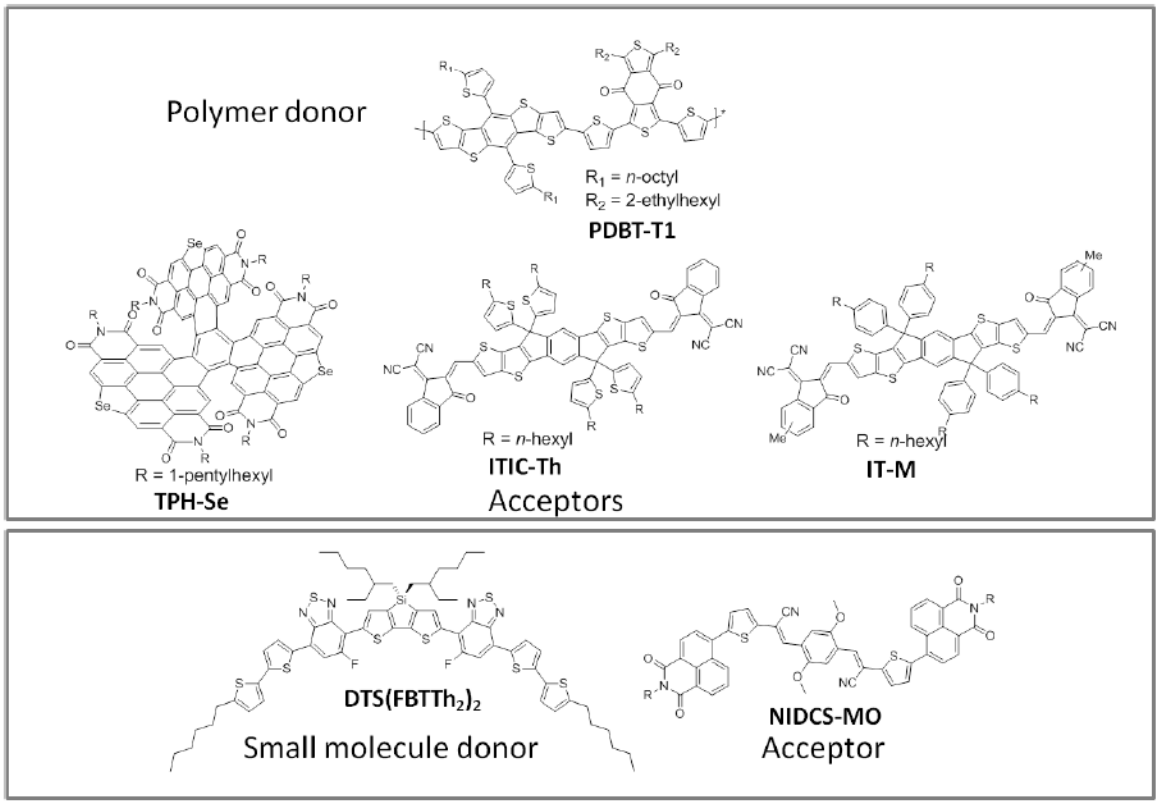

Figure 5.2. Recent high-performance donor non-fullerene acceptor systems.

The crux of these issues lies in the way the devices are made. Spin coating is an excellent technique for forming nanosized domains in blend films since the drying process is relatively fast. As the host solvent evaporates from a dye solution, the donor and acceptor materials come into closer proximity and experience stronger non-covalent interactions. Typically, the interspecies interactions lead to phase separation that can be characterized by some time constant, which is dependent on the materials and the casting conditions. There is also a time constant associated with the film drying. When the film dries on time scales shorter than phase-separation time scales, nanosized domains can be achieved. However, spin coating is not compatible with low-cost, high-throughput processing. To commercialize solution-processed OPVs a large-area technique such as slot-dye coating, gravure printing, or inkjet printing needs to be adopted. This completely changes the film drying kinetics, making it challenging to transplant a donor:acceptor system that has evolved on a spin coater to a vastly different casting environment. Research into roll-to-

roll solution-processed OPVs has largely been limited to P3HT:$PC_{61}BM$, achieving ~ 2 % PCE in large-area modules.[140] Although a more recent polymer:fullerene system, PBTZT-stat-BDTT-8:$PC_{61}BM$, has been identified to be able to achieve 4.5 % PCE in large-area modules. However, lab-scale devices routinely achieve greater than 9 % PCE, representing a 50 % decrease in efficiency upon up-scaling.[141,142]

Furthermore, the donor:acceptor BHJ can be thought of as having a kinetically-trapped morphology. If given excess thermal energy, such as by placing a device on a hot plate, phase separation can be driven to grow grain sizes which is often detrimental to device performance. When placed in the sun, solar cells experience internal temperatures of 50-75 °C.[143] Sustained elevated temperatures under these conditions can lead to decreased performance, with most high-performance blends experiencing half-lives on the order of hours. The stability of the metastable state of the BHJ is dependent on intermolecular interactions. π-π interactions between molecular planes or possible hydrogen bonding interactions can stabilize the morphology. Floppy solubilizing chains can create steric repulsion and increase distances between adjacent molecules, weakening intermolecular interactions. Furthermore, they can screen Coulombic potentials. Vibrational degrees of freedom can also soften potential barriers to molecular reorientation and diffusion. This is shown schematically in Figure 5.3. The rigid molecule on the left faces steep potential barriers in moving from metastable state 1 to state 2, while the floppy molecule on the right faces softer potentials barriers.

The issues associated with forming a nanoscale morphology with arbitrarily chosen donor and acceptor materials, and preventing that nanoscale morphology from relaxing over time, can both be addressed by decoupling film casting from the morphology. A technique known as nanoembossing has the potential to achieve this. Figure 5.4 shows a brief overview of the process. First, a neat layer of acceptor is deposited from solution onto a substrate. The deposition technique does not matter as long as a uniform film of desired thickness can be produced. Next, a nanostructured stamp is pressed into the film, patterning the acceptor film with either nanopillars or nanoindentations. In a roll-to-roll process this could be accomplished using a roller stamp. Finally, a neat donor solution is

deposited on top, filling the nanovoids created by the stamp. The last step requires that the donor solution does not dissolve the acceptor film.

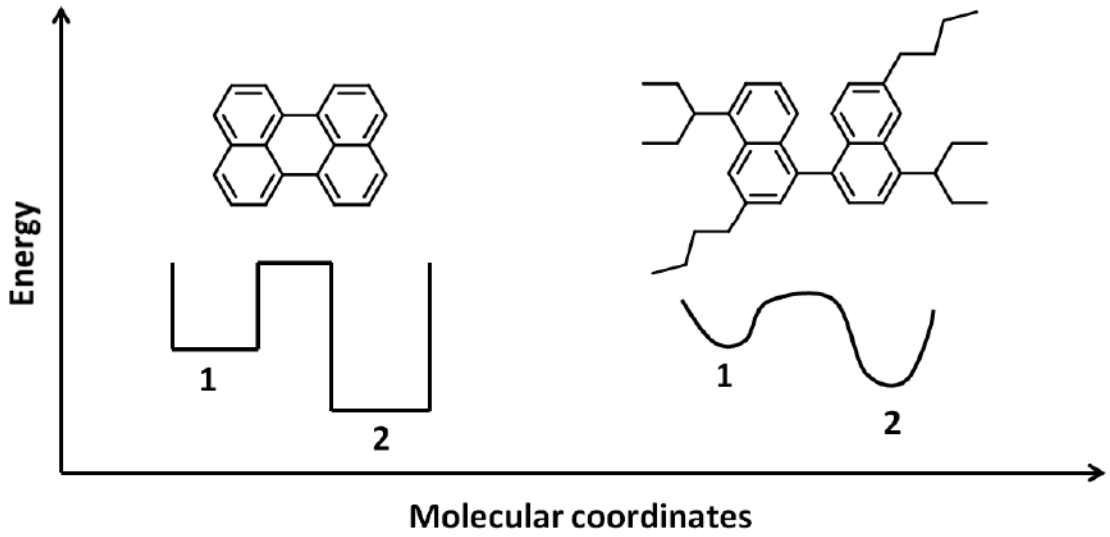

Figure 5.3. Potential energy barriers in transitioning between metastable states.

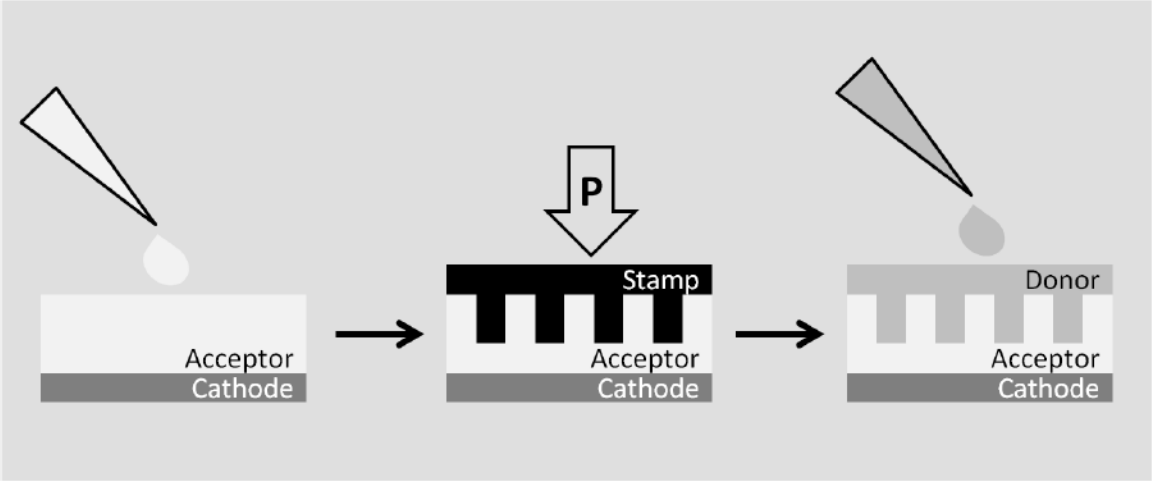

Figure 5.4. Nanoembossing OPV devices.

In principle, nanoembossing has the capability of imprinting a repeatable pattern into the acceptor film with optimal domain sizes. The lateral feature sizes of the stamp should be approximately twice the exciton diffusion length of the organic dyes, such that all

excitons can reach a donor/acceptor interface. The depth of the pattern should correspond to the film thickness, such that the imprinted features extend through the film. Since the requirement for spontaneous phase separation during film casting has been relaxed, the dyes used in this process can be more crystalline in nature. Using more rigid dyes with less solubilizing groups increases both the amount of electronically active material in the light absorbing layer, and the strength of π-π interactions between adjacent chromophores. In addition to enhanced electronic coupling, this also increases the electrostatic interactions between molecules, resulting in a more stable film. Further post-processing of the neat acceptor and donor layers can be done to further enhance the film stabilities. One method to accomplish this would be to use thermally cleavable solubilizing groups to form hydrogen bonds between adjacent molecules. This strategy is discussed later in this chapter. Another viable method to enhance film stability would be to crosslink adjacent molecules.

Nanoembossing, also known as nanoimprint lithography, is a technique used in the patterning of various polymer resists such as polymethylmethacrylate (PMMA) for subsequent pattern transfer to the underlying substrate.[144] Typically, nanostructured master stamps are made from silicon wafers that are patterned using electron beam lithography. Since the electron beam needs to raster over each feature, creating these stamps is a slow process and purchasing a stamp with features comparable to exciton diffusion lengths (~ 40 nm) costs more than $10,000 per cm^2. Despite the high cost, Yang *et al.* used this technique to create a grating in a donor polymer film (PCPDTBT) with 70 nm wide features. C_{70} was then evaporated onto the polymer grating using a rotating-planetary system, producing OPV devices with 5.5 % PCE.[145] Ideally an all-solution-processed method would be used, since introducing a vacuum deposition system into a roll-to-roll process significantly increases the cost. Furthermore, to evaporate molecules into high-aspect ratio indentations a rotating-planetary system is required to avoid shadow effects of the walls of the indentations. It is not obvious how such a mechanism could be implemented in a roll-to-roll process. Further development of this technique, using significantly cheaper stamps and solution processing of both acceptor and donor materials is described in this chapter.

5.1 Anodized Aluminum Oxide

When aluminum films or foils are anodized in various acid solutions under certain conditions, the resulting aluminum oxide can have uniform hexagonal arrays of nanosized pores that penetrate through the film or foil.[146] For a given acid solution, the pore size and interpore spacing varies linearly with anodizing potential. This has allowed researchers to create porous anodized aluminum oxide (AAO) templates with uniform pore sizes from 6 nm up to 600 nm, with anodizing potentials ranging from 6-250 V.[146–148] Figure 5.5 shows the dependence of the interpore spacing on the anodizing potential using a 10% H_2SO_4 solution. This low-cost, and facile method for creating nanostructured templates with tunable feature sizes is ideal for nanoembossing large-area arrays such OPV devices.

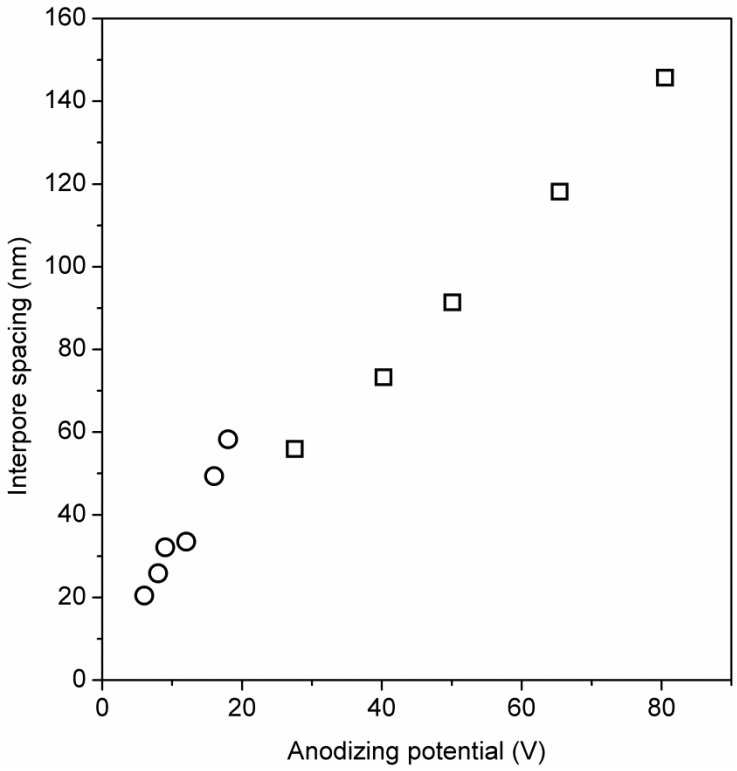

Figure 5.5. Interpore spacing of AAO templates versus anodizing potential using a 10% H_2SO_4 solution. Produced using data from[148,149]. The two marker symbols indicate the two referenced journal articles.

To create AAO templates that have low surface roughness compared to the thickness of the organic films, silicon wafers with 300.0 nm SiO_2 were used as substrates. The wafers were cut into squares approximately 25 mm x 25 mm. The wafer pieces were then placed under vacuum at a base pressure of 10^{-6} mbar. Next, 40 ± 1 nm of titanium was evaporated onto the wafers at a rate of 0.10 ± 0.05 nm·s^{-1}. The deposition rate of all evaporated materials was monitored using a quartz crystal microbalance deposition monitor. Since the conductive aluminum converts to insulating aluminum oxide during anodization, the titanium layer provides a conductive pathway for anodization to continue until all the aluminum has been converted. Previous researchers have shown that the anodization stops at the Ti/Al interface.[150] Finally, 100 ± 1 nm of aluminum was evaporated on the Ti layer at a rate of 0.10 ± 0.05 nm·s^{-1}. The Ti/Al coated wafer pieces were then placed in a 10% H_3PO_4 solution with one corner extending above the acid solution surface. This corner was used to make electrical contact with an alligator clip, and kept dry to avoid electrical shorts upon applying a bias. The beaker containing the solution was submerged in an ice bath to maintain the acid solution at 0 °C. A piece of stainless steel shim stock was used as a counter electrode, with one end extending above the surface of the acid solution for electrical contact via an alligator clip. Next, a 150 V bias was applied to the Ti/Al coated wafer piece, using a DC power supply with the negative terminal connected to the stainless steel counter electrode, The current supplied by the power supply was monitored, showing a current density of approximately 500 mA·cm^{-2} during anodization. After approximately 10 s the current density quickly decayed below 10 μA·cm^{-2}, and the anodization process was deemed complete. Figure 5.6 shows a scanning electron microscopy (SEM) image of an AAO template formed in 10% H_3PO_4 solution at 150 V, with pores approximately 100 nm in diameter. Ideally the pore diameter would be closer to 20-30 nm to correspond to twice the expected exciton diffusion length. However, larger pore sizes are easier to image.

The array of pores shown in Figure 5.6 is not well ordered. Very uniform, hexagonal arrays of pores can be realized by doing multiple anodization and etching steps.[146] However, this requires a much thicker initial aluminum layer and the uniform periodicity is not necessarily required for good performance in OPV devices.

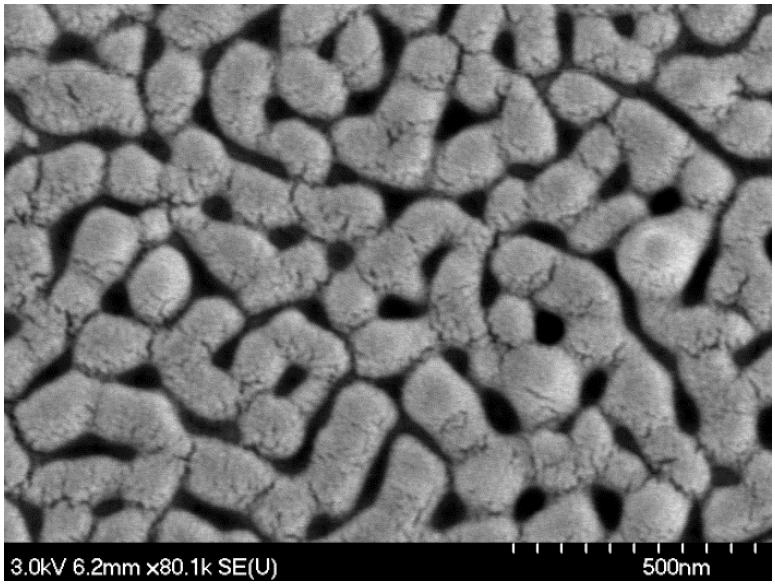

Figure 5.6. SEM image of AAO template formed at 150 V in 10 % H_3PO_4.

5.2 Embossing Acceptor Films

When polymer resists are nanoembossed, the polymer is usually heated to approximately 70 °C above its glass transition temperature, so that the polymer will flow between features when imprinted. Small molecules have very low glass transition temperatures, so the nanoembossing was done at room temperature. To reduce adhesion between the AAO template and the organic film, a self-assembled monolayer of perfluorohexanoic phosphonic acid was used to coat the AAO. To do this, the AAO templates were soaked overnight in a 1 mmol solution of perfluorohexanephosphonic acid in ethanol. After soaking, the AAO templates were rinsed in ethanol and blown dry with compressed air. Imprinting was done under 5.0 ± 0.1 MPa of pressure, supplied by a 100 mm diameter pneumatic cylinder, for 10 minutes. To ensure conformal contact of the AAO template to the substrate, a 3 mm thick piece of 25 mm x 25 mm fabric-reinforced silicone was placed between the piston rod of the cylinder and a 12 mm thick, 25 mm x 25 mm aluminum block that had been milled to be very flat (approximately 20 μm surface roughness). The fabric-reinforced silicone was chosen for its high compressive strength

and high melting point. The AAO template was placed face-down below the aluminum block and on top of the substrate to be patterned. The substrate to be patterned sat on top of a 12 mm thick, 80 mm x 80 mm aluminum block that had been milled to be very flat (approximately 20 µm surface roughness). The aluminum block had four feet to raise the block up such that a heating element could be attached to the bottom, forming a hotplate that could withstand large applied loads. The entire embossing apparatus was contained in an aluminum frame constructed from 80/20 modular framing. Figure 5.7 shows a schematic of this embossing process. The substrate to be patterned consisted of a clean piece of ITO-coated glass, with approximately 100 nm of dNPDI-eth spin cast on top. The dNPDI-eth was deposited from a 20 $mg \cdot mL^{-1}$ solution in chlorobenzene, spun at 1000 rpm for 60 s.

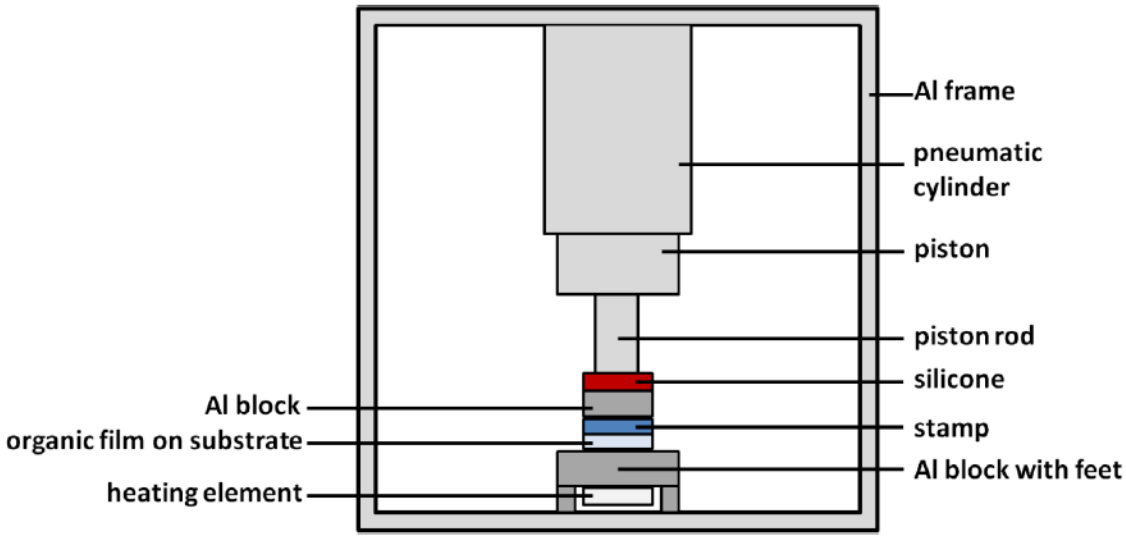

Figure 5.7. Schematic of the nanoembossing procedure.

Figure 5.8 shows SEM micrographs of an AAO template before and after being used to directly emboss a dNPDI-eth film. The arrows point to regions where the acceptor molecules have become stuck in the AAO pores, creating pock marks on the acceptor film.

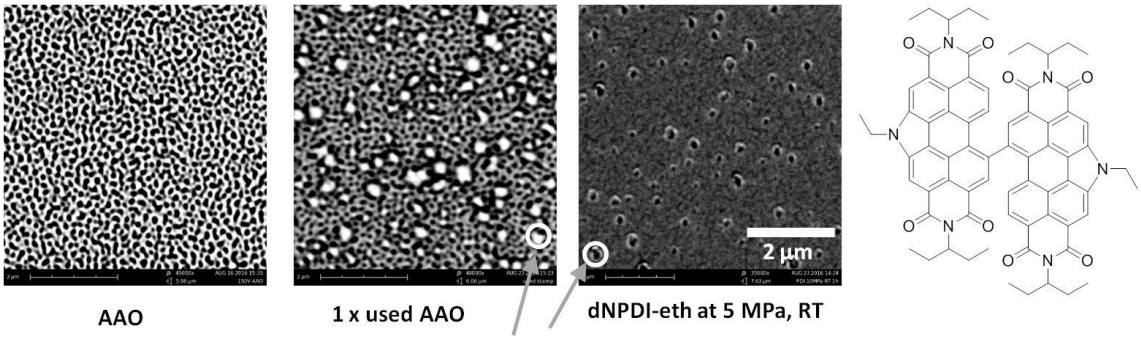

Figure 5.8. SEM micrograph of a fresh and used AAO template, and the dNPDI-eth embossed film. Chemical structure of dNPDI-eth shown at far right.

Since small molecule films are not very mechanically robust, it was rationalized that using an AAO template directly would create nanopillars that could easily break and detach from the film. Inverting the pattern should be easier since poking holes in a film does not create fragile structures. To address this, an inverted stamp was made by first embossing a PMMA film, one of the most widely studied materials for nanoembossing.[146] The inverted stamp was made on 25 mm x 25 mm pieces of Si wafer with 300.0 nm of SiO_2. Hexamethyldisilazane (HMDS) (MCC Primer 80:20, Microchem) was spin cast on top of the Si wafers at 4000 rpm for 60 s, then annealed on a hotplate at 110 ± 2 °C for 3 minutes, as per manufacturer instructions. The HMDS promotes adhesion of the PMMA to the wafer. Next, a 50 $mg \cdot mL^{-1}$ solution of 80:20 15 kDa:1 MDa PMMA in chlorobenzene was spin-cast onto the HMDS-treated Si wafers 1000 rpm for 60 s. The high molecular weight PMMA aides in uniform film forming, while the low molecular weight is required to form nanostructures since the smallest feature size attainable is proportional to the radius of gyration of the embossed polymer.[144] Using the same embossing configuration as in Figure 5.7, the PMMA films were heated to 185 ± 2 °C under approximately 500 kPa so that the AAO template would be at the same temperature, before the pressure was increased to 5.0 ± 0.1 MPa for 10 minutes. The hotplate was allowed to cool below 70 °C before the pressure was relieved and the stamp delaminated. The nanostructured PMMA films were then used to emboss dNPDI-eth films at 5.0 ± 0.1 MPa at room temperature for 10 minutes. Figure 5.8 shows SEM micrographs of the three substrates.

The protruding features (lighter color) in the PMMA film have length scales that correspond to the pores in the AAO template. The dNPDI-eth film has indentations that correspond to the protrusions from the PMMA film. This confirms that this is a viable method for producing nanostructured small-molecule acceptor films.

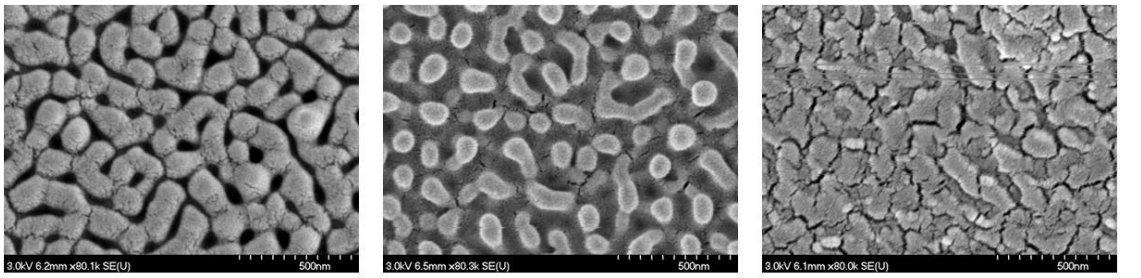

Figure 5.8. SEM micrographs of AAO template with approximately 100 nm diameter pores, embossed PMMA film with protruding structures corresponding to the AAO pores, and embossed dNPDI-eth film with indentations corresponding to the PMMA protrusions.

5.3 Orthogonal Donor Films

With a nanostructured acceptor film, the remaining criterion for this technique to succeed is that the donor solution cannot dissolve the acceptor film. In other words, the donor solution needs to be orthogonal to the acceptor film. There are two strategies that could be employed to achieve this: 1) the donor could be chemically altered to be soluble in orthogonal solvents such as alcohol or water; 2) the acceptor film could be post-processed to be insoluble in organic solvents. Since remaking donor materials is outside the scope of this project, the second option was chosen. From this route, there are two obvious techniques that could be used: thermally-cleavable solubilizing groups, or UV-crosslinking of acceptor molecules. Figure 5.9 shows the option with thermally cleavable solubilizing groups, which was determined to be easier to implement. Essentially the annulated nitrogen atom of the acceptor would have a *t*-butyloxycarbonyl protecting group, allowing the acceptor to be soluble in common organic solvents. After film deposition and nanostructuring, annealing the films at 180 °C should thermally cleave the ester group, producing hydrogen-terminated annulated nitrogens and evolving CO_2 and

isobutylene gas.[152] The hydrogen-terminated nitrogens should be able to hydrogen bond with neighboring molecules, rendering the film insoluble in organic solvents used to deposit the donor material.

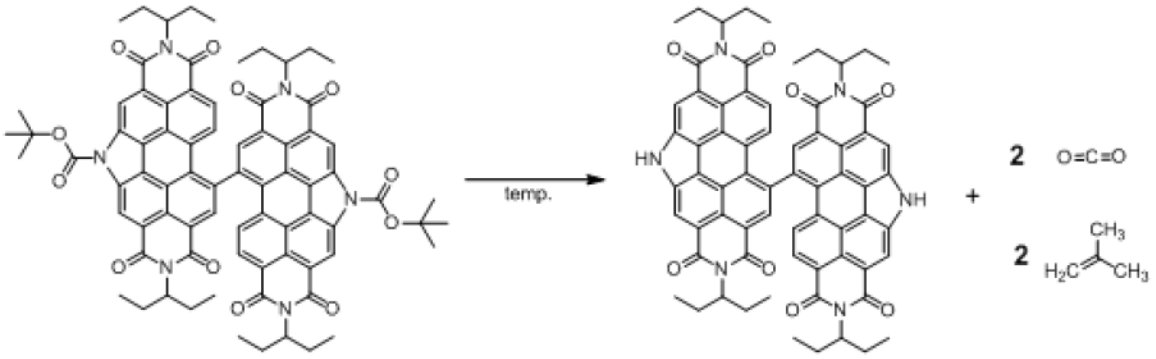

Figure 5.9. Thermal deprotection of *t*-butyloxycarbonyl from dNPDI acceptors.

5.4 Chapter 5 Summary

Our collaborators have yet to scale-up the synthesis of the acceptor shown in Figure 5.9. However, the concept of nanoembossing small-molecule acceptor films has been has been shown to be a viable method for achieving reproducible nanoscale morphology of organic thin films, independent of the method of deposition. Furthermore, this technique can be compatible with low-cost, continuous fabrication procedures if implemented in the form of a roller stamp, for example. Using AAO templates provides an extremely low-cost method for producing nanostructured stamps. Furthermore, this morphology is independent of the donor and acceptor pairing, such that any two materials should be able to be combined in an OPV device where the performance is not limited by morphology. Additionally, the thermally cleavable solubilizing chains introduce hydrogen bonds between adjacent molecules, which are expected to significantly increase the thermal stability of the devices.

CHAPTER 6 CONCLUSION

At the beginning of this project (2012), solution-processed OPVs had begun to achieve PCEs of ~ 7 % when blended with fullerene acceptors. Around this time researchers became interested in non-fullerene acceptors to address the shortcomings of fullerenes. The work presented in Chapters 3 and 4 details the progression of designing and integrating non-fullerene acceptors into solution-processed OPV devices.

As a starting point, a push-pull chromophore strategy was used to design acceptor molecules with electron-deficient building blocks to increase the HOMO and LUMO binding energies. Phthalimide and naphthalimide groups served as the electron-deficient end-groups, connected to a DPP core through electron-rich thiophene units. Using UPS, the ionization energies of this series of molecules were measured to range between 5.2-5.4 eV, sufficiently large for transfer of a photoexcited hole from the acceptor to a wide range of donor molecules. This series of compounds was intended to be used in BHJ devices, however the use of long alkyl chains did not result in sufficiently soluble dyes, prohibiting the casting of BHJ films. To understand the electron transport capabilities, n-channel TFTs were fabricated. The best performing molecule achieved electron mobilities on the order of 10^{-3} $cm^2 \cdot V^{-1} \cdot s^{-1}$, an order of magnitude lower than the mobilities of fullerenes in similar TFT devices.

In the following iteration of molecules, the DPP core was removed and molecules consisting only of phthalimide and thiophene were investigated. Larger ionization energies ranging from 5.7-6.5 eV were measured via UPS, which could be correlated to the relative amounts of electron-deficient to electron-rich building blocks. The electron mobilities in TFT devices reached 10^{-1} $cm^2 \cdot V^{-1} \cdot s^{-1}$ for the best performing molecules in this series, sufficiently large for high-performance OPV devices. Furan substitution for the thiophene units was also investigated, however the furan-containing compound was found to exhibit no measurable electron mobility. A higher hole mobility was achieved by the furan-containing compound, indicating furan for thiophene substitution may be

more appropriate in donor molecules. However, since the exact mechanism of the differences in mobilities has yet to be determined, this idea remains a conjecture.

Moving forward, the phthalimide-thiophene architecture was further modified to incorporate branched ethylpropyl solubilizing groups, significantly increasing the solubilities. A number of core substitutions were investigated, significantly altering the optical absorption properties and tuning the ionization energies between 5.4-6.1 eV. With sufficiently soluble acceptors, BHJ devices were fabricated using both a small-molecule and a polymer donor. The most promising molecule used isoindigo as the central core, resulting in PCEs of 0.4 % when blended with the small-molecule donor DTS($FBTTh_2$)$_2$. However, the morphologies of the blend films, determined using AFM, indicated that large domain sizes were limiting the number of excitons that could reach a donor/acceptor interface. In a series of separate studies, the isoindigo-containing molecule was structurally modified by Seth McAfee, while Jessica Topple optimized the performance with DTS($FBTTh_2$)$_2$, achieving PCEs of 2 %.

While modest performance improvements were made with the phthalimide/naphthalimide and thiophene molecular architecture, continuing issues with large domain sizes provided the motivation to try an alternative strategy. PDI monomers, which are rigid-extended chromophores and had been widely studied in both TFT and OPV devices, were chosen to be the basis of the next series of molecules. Branched alkyl chain substitutions were made to the imide nitrogen location. The length and branching point of the alkyl chains were found to have significant impacts on the solubilities and film-forming properties. In BHJ devices with DTS($FBTTh_2$)$_2$, PCEs of 3.2 % were achieved using ethylpropyl chains, however macroscopic film uniformity remained an issue for the best performing acceptor. Furthermore, donor and acceptor domain sizes were still found to be limiting device performance.

To address the phase separation issue, a dimer was constructed by bay-linking two PDI monomers to reduce crystallinity of the acceptor. Polymer donors were also used since they tend to be less sensitive to casting conditions and form uniform films with smaller

domain sizes. PCEs of 5.5 % were achieved when blending the dimer with PTB7-Th, a significant improvement over the PDI monomer devices with a small-molecule donor.

However, donor selection among polymers still presented itself to be an important criterion. The morphology of organic films that result from a dynamic process such as spin coating depends on a large list of complex interactions between donor and acceptor dyes, solvents, solvent additives, and the surrounding working gas. Furthermore, achieving an intimately-mixed metastable morphology can lead to shorter lifetimes when the morphology can easily relax to a more stable state.

To address the challenges associated with fabricating and maintaining nanosized domains, nanoembossing was investigated to form nanostructured acceptor films that could be post-processed to enhance thermal stability. Aluminum films were anodized to form nanoporous AAO templates for embossing acceptor films. Direct pattern transfer to the acceptor was found to be problematic, since the acceptor molecules tended to stick inside the pores of the AAO. An inverted stamp was then fabricated by embossing a PMMA film with the AAO template, forming a nanopillared stamp. This stamp was then used to emboss the acceptor film at room temperature, forming nanoindentations in the acceptor with feature sizes that could be traced back to the pores in the AAO template. This study confirmed that AAO provides a low-cost method for producing nanostructured stamps for embossing small-molecule acceptor films. If mounted on a roller, this technique could be compatible with roll-to-roll processing of OPV devices.

To address the issues of both thermal stability and orthogonality of the donor solution, a dimer molecule with thermally-cleavable solubilizing chains was proposed. Cleaving the solubilizing chains leaves behind NH groups that can undergo hydrogen bonding with adjacent molecules to enhance the thermal stability and reduce the solubility of the acceptor film. However, this molecule has yet to be synthesized in quantities required to be integrated into devices.

Future work on this project should focus on integrating the aforementioned dimer molecule to create nanoindented acceptor films. The aspect ratios of the indentations should be optimized to allow for films with sufficient optical densities for absorbing incident light, yet maintaining short distances for excitons to travel before reaching a D/A interface. The pore sizes of the AAO templates initially studied were approximately 100 nm in diameter. This pore diameter should be reduced to approximately 20-30 nm for efficient exciton harvesting. The solubilizing chains should be able to be cleaved without changing the structure of the acceptor film. Since organic films are known to undergo grain growth during annealing, it may be necessary for the stamp to be in place while the cleaving process occurs. Unfortunately, PMMA is typically embossed at the cleaving temperature (180 °C) and will likely be too soft to maintain structural rigidity while under heat and pressure. To address this, either a nanopillared SiO_2 stamp could be made by using a free-standing AAO template as a shadow mask for metal deposition onto the SiO_2, followed by reactive ion etching, or a spin-on dielectric such as polyamic acid could be used to pore-fill the AAO template followed by curing at 350 °C. This will result in a nanopillared polyimide film with much higher thermal stability than PMMA, that can removed from the AAO template by etching in warm H_3PO_4.

Following the production of a high aspect ratio nanoindented acceptor film, that is insoluble in common organic solvents, donor materials should be investigated for optimizing performance. Polymer donors will no longer be needed for their film-forming characteristics, and are substantially more expensive than synthesizing simple small-molecule donors. Since nanosized domain formation will no longer be an issue, optimizing chemical structures to investigate molecular orientation at the D/A interface for enhancing charge separation will likely produce the most significant performance gains. Additionally, developing dyes with longer exciton and charge-carrier diffusion lengths will improve performance and relax constraints on domain sizes.

BIBLIOGRAPHY

[1] J. Appleby, The Relentless Revolution, Reprint edition, WW Norton, 2011.

[2] A. Smith, Wealth of Nations, Hayes Barton Press, 1970.

[3] M. Beaud, A History of Capitalism 1500-2000, Aakar Books, 2006.

[4] J.R. Fleming, Joseph Fourier, the "greenhouse effect", and the quest for a universal theory of terrestrial temperatures, Endeavour. 23 (1999) 72–75. doi:10.1016/S0160-9327(99)01210-7.

[5] J. Hansen, M. Sato, R. Ruedy, K. Lo, D.W. Lea, M. Medina-Elizade, Global temperature change, Proc. Natl. Acad. Sci. 103 (2006) 14288–14293. doi:10.1073/pnas.0606291103.

[6] M. Vermeer, S. Rahmstorf, Global sea level linked to global temperature, Proc. Natl. Acad. Sci. 106 (2009) 21527–21532. doi:10.1073/pnas.0907765106.

[7] M.A. Bender, T.R. Knutson, R.E. Tuleya, J.J. Sirutis, G.A. Vecchi, S.T. Garner, I.M. Held, Modeled Impact of Anthropogenic Warming on the Frequency of Intense Atlantic Hurricanes, Science. 327 (2010) 454–458. doi:10.1126/science.1180568.

[8] D. Coumou, S. Rahmstorf, A decade of weather extremes, Nat. Clim. Change. 2 (2012) 491–496. doi:10.1038/nclimate1452.

[9] S. Ghosh, S. Rahman, Global deployment of solar photovoltaics: Its opportunities and challenges, in: 2016 IEEE PES Innov. Smart Grid Technol. Conf. Eur. ISGT-Eur., 2016: pp. 1–6. doi:10.1109/ISGTEurope.2016.7856217.

[10] V. Smil, Energy Transitions: History, Requirements, Prospects, Praeger, Santa Barbara, Calif, 2010.

[11] World Population Prospects - Population Division - United Nations, (2017). https://esa.un.org/unpd/wpp/ (accessed April 4, 2017).

[12] H. Friedli, H. Lötscher, H. Oeschger, U. Siegenthaler, B. Stauffer, Ice core record of the 13C/12C ratio of atmospheric CO2 in the past two centuries, Nature. 324 (1986) 237–238. doi:10.1038/324237a0.

[13] NOAA, ESRL Global Monitoring Division - Global Greenhouse Gas Reference Network, (2017). https://www.esrl.noaa.gov/gmd/ccgg/trends/full.html (accessed April 4, 2017).

[14] D. Lüthi, M. Le Floch, B. Bereiter, T. Blunier, J.-M. Barnola, U. Siegenthaler, D. Raynaud, J. Jouzel, H. Fischer, K. Kawamura, T.F. Stocker, High-resolution carbon dioxide concentration record 650,000–800,000 years before present, Nature. 453 (2008) 379–382. doi:10.1038/nature06949.

[15] National Renewable Energy Laboratory (NREL) Home Page, (2017). http://www.nrel.gov/ (accessed May 30, 2017).

[16] G.J. Bauhuis, P. Mulder, E.J. Haverkamp, J.C.C.M. Huijben, J.J. Schermer, 26.1% thin-film GaAs solar cell using epitaxial lift-off, Sol. Energy Mater. Sol. Cells. 93 (2009) 1488–1491. doi:10.1016/j.solmat.2009.03.027.

[17] K. Lee, J. Lee, B.A. Mazor, S.R. Forrest, Transforming the cost of solar-to-electrical energy conversion: Integrating thin-film GaAs solar cells with non-tracking mini-concentrators, Light Sci. Appl. 4 (2015) e288. doi:10.1038/lsa.2015.61.

[18] M.A. Green, Commercial progress and challenges for photovoltaics, Nat. Energy. 1 (2016) nenergy201515. doi:10.1038/nenergy.2015.15.

[19] A. Gürses, M. Açıkyıldız, K. Güneş, M.S. Gürses, Dyes and Pigments: Their Structure and Properties, in: Dyes Pigments, Springer International Publishing, 2016: pp. 13–29. doi:10.1007/978-3-319-33892-7_2.

[20] W. Cao, J. Xue, Recent progress in organic photovoltaics: device architecture and optical design, Energy Environ. Sci. 7 (2014) 2123–2144. doi:10.1039/C4EE00260A.

[21] J. Zhao, Y. Li, G. Yang, K. Jiang, H. Lin, H. Ade, W. Ma, H. Yan, Efficient organic solar cells processed from hydrocarbon solvents, Nat. Energy. 1 (2016) 15027. doi:10.1038/nenergy.2015.27.

[22] V. Coropceanu, J. Cornil, D.A. da Silva Filho, Y. Olivier, R. Silbey, J.-L. Brédas, Charge Transport in Organic Semiconductors, Chem. Rev. 107 (2007) 926–952. doi:10.1021/cr050140x.

[23] Y. Diao, K.M. Lenn, W.-Y. Lee, M.A. Blood-Forsythe, J. Xu, Y. Mao, Y. Kim, J.A. Reinspach, S. Park, A. Aspuru-Guzik, G. Xue, P. Clancy, Z. Bao, S.C.B. Mannsfeld, Understanding Polymorphism in Organic Semiconductor Thin Films through Nanoconfinement, J. Am. Chem. Soc. 136 (2014) 17046–17057. doi:10.1021/ja507179d.

[24] A. Byk, H. Borck, Ber. dtsch. physik, Ber Deut Phys. Ges. 8 (1910) 621.

[25] I.G. Hill, A. Kahn, Z.G. Soos, J. Pascal R.A., Charge-separation energy in films of π-conjugated organic molecules, Chem. Phys. Lett. 327 (2000) 181–188. doi:10.1016/S0009-2614(00)00882-4.

[26] C.W. Tang, Two-layer organic photovoltaic cell, Appl. Phys. Lett. 48 (1986) 183–185. doi:10.1063/1.96937.

[27] M. Muntwiler, Q. Yang, W.A. Tisdale, X.-Y. Zhu, Coulomb Barrier for Charge Separation at an Organic Semiconductor Interface, Phys. Rev. Lett. 101 (2008) 196403. doi:10.1103/PhysRevLett.101.196403.

[28] S. Gélinas, A. Rao, A. Kumar, S.L. Smith, A.W. Chin, J. Clark, T.S. van der Poll, G.C. Bazan, R.H. Friend, Ultrafast Long-Range Charge Separation in Organic Semiconductor Photovoltaic Diodes, Science. 343 (2014) 512–516. doi:10.1126/science.1246249.

[29] J. Lee, K. Vandewal, S.R. Yost, M.E. Bahlke, L. Goris, M.A. Baldo, J.V. Manca, T.V. Voorhis, Charge Transfer State Versus Hot Exciton Dissociation in Polymer−Fullerene Blended Solar Cells, J. Am. Chem. Soc. 132 (2010) 11878–11880. doi:10.1021/ja1045742.

[30] K. Vandewal, S. Albrecht, E.T. Hoke, K.R. Graham, J. Widmer, J.D. Douglas, M. Schubert, W.R. Mateker, J.T. Bloking, G.F. Burkhard, A. Sellinger, J.M.J. Fréchet, A. Amassian, M.K. Riede, M.D. McGehee, D. Neher, A. Salleo, Efficient charge generation by relaxed charge-transfer states at organic interfaces, Nat. Mater. 13 (2014) 63–68. doi:10.1038/nmat3807.

[31] B. Bernardo, D. Cheyns, B. Verreet, R.D. Schaller, B.P. Rand, N.C. Giebink, Delocalization and dielectric screening of charge transfer states in organic photovoltaic cells, Nat. Commun. 5 (2014) 3245. doi:10.1038/ncomms4245.

[32] K.J. Bergemann, S.R. Forrest, Measurement of exciton diffusion lengths in optically thin organic films, Appl. Phys. Lett. (2011). doi:10.1063/1.3668106.

[33] J.D.A. Lin, O.V. Mikhnenko, J. Chen, Z. Masri, A. Ruseckas, A. Mikhailovsky, R.P. Raab, J. Liu, P.W.M. Blom, M.A. Loi, C.J. García-Cervera, I.D.W. Samuel, T.-Q. Nguyen, Systematic study of exciton diffusion length in organic semiconductors by six experimental methods, Mater. Horiz. 1 (2014) 280. doi:10.1039/c3mh00089c.

[34] R.R. Lunt, J.B. Benziger, S.R. Forrest, Relationship between Crystalline Order and Exciton Diffusion Length in Molecular Organic Semiconductors, Adv. Mater. 22 (2010) 1233–1236. doi:10.1002/adma.200902827.

[35] Y. Zhou, T. Taima, T. Miyadera, T. Yamanari, M. Kitamura, K. Nakatsu, Y. Yoshida, Phase separation of co-evaporated ZnPc:C_{60} blend film for highly efficient organic photovoltaics, Appl. Phys. Lett. 100 (2012) 233302. doi:10.1063/1.4726118.

[36] K. Cnops, B.P. Rand, D. Cheyns, B. Verreet, M.A. Empl, P. Heremans, 8.4% efficient fullerene-free organic solar cells exploiting long-range exciton energy transfer, Nat. Commun. 5 (2014) 3406. doi:10.1038/ncomms4406.

[37] W. Ma, C. Yang, X. Gong, K. Lee, A.J. Heeger, Thermally Stable, Efficient Polymer Solar Cells with Nanoscale Control of the Interpenetrating Network Morphology, Adv. Funct. Mater. 15 (2005) 1617–1622. doi:10.1002/adfm.200500211.

[38] Y. Liang, D. Feng, Y. Wu, S.-T. Tsai, G. Li, C. Ray, L. Yu, Highly Efficient Solar Cell Polymers Developed via Fine-Tuning of Structural and Electronic Properties, J. Am. Chem. Soc. 131 (2009) 7792–7799. doi:10.1021/ja901545q.

[39] T.-Y. Chu, J. Lu, S. Beaupré, Y. Zhang, J.-R. Pouliot, S. Wakim, J. Zhou, M. Leclerc, Z. Li, J. Ding, Y. Tao, Bulk Heterojunction Solar Cells Using Thieno[3,4-c]pyrrole-4,6-dione and Dithieno[3,2-b:2′,3′-d]silole Copolymer with a Power Conversion Efficiency of 7.3%, J. Am. Chem. Soc. 133 (2011) 4250–4253. doi:10.1021/ja200314m.

[40] T.S. van der Poll, J.A. Love, T.-Q. Nguyen, G.C. Bazan, Non-Basic High-Performance Molecules for Solution-Processed Organic Solar Cells, Adv. Mater. 24 (2012) 3646–3649. doi:10.1002/adma.201201127.

[41] N.C. Miller, E. Cho, R. Gysel, C. Risko, V. Coropceanu, C.E. Miller, S. Sweetnam, A. Sellinger, M. Heeney, I. McCulloch, J.-L. Brédas, M.F. Toney, M.D. McGehee, Factors Governing Intercalation of Fullerenes and Other Small Molecules Between the Side Chains of Semiconducting Polymers Used in Solar Cells, Adv. Energy Mater. 2 (2012) 1208–1217. doi:10.1002/aenm.201200392.

[42] A. Anctil, C.W. Babbitt, R.P. Raffaelle, B.J. Landi, Material and Energy Intensity of Fullerene Production, Environ. Sci. Technol. 45 (2011) 2353–2359. doi:10.1021/es103860a.

[43] A. Anctil, C.W. Babbitt, R.P. Raffaelle, B.J. Landi, Cumulative energy demand for small molecule and polymer photovoltaics, Prog. Photovolt. Res. Appl. 21 (2013) 1541–1554. doi:10.1002/pip.2226.

[44] M. Mojica, J.A. Alonso, F. Méndez, Synthesis of fullerenes, J. Phys. Org. Chem. 26 (2013) 526–539. doi:10.1002/poc.3121.

[45] G. Ren, E. Ahmed, S.A. Jenekhe, Non-Fullerene Acceptor-Based Bulk Heterojunction Polymer Solar Cells: Engineering the Nanomorphology via Processing Additives, Adv. Energy Mater. 1 (2011) 946–953. doi:10.1002/aenm.201100285.

[46] J.T. Bloking, X. Han, A.T. Higgs, J.P. Kastrop, L. Pandey, J.E. Norton, C. Risko, C.E. Chen, J.-L. Brédas, M.D. McGehee, A. Sellinger, Solution-Processed Organic Solar Cells with Power Conversion Efficiencies of 2.5% using Benzothiadiazole/Imide-Based Acceptors, Chem. Mater. 23 (2011) 5484–5490. doi:10.1021/cm203111k.

[47] Y. Zhou, L. Ding, K. Shi, Y.-Z. Dai, N. Ai, J. Wang, J. Pei, A Non-Fullerene Small Molecule as Efficient Electron Acceptor in Organic Bulk Heterojunction Solar Cells, Adv. Mater. 24 (2012) 957–961. doi:10.1002/adma.201103927.

[48] B. Walker, X. Han, C. Kim, A. Sellinger, T.-Q. Nguyen, Solution-Processed Organic Solar Cells from Dye Molecules: An Investigation of Diketopyrrolopyrrole:Vinazene Heterojunctions, ACS Appl. Mater. Interfaces. 4 (2012) 244–250. doi:10.1021/am201304e.

[49] S. Rajaram, R. Shivanna, S.K. Kandappa, K.S. Narayan, Nonplanar Perylene Diimides as Potential Alternatives to Fullerenes in Organic Solar Cells, J. Phys. Chem. Lett. 3 (2012) 2405–2408. doi:10.1021/jz301047d.

[50] A.G. Ismail, I.G. Hill, Stability of n-channel organic thin-film transistors using oxide, SAM-modified oxide and polymeric gate dielectrics, Org. Electron. 12 (2011) 1033–1042. doi:10.1016/j.orgel.2011.03.027.

[51] J. Huang, P.F. Miller, J.C. de Mello, A.J. de Mello, D.D.C. Bradley, Influence of thermal treatment on the conductivity and morphology of PEDOT/PSS films, Synth. Met. 139 (2003) 569–572. doi:10.1016/S0379-6779(03)00280-7.

[52] Y. Sun, J.H. Seo, C.J. Takacs, J. Seifter, A.J. Heeger, Inverted Polymer Solar Cells Integrated with a Low-Temperature-Annealed Sol-Gel-Derived ZnO Film as an Electron Transport Layer, Adv. Mater. 23 (2011) 1679–1683. doi:10.1002/adma.201004301.

[53] L. Znaidi, Sol–gel-deposited ZnO thin films: A review, Mater. Sci. Eng. B. 174 (2010) 18–30. doi:10.1016/j.mseb.2010.07.001.

[54] Z.-G. Zhang, B. Qi, Z. Jin, D. Chi, Z. Qi, Y. Li, J. Wang, Perylene diimides: a thickness-insensitive cathode interlayer for high performance polymer solar cells, Energy Environ. Sci. 7 (2014) 1966. doi:10.1039/c4ee00022f.

[55] L. Chang, I.E. Jacobs, M.P. Augustine, A.J. Moulé, Correlating dilute solvent interactions to morphology and OPV device performance, Org. Electron. 14 (2013) 2431–2443. doi:10.1016/j.orgel.2013.06.016.

[56] B.W. D'Andrade, S. Datta, S.R. Forrest, P. Djurovich, E. Polikarpov, M.E. Thompson, Relationship between the ionization and oxidation potentials of molecular organic semiconductors, Org. Electron. 6 (2005) 11–20. doi:10.1016/j.orgel.2005.01.002.

[57] P. Hohenberg, W. Kohn, Inhomogeneous Electron Gas, Phys. Rev. 136 (1964) B864–B871. doi:10.1103/PhysRev.136.B864.

[58] A.D. Becke, Density-functional exchange-energy approximation with correct asymptotic behavior, Phys. Rev. A. 38 (1988) 3098–3100. doi:10.1103/PhysRevA.38.3098.

[59] A.D. Becke, A new mixing of Hartree–Fock and local density-functional theories, J. Chem. Phys. 98 (1993) 1372–1377. doi:10.1063/1.464304.

[60] C. Lee, W. Yang, R.G. Parr, Development of the Colle-Salvetti correlation-energy formula into a functional of the electron density, Phys. Rev. B. 37 (1988) 785–789. doi:10.1103/PhysRevB.37.785.

[61] D.G. Farnum, G. Mehta, G.G.I. Moore, F.P. Siegal, Attempted reformatskii reaction of benzonitrile, 1,4-diketo-3,6-diphenylpyrrolo[3,4-C]pyrrole. A lactam analogue of pentalene., Tetrahedron Lett. 15 (1974) 2549–2552. doi:10.1016/S0040-4039(01)93202-2.

[62] D. Chandran, K.-S. Lee, Diketopyrrolopyrrole: A versatile building block for organic photovoltaic materials, Macromol. Res. 21 (2013) 272–283. doi:10.1007/s13233-013-1141-3.

[63] C.B. Nielsen, M. Turbiez, I. McCulloch, Recent Advances in the Development of Semiconducting DPP-Containing Polymers for Transistor Applications, Adv. Mater. 25 (2013) 1859–1880. doi:10.1002/adma.201201795.

[64] S. Qu, H. Tian, Diketopyrrolopyrrole (DPP)-based materials for organic photovoltaics, Chem. Commun. 48 (2012) 3039–3051. doi:10.1039/C2CC17886A.

[65] P. Sonar, G.-M. Ng, T.T. Lin, A. Dodabalapur, Z.-K. Chen, Solution processable low bandgap diketopyrrolopyrrole (DPP) based derivatives: novel acceptors for organic solar cells, J. Mater. Chem. 20 (2010) 3626–3636. doi:10.1039/B924404B.

[66] Y. Lin, P. Cheng, Y. Li, X. Zhan, A 3D star-shaped non-fullerene acceptor for solution-processed organic solar cells with a high open-circuit voltage of 1.18 V, Chem. Commun. 48 (2012) 4773. doi:10.1039/c2cc31511d.

[67] Y. Lin, Y. Li, X. Zhan, A Solution-Processable Electron Acceptor Based on Dibenzosilole and Diketopyrrolopyrrole for Organic Solar Cells, Adv. Energy Mater. 3 (2013) 724–728. doi:10.1002/aenm.201200911.

[68] A.D. Hendsbee, J.-P. Sun, L.R. Rutledge, I.G. Hill, G.C. Welch, Electron deficient diketopyrrolopyrrole dyes for organic electronics: synthesis by direct arylation, optoelectronic characterization, and charge carrier mobility, J. Mater. Chem. A. 2 (2014) 4198. doi:10.1039/c3ta14414c.

[69] J.-L. Bredas, Mind the gap!, Mater. Horiz. 1 (2014) 17–19. doi:10.1039/C3MH00098B.

[70] X. Gong, M. Tong, F.G. Brunetti, J. Seo, Y. Sun, D. Moses, F. Wudl, A.J. Heeger, Bulk Heterojunction Solar Cells with Large Open-Circuit Voltage: Electron Transfer with Small Donor-Acceptor Energy Offset, Adv. Mater. 23 (2011) 2272–2277. doi:10.1002/adma.201003768.

[71] E.T. Hoke, I.T. Sachs-Quintana, M.T. Lloyd, I. Kauvar, W.R. Mateker, A.M. Nardes, C.H. Peters, N. Kopidakis, M.D. McGehee, The Role of Electron Affinity in Determining Whether Fullerenes Catalyze or Inhibit Photooxidation of Polymers for Solar Cells, Adv. Energy Mater. 2 (2012) 1351–1357. doi:10.1002/aenm.201200169.

[72] M.-M. Ling, P. Erk, M. Gomez, M. Koenemann, J. Locklin, Z. Bao, Air-Stable n-Channel Organic Semiconductors Based on Perylene Diimide Derivatives without Strong Electron Withdrawing Groups, Adv. Mater. 19 (2007) 1123–1127. doi:10.1002/adma.200601705.

[73] J.A. Bartelt, D. Lam, T.M. Burke, S.M. Sweetnam, M.D. McGehee, Charge-Carrier Mobility Requirements for Bulk Heterojunction Solar Cells with High Fill Factor and External Quantum Efficiency >90%, Adv. Energy Mater. 5 (2015). doi:10.1002/aenm.201500577.

[74] T.D. Anthopoulos, D.M. de Leeuw, E. Cantatore, S. Setayesh, E.J. Meijer, C. Tanase, J.C. Hummelen, P.W.M. Blom, Organic complementary-like inverters employing methanofullerene-based ambipolar field-effect transistors, Appl. Phys. Lett. (2004). doi:10.1063/1.1812577.

[75] E.G. Bittle, J.I. Basham, T.N. Jackson, O.D. Jurchescu, D.J. Gundlach, Mobility overestimation due to gated contacts in organic field-effect transistors, Nat. Commun. 7 (2016) 10908. doi:10.1038/ncomms10908.

[76] J.-P. Sun, A.D. Hendsbee, A.F. Eftaiha, C. Macaulay, L.R. Rutledge, G.C. Welch, I.G. Hill, Phthalimide–thiophene-based conjugated organic small molecules with high electron mobility, J. Mater. Chem. C. 2 (2014) 2612–2621. doi:10.1039/C3TC32497D.

[77] H. Fukagawa, H. Yamane, T. Kataoka, S. Kera, M. Nakamura, K. Kudo, N. Ueno, Origin of the highest occupied band position in pentacene films from ultraviolet photoelectron spectroscopy: Hole stabilization versus band dispersion, Phys. Rev. B. 73 (2006) 245310. doi:10.1103/PhysRevB.73.245310.

[78] N. Koch, I. Salzmann, R.L. Johnson, J. Pflaum, R. Friedlein, J.P. Rabe, Molecular orientation dependent energy levels at interfaces with pentacene and pentacenequinone, Org. Electron. 7 (2006) 537–545. doi:10.1016/j.orgel.2006.07.010.

[79] K. Ihm, B. Kim, T.-H. Kang, K.-J. Kim, M.H. Joo, T.H. Kim, S.S. Yoon, S. Chung, Molecular orientation dependence of hole-injection barrier in pentacene thin film on the Au surface in organic thin film transistor, Appl. Phys. Lett. 89 (2006) 033504. doi:10.1063/1.2227712.

[80] S. Duhm, G. Heimel, I. Salzmann, H. Glowatzki, R.L. Johnson, A. Vollmer, J.P. Rabe, N. Koch, Orientation-dependent ionization energies and interface dipoles in ordered molecular assemblies, Nat. Mater. 7 (2008) 326–332. doi:10.1038/nmat2119.

[81] H. Sun, S. Ryno, C. Zhong, M.K. Ravva, Z. Sun, T. Körzdörfer, J.-L. Brédas, Ionization Energies, Electron Affinities, and Polarization Energies of Organic Molecular Crystals: Quantitative Estimations from a Polarizable Continuum Model (PCM)-Tuned Range-Separated Density Functional Approach, J. Chem. Theory Comput. 12 (2016) 2906–2916. doi:10.1021/acs.jctc.6b00225.

[82] G.R. Desiraju, A. Gavezzotti, Crystal structures of polynuclear aromatic hydrocarbons. Classification, rationalization and prediction from molecular structure, Acta Crystallogr. B. 45 (1989) 473–482. doi:10.1107/S0108768189003794.

[83] A.F. Eftaiha, J.-P. Sun, A.D. Hendsbee, C. Macaulay, I.G. Hill, G.C. Welch, High Open Circuit Voltage Organic Solar Cells based upon Fullerene Free Bulk-Heterojunction Active Layers., Can. J. Chem. (2014). doi:10.1139/cjc-2014-0099.

[84] D.J. Burke, D.J. Lipomi, Green chemistry for organic solar cells, Energy Environ. Sci. 6 (2013) 2053–2066. doi:10.1039/C3EE41096J.

[85] A.D. Hendsbee, J.-P. Sun, T.M. McCormick, I.G. Hill, G.C. Welch, Unusual loss of electron mobility upon furan for thiophene substitution in a molecular semiconductor, Org. Electron. 18 (2015) 118–125. doi:10.1016/j.orgel.2014.12.033.

[86] P. Keg, A. Lohani, D. Fichou, Y.M. Lam, Y. Wu, B.S. Ong, S.G. Mhaisalkar, Direct Observation of Alkyl Chain Interdigitation in Conjugated Polyquarterthiophene Self-Organized on Graphite Surfaces, Macromol. Rapid Commun. 29 (2008) 1197–1202. doi:10.1002/marc.200800012.

[87] A.D. Hendsbee, S.M. McAfee, J.-P. Sun, T.M. McCormick, I.G. Hill, G.C. Welch, Phthalimide-based π-conjugated small molecules with tailored electronic energy levels for use as acceptors in organic solar cells, J. Mater. Chem. C. 3 (2015) 8904–8915. doi:10.1039/C5TC01877C.

[88] S.M. McAfee, J.M. Topple, A.-J. Payne, J.-P. Sun, I.G. Hill, G.C. Welch, An Electron-Deficient Small Molecule Accessible from Sustainable Synthesis and Building Blocks for Use as a Fullerene Alternative in Organic Photovoltaics, ChemPhysChem. 16 (2015) 1190–1202. doi:10.1002/cphc.201402662.

[89] J.M. Topple, S.M. McAfee, G.C. Welch, I.G. Hill, Pivotal factors in solution-processed, non-fullerene, all small-molecule organic solar cell device optimization, Org. Electron. 27 (2015) 197–201. doi:10.1016/j.orgel.2015.09.020.

[90] S. McAfee, J. M. Topple, J.-P. Sun, I. G. Hill, G. C. Welch, The structural evolution of an isoindigo-based non-fullerene acceptor for use in organic photovoltaics, RSC Adv. 5 (2015) 80098–80109. doi:10.1039/C5RA16696A.

[91] F. Würthner, C.R. Saha-Möller, B. Fimmel, S. Ogi, P. Leowanawat, D. Schmidt, Perylene Bisimide Dye Assemblies as Archetype Functional Supramolecular Materials, Chem. Rev. 116 (2016) 962–1052. doi:10.1021/acs.chemrev.5b00188.

[92] W. Herbst, K. Hunger, G. Wilker, H. Ohleier, R. Winter, Front Matter, in: Ind. Org. Pigments, Wiley-VCH Verlag GmbH & Co. KGaA, 2004: pp. i–xvii. http://onlinelibrary.wiley.com/doi/10.1002/3527602429.fmatter/summary (accessed February 5, 2016).

[93] P.R.L. Malenfant, C.D. Dimitrakopoulos, J.D. Gelorme, L.L. Kosbar, T.O. Graham, A. Curioni, W. Andreoni, N-type organic thin-film transistor with high field-effect mobility based on a N,N′-dialkyl-3,4,9,10-perylene tetracarboxylic diimide derivative, Appl. Phys. Lett. 80 (2002) 2517–2519. doi:10.1063/1.1467706.

[94] L. Ma, Y. Guo, Y. Wen, Y. Liu, X. Zhan, High-mobility, air stable bottom-contact n-channel thin film transistors based on N,N′-ditridecyl perylene diimide, Appl. Phys. Lett. 103 (2013) 203303. doi:10.1063/1.4831971.

[95] D.R.T. Zahn, G.N. Gavrila, M. Gorgoi, The transport gap of organic semiconductors studied using the combination of direct and inverse photoemission, Chem. Phys. 325 (2006) 99–112. doi:10.1016/j.chemphys.2006.02.003.

[96] X. Zhang, B. Jiang, X. Zhang, A. Tang, J. Huang, C. Zhan, J. Yao, Cooperatively Tuning Phase Size and Absorption of Near IR Photons in P3HT:Perylene Diimide Solar Cells by Bay-Modifications on the Acceptor, J. Phys. Chem. C. 118 (2014) 24212–24220. doi:10.1021/jp5093674.

[97] P.E. Hartnett, A. Timalsina, H.S.S.R. Matte, N. Zhou, X. Guo, W. Zhao, A. Facchetti, R.P.H. Chang, M.C. Hersam, M.R. Wasielewski, T.J. Marks, Slip-Stacked Perylenediimides as an Alternative Strategy for High Efficiency Nonfullerene Acceptors in Organic Photovoltaics, J. Am. Chem. Soc. 136 (2014) 16345–16356. doi:10.1021/ja508814z.

[98] R. Shivanna, S. Shoaee, S. Dimitrov, S.K. Kandappa, S. Rajaram, J.R. Durrant, K.S. Narayan, Charge generation and transport in efficient organic bulk heterojunction solar cells with a perylene acceptor, Energy Env. Sci. 7 (2014) 435–441. doi:10.1039/C3EE42484G.

[99] W. Jiang, L. Ye, X. Li, C. Xiao, F. Tan, W. Zhao, J. Hou, Z. Wang, Bay-linked perylene bisimides as promising non-fullerene acceptors for organic solar cells, Chem. Commun. 50 (2014) 1024. doi:10.1039/c3cc47204c.

[100] Z. Lu, B. Jiang, X. Zhang, A. Tang, L. Chen, C. Zhan, J. Yao, Perylene–Diimide Based Non-Fullerene Solar Cells with 4.34% Efficiency through Engineering Surface Donor/Acceptor Compositions, Chem. Mater. 26 (2014) 2907–2914. doi:10.1021/cm5006339.

[101] Y. Zhong, M.T. Trinh, R. Chen, W. Wang, P.P. Khlyabich, B. Kumar, Q. Xu, C.-Y. Nam, M.Y. Sfeir, C. Black, M.L. Steigerwald, Y.-L. Loo, S. Xiao, F. Ng, X.-Y. Zhu, C. Nuckolls, Efficient Organic Solar Cells with Helical Perylene Diimide Electron Acceptors, J. Am. Chem. Soc. 136 (2014) 15215–15221. doi:10.1021/ja5092613.

[102] Y. Lin, Y. Wang, J. Wang, J. Hou, Y. Li, D. Zhu, X. Zhan, A Star-Shaped Perylene Diimide Electron Acceptor for High-Performance Organic Solar Cells, Adv. Mater. 26 (2014) 5137–5142. doi:10.1002/adma.201400525.

[103] Y. Zhong, M.T. Trinh, R. Chen, G.E. Purdum, P.P. Khlyabich, M. Sezen, S. Oh, H. Zhu, B. Fowler, B. Zhang, W. Wang, C.-Y. Nam, M.Y. Sfeir, C.T. Black, M.L. Steigerwald, Y.-L. Loo, F. Ng, X.-Y. Zhu, C. Nuckolls, Molecular helices as electron acceptors in high-performance bulk heterojunction solar cells, Nat. Commun. 6 (2015) 8242. doi:10.1038/ncomms9242.

[104] Y. Liu, C. Mu, K. Jiang, J. Zhao, Y. Li, L. Zhang, Z. Li, J.Y.L. Lai, H. Hu, T. Ma, R. Hu, D. Yu, X. Huang, B.Z. Tang, H. Yan, A Tetraphenylethylene Core-Based 3D Structure Small Molecular Acceptor Enabling Efficient Non-Fullerene Organic Solar Cells, Adv. Mater. 27 (2015) 1015–1020. doi:10.1002/adma.201404152.

[105] M.A. Angadi, D. Gosztola, M.R. Wasielewski, Characterization of photovoltaic cells using poly(phenylenevinylene) doped with perylenediimide electron acceptors, J. Appl. Phys. 83 (1998) 6187–6189. doi:10.1063/1.367491.

[106] J.J. Dittmer, E.A. Marseglia, R.H. Friend, Electron Trapping in Dye/Polymer Blend Photovoltaic Cells, Adv. Mater. 12 (2000) 1270–1274. doi:10.1002/1521-4095(200009)12:17<1270::AID-ADMA1270>3.0.CO;2-8.

[107] K. Petritsch, J.J. Dittmer, E.A. Marseglia, R.H. Friend, A. Lux, G.G. Rozenberg, S.C. Moratti, A.B. Holmes, Dye-based donor/acceptor solar cells, Sol. Energy Mater. Sol. Cells. 61 (2000) 63–72. doi:10.1016/S0927-0248(99)00097-5.

[108] M.J. Yang, S.L. Lu, Y. Li, Novel electron acceptors based on perylenetetracarboxylates for plastic solar cells, J. Mater. Sci. Lett. 22 (2003) 813–815. doi:10.1023/A:1023960108880.

[109] V. Kamm, G. Battagliarin, I.A. Howard, W. Pisula, A. Mavrinskiy, C. Li, K. Müllen, F. Laquai, Polythiophene:Perylene Diimide Solar Cells – the Impact of Alkyl-Substitution on the Photovoltaic Performance, Adv. Energy Mater. 1 (2011) 297–302. doi:10.1002/aenm.201000006.

[110] J. Li, F. Dierschke, J. Wu, A.C. Grimsdale, K. Müllen, Poly(2,7-carbazole) and perylene tetracarboxydiimide: a promising donor/acceptor pair for polymer solar cells, J Mater Chem. 16 (2006) 96–100. doi:10.1039/B512373A.

[111] W. Wu, L. Liu, Y. Zhou, S. Wen, W. Tian, Morphology and properties of poly(2-methoxy-5-(2′-ethyl-hexyloxy)-p-phenylenevinylene) (MEH-PPV): N,N′-bis(1-ethylpropyl)-3,4:9,10-perylene bis(tetracarboxyl diimide) (EP-PTC) based solar cells, Curr. Appl. Phys. 9 (2009) 950–955. doi:10.1016/j.cap.2008.09.010.

[112] H.C. Hesse, J. Weickert, M. Al-Hussein, L. Dössel, X. Feng, K. Müllen, L. Schmidt-Mende, Discotic materials for organic solar cells: Effects of chemical structure on assembly and performance, Sol. Energy Mater. Sol. Cells. 94 (2010) 560–567. doi:10.1016/j.solmat.2009.11.024.

[113] M. Al-Hussein, H.C. Hesse, J. Weickert, L. Dössel, X. Feng, K. Müllen, L. Schmidt-Mende, Structural properties of the active layer of discotic hexabenzocoronene/perylene diimide bulk hetero junction photovoltaic devices: The role of alkyl side chain length, Thin Solid Films. 520 (2011) 307–313. doi:10.1016/j.tsf.2011.06.044.

[114] A. Sharenko, C.M. Proctor, T.S. van der Poll, Z.B. Henson, T.-Q. Nguyen, G.C. Bazan, A High-Performing Solution-Processed Small Molecule:Perylene Diimide Bulk Heterojunction Solar Cell, Adv. Mater. 25 (2013) 4403–4406. doi:10.1002/adma.201301167.

[115] A. Sharenko, D. Gehrig, F. Laquai, T.-Q. Nguyen, The Effect of Solvent Additive on the Charge Generation and Photovoltaic Performance of a Solution-Processed Small Molecule:Perylene Diimide Bulk Heterojunction Solar Cell, Chem. Mater. 26 (2014) 4109–4118. doi:10.1021/cm5010483.

[116] M. Li, J. Liu, X. Cao, K. Zhou, Q. Zhao, X. Yu, R. Xing, Y. Han, Achieving balanced intermixed and pure crystalline phases in PDI-based non-fullerene organic solar cells via selective solvent additives, Phys Chem Chem Phys. 16 (2014) 26917–26928. doi:10.1039/C4CP04161E.

[117] Y. Chen, X. Zhang, C. Zhan, J. Yao, In-depth understanding of photocurrent enhancement in solution-processed small-molecule:perylene diimide non-fullerene organic solar cells, Phys. Status Solidi A. 212 (2015) 1961–1968. doi:10.1002/pssa.201532102.

[118] W.S. Shin, H.-H. Jeong, M.-K. Kim, S.-H. Jin, M.-R. Kim, J.-K. Lee, J.W. Lee, Y.-S. Gal, Effects of functional groups at perylene diimide derivatives on organic photovoltaic device application, J. Mater. Chem. 16 (2006) 384–390. doi:10.1039/B512983D.

[119] S. Rajaram, P.B. Armstrong, B.J. Kim, J.M.J. Fréchet, Effect of Addition of a Diblock Copolymer on Blend Morphology and Performance of Poly(3-hexylthiophene):Perylene Diimide Solar Cells, Chem. Mater. 21 (2009) 1775–1777. doi:10.1021/cm900911x.

[120] T.W. Holcombe, J.E. Norton, J. Rivnay, C.H. Woo, L. Goris, C. Piliego, G. Griffini, A. Sellinger, J.-L. Brédas, A. Salleo, J.M.J. Fréchet, Steric Control of the Donor/Acceptor Interface: Implications in Organic Photovoltaic Charge Generation, J. Am. Chem. Soc. 133 (2011) 12106–12114. doi:10.1021/ja203235z.

[121] J.-P. Sun, A.D. Hendsbee, A.J. Dobson, G.C. Welch, I.G. Hill, Perylene diimide based all small-molecule organic solar cells: Impact of branched-alkyl side chains on solubility, photophysics, self-assembly, and photovoltaic parameters, Org. Electron. 35 (2016) 151–157. doi:10.1016/j.orgel.2016.05.012.

[122] G. Klebe, F. Graser, E. Hädicke, J. Berndt, Crystallochromy as a solid-state effect: correlation of molecular conformation, crystal packing and colour in perylene-3,4:9,10-bis(dicarboximide) pigments, Acta Crystallogr. B. 45 (1989) 69–77. doi:10.1107/S0108768188010407.

[123] A.E. Clark, C. Qin, A.D.Q. Li, Beyond Exciton Theory: A Time-Dependent DFT and Franck−Condon Study of Perylene Diimide and Its Chromophoric Dimer, J. Am. Chem. Soc. 129 (2007) 7586–7595. doi:10.1021/ja0687724.

[124] C. Huang, S. Barlow, S.R. Marder, Perylene-3,4,9,10-tetracarboxylic Acid Diimides: Synthesis, Physical Properties, and Use in Organic Electronics, J. Org. Chem. 76 (2011) 2386–2407. doi:10.1021/jo2001963.

[125] Y. Nagao, Synthesis and properties of perylene pigments, Prog. Org. Coat. 31 (1997) 43–49. doi:10.1016/S0300-9440(97)00017-9.

[126] K. Balakrishnan, A. Datar, T. Naddo, J. Huang, R. Oitker, M. Yen, J. Zhao, L. Zang, Effect of Side-Chain Substituents on Self-Assembly of Perylene Diimide Molecules: Morphology Control, J. Am. Chem. Soc. 128 (2006) 7390–7398. doi:10.1021/ja061810z.

[127] Z. Chen, V. Stepanenko, V. Dehm, P. Prins, L.D.A. Siebbeles, J. Seibt, P. Marquetand, V. Engel, F. Würthner, Photoluminescence and Conductivity of Self-Assembled π–π Stacks of Perylene Bisimide Dyes, Chem. – Eur. J. 13 (2007) 436–449. doi:10.1002/chem.200600889.

[128] A.D. Hendsbee, J.-P. Sun, W.K. Law, H. Yan, I.G. Hill, D.M. Spasyuk, G.C. Welch, Synthesis, Self-Assembly, and Solar Cell Performance of N-Annulated Perylene Diimide Non-Fullerene Acceptors, Chem. Mater. 28 (2016) 7098–7109. doi:10.1021/acs.chemmater.6b03292.

[129] E. Aluicio-Sarduy, R. Singh, Z. Kan, T. Ye, A. Baidak, A. Calloni, G. Berti, L. Duò, A. Iosifidis, S. Beaupré, M. Leclerc, H.-J. Butt, G. Floudas, P.E. Keivanidis, Elucidating the Impact of Molecular Packing and Device Architecture on the Performance of Nanostructured Perylene Diimide Solar Cells, ACS Appl. Mater. Interfaces. 7 (2015) 8687–8698. doi:10.1021/acsami.5b00827.

[130] B. Kan, M. Li, Q. Zhang, F. Liu, X. Wan, Y. Wang, W. Ni, G. Long, X. Yang, H. Feng, Y. Zuo, M. Zhang, F. Huang, Y. Cao, T.P. Russell, Y. Chen, A Series of Simple Oligomer-like Small Molecules Based on Oligothiophenes for Solution-Processed Solar Cells with High Efficiency, J. Am. Chem. Soc. 137 (2015) 3886–3893. doi:10.1021/jacs.5b00305.

[131] B. Kan, Q. Zhang, M. Li, X. Wan, W. Ni, G. Long, Y. Wang, X. Yang, H. Feng, Y. Chen, Solution-Processed Organic Solar Cells Based on Dialkylthiol-Substituted Benzodithiophene Unit with Efficiency near 10%, J. Am. Chem. Soc. 136 (2014) 15529–15532. doi:10.1021/ja509703k.

[132] L. Yuan, K. Lu, B. Xia, J. Zhang, Z. Wang, Z. Wang, D. Deng, J. Fang, L. Zhu, Z. Wei, Acceptor End-Capped Oligomeric Conjugated Molecules with Broadened Absorption and Enhanced Extinction Coefficients for High-Efficiency Organic Solar Cells, Adv. Mater. 28 (2016) 5980–5985. doi:10.1002/adma.201600512.

[133] J.-L. Wang, K.-K. Liu, J. Yan, Z. Wu, F. Liu, F. Xiao, Z.-F. Chang, H.-B. Wu, Y. Cao, T.P. Russell, Series of Multifluorine Substituted Oligomers for Organic Solar Cells with Efficiency over 9% and Fill Factor of 0.77 by Combination Thermal and Solvent Vapor Annealing, J. Am. Chem. Soc. 138 (2016) 7687–7697. doi:10.1021/jacs.6b03495.

[134] J. Huang, J.H. Carpenter, C.-Z. Li, J.-S. Yu, H. Ade, A.K.-Y. Jen, Highly Efficient Organic Solar Cells with Improved Vertical Donor–Acceptor Compositional Gradient Via an Inverted Off-Center Spinning Method, Adv. Mater. 28 (2016) 967–974. doi:10.1002/adma.201504014.

[135] L. Huo, T. Liu, X. Sun, Y. Cai, A.J. Heeger, Y. Sun, Single-Junction Organic Solar Cells Based on a Novel Wide-Bandgap Polymer with Efficiency of 9.7%, Adv. Mater. 27 (2015) 2938–2944. doi:10.1002/adma.201500647.

[136] D. Meng, H. Fu, C. Xiao, X. Meng, T. Winands, W. Ma, W. Wei, B. Fan, L. Huo, N.L. Doltsinis, Y. Li, Y. Sun, Z. Wang, Three-Bladed Rylene Propellers with Three-Dimensional Network Assembly for Organic Electronics, J. Am. Chem. Soc. 138 (2016) 10184–10190. doi:10.1021/jacs.6b04368.

[137] Y. Lin, F. Zhao, Q. He, L. Huo, Y. Wu, T.C. Parker, W. Ma, Y. Sun, C. Wang, D. Zhu, A.J. Heeger, S.R. Marder, X. Zhan, High-Performance Electron Acceptor with Thienyl Side Chains for Organic Photovoltaics, J. Am. Chem. Soc. 138 (2016) 4955–4961. doi:10.1021/jacs.6b02004.

[138] S. Li, L. Ye, W. Zhao, S. Zhang, S. Mukherjee, H. Ade, J. Hou, Energy-Level Modulation of Small-Molecule Electron Acceptors to Achieve over 12% Efficiency in Polymer Solar Cells, Adv. Mater. 28 (2016) 9423–9429. doi:10.1002/adma.201602776.

[139] O.K. Kwon, J.-H. Park, D.W. Kim, S.K. Park, S.Y. Park, An All-Small-Molecule Organic Solar Cell with High Efficiency Nonfullerene Acceptor, Adv. Mater. 27 (2015) 1951–1956. doi:10.1002/adma.201405429.

[140] M.J. Griffith, N.A. Cooling, B. Vaughan, D.C. Elkington, A.S. Hart, A.G. Lyons, S. Quereshi, W.J. Belcher, P.C. Dastoor, Combining Printing, Coating, and Vacuum Deposition on the Roll-to-Roll Scale: A Hybrid Organic Photovoltaics Fabrication, IEEE J. Sel. Top. Quantum Electron. 22 (2016) 112–125. doi:10.1109/JSTQE.2015.2487968.

[141] L. Lucera, F. Machui, P. Kubis, H.J. Egelhaaf, C.J. Brabec, Highly efficient, large area, roll coated flexible and rigid solar modules: Design rules and realization, in: 2016 IEEE 43rd Photovolt. Spec. Conf. PVSC, 2016: pp. 0234–0237. doi:10.1109/PVSC.2016.7749585.

[142] S. Berny, N. Blouin, A. Distler, H.-J. Egelhaaf, M. Krompiec, A. Lohr, O.R. Lozman, G.E. Morse, L. Nanson, A. Pron, T. Sauermann, N. Seidler, S. Tierney, P. Tiwana, M. Wagner, H. Wilson, Solar Trees: First Large-Scale Demonstration of Fully Solution Coated, Semitransparent, Flexible Organic Photovoltaic Modules, Adv. Sci. 3 (2016) n/a-n/a. doi:10.1002/advs.201500342.

[143] E. Kam-Lum, A method to characterize OPV temperature, humidity and irradiance combined degradation- preliminary results, in: 2012 38th IEEE Photovolt. Spec. Conf., 2012: pp. 003253–003258. doi:10.1109/PVSC.2012.6318271.

[144] L.J. Guo, Nanoimprint Lithography: Methods and Material Requirements, Adv. Mater. 19 (2007) 495–513. doi:10.1002/adma.200600882.

[145] Y. Yang, K. Mielczarek, A. Zakhidov, W. Hu, Efficient Low Bandgap Polymer Solar Cell with Ordered Heterojunction Defined by Nanoimprint Lithography, ACS Appl. Mater. Interfaces. 6 (2014) 19282–19287. doi:10.1021/am505303a.

[146] W. Lee, S.-J. Park, Porous Anodic Aluminum Oxide: Anodization and Templated Synthesis of Functional Nanostructures, Chem. Rev. 114 (2014) 7487–7556. doi:10.1021/cr500002z.

[147] U. Malinovskis, R. Poplausks, I. Apsite, R. Meija, J. Prikulis, F. Lombardi, D. Erts, Ultrathin Anodic Aluminum Oxide Membranes for Production of Dense Sub-20 nm Nanoparticle Arrays, J. Phys. Chem. C. 118 (2014) 8685–8690. doi:10.1021/jp412689y.

[148] F. Zhang, X. Liu, C. Pan, J. Zhu, Nano-porous anodic aluminium oxide membranes with 6–19 nm pore diameters formed by a low-potential anodizing process, Nanotechnology. 18 (2007) 345302. doi:10.1088/0957-4484/18/34/345302.

[149] K. Schwirn, W. Lee, R. Hillebrand, M. Steinhart, K. Nielsch, U. Gösele, Self-Ordered Anodic Aluminum Oxide Formed by H2SO4 Hard Anodization, ACS Nano. 2 (2008) 302–310. doi:10.1021/nn7001322.

[150] T.R.B. Foong, A. Sellinger, X. Hu, Origin of the Bottlenecks in Preparing Anodized Aluminum Oxide (AAO) Templates on ITO Glass, ACS Nano. 2 (2008) 2250–2256. doi:10.1021/nn800435n.

[151] M.S.M. Saifullah, T. Ondarçuhu, D.K. Koltsov, C. Joachim, M.E. Welland, A reliable scheme for fabricating sub-5 nm co-planar junctions for single-molecule electronics, Nanotechnology. 13 (2002) 659. doi:10.1088/0957-4484/13/5/323.

[152] J. Lee, A.-R. Han, J. Hong, J.H. Seo, J.H. Oh, C. Yang, Inversion of Dominant Polarity in Ambipolar Polydiketopyrrolopyrrole with Thermally Removable Groups, Adv. Funct. Mater. 22 (2012) 4128–4138. doi:10.1002/adfm.201200940.

APPENDIX A COPYRIGHT STATEMENT

Content contained in this dissertation has been reproduced and/or adapted in accordance with the rights retained by authors for reuse of published materials granted by the Royal Society of Chemistry, the American Chemical Society, and Elsevier. Publications containing the original materials have been appropriately acknowledged.

****

Elsevier:

Dear Jon-Paul,

As an Elsevier journal author, you retain the right to Include the article in a thesis or dissertation (provided that this is not to be published commercially) whether in full or in part, subject to proper acknowledgment; see https://www.elsevier.com/about/our-business/policies/copyright/personal-use for more information. As this is a retained right, no written permission from Elsevier is necessary.

If I may be of further assistance, please let me know.

Best of luck with your thesis and best regards,
Laura

Laura Stingelin
Permissions Helpdesk Associate
ELSEVIER | Global E-Operations Books
+1 215-239-3867 office
l.stingelin@elsevier.com
Contact the Permissions Helpdesk
+1 800-523-4069 x3808 | permissionshelpdesk@elsevier.com

****

Royal Society of Chemistry:

Dear Jon-Paul,

Thank you for your message, and thanks to Professor Skabara for passing it on. As you are intending to include articles on which you are an author within your thesis, you are within your rights to do so without formal authorisation from us (but see limitations to redistribution of particular versions below). Please see our policy here:

http://www.rsc.org/journals-books-databases/journal-authors-reviewers/licences-copyright-permissions/ , section entitled 'Author reusing their own work published by the Royal Society of Chemistry'.

However, please ensure that your co-authors are aware that you intend to include the articles in your thesis. Additionally, please ensure that you include acknowledgement of the original publications in Journal of Materials Chemistry C.

For the reproduction and distribution of the full articles by LAC, you may use the submitted manuscript version immediately. The accepted manuscript version may be distributed after a 12 month embargo period from date of first publication. Our policy on this can be found at http://www.rsc.org/journals-books-databases/open-access/green-open-access/#share.

If you need me to complete the letter nonetheless, i.e. if this email won't suffice, just let me know and also clarify which version of your articles you intend to include in your thesis?

Best wishes and good luck with your thesis!

Annie

Annie Harvey
Managing Editor
Journal of Materials Chemistry A, B & C
Royal Society of Chemistry
Thomas Graham House,
Science Park, Milton Road,
Cambridge, CB4 0WF, UK

****

American Chemical Society:

Dear Dr. Sun,

Thank you for sending that in. After discussing this, we have determined that you should be able to request permission using the below link. I hope this helps!

https://s100.copyright.com/AppDispatchServlet?startPage=7098&pageCount=12&copyright=American+Chemical+Society&author=Arthur+D.+Hendsbee%2C+Jon-Paul+Sun%2C+Wai+Kit+Law%2C+et+al&orderBeanReset=true&imprint=American+Chemical+Society&volumeNum=28&issueNum=19&contentID=acs.chemmater.6b03292&title=Synthesis%2C+Self-Assembly%2C+and+Solar+Cell+Performance+of+N-Annulated+Perylene+Diimide+Non-Fullerene+Acceptors&issn=0897-

4756&publisherName=acs&publication=cmatex&rpt=n&endPage=7109&publicationDate=October+2016

Best,

Craig Lincoln
Chemistry of Materials Editorial Office

Contents of link sent from Craig Lincoln:

If credit is given to another source for the material you requested, permission must be obtained from that source.

PERMISSION/LICENSE IS GRANTED FOR YOUR ORDER AT NO CHARGE

This type of permission/license, instead of the standard Terms & Conditions, is sent to you because no fee is being charged for your order. Please note the following:

- Permission is granted for your request in both print and electronic formats, and translations.
- If figures and/or tables were requested, they may be adapted or used in part.
- Please print this page for your records and send a copy of it to your publisher/graduate school.
- Appropriate credit for the requested material should be given as follows: "Reprinted (adapted) with permission from (COMPLETE REFERENCE CITATION). Copyright (YEAR) American Chemical Society." Insert appropriate information in place of the capitalized words.
- One-time permission is granted only for the use specified in your request. No additional uses are granted (such as derivative works or other editions). For any other uses, please submit a new request.

APPENDIX B LIST OF PUBLICATIONS AND CONTRIBUTIONS

1. Carl Roy, Thomas Bura, Serge Beaupré, Marc-André Légaré, **Jon-Paul Sun**, Ian G. Hill, and Mario Leclerc. Fluorinated thiophene-based synthons: polymerization of 1,4-dialkoxybenzene and fluorinated dithieno-2,1,3-benzothiadiazole by direct heteroarylation. *Macromolecules*, 2017, accepted manuscript.

   Contribution: UPS and IPES of polymers.

2. Jonathan Cann, Sergey Dayneko, **Jon-Paul Sun**, Arthur D. Hendsbee, Ian G. Hill, and Gregory C. Welch. N-annulated perylene diimide dimers: acetylene linkers as a strategy for controlling structural conformation and the impact on physical, electronic, optical and photovoltaic properties. *J. Mater. Chem. C*, 2017, **5**, 2074-2083.

   Contribution: UPS and IPES of acceptor molecules, and fabrication, optimization, and characterization of OPV devices cast from chlorobenzene.

3. Arthur D. Hendsbee, **Jon-Paul Sun**, Wai Kit Law, He Yan, Ian G. Hill, Denis M. Spasyuk and Gregory C. Welch. Synthesis, self-assembly, and solar cell performance of N-annulated PDI non-fullerene acceptors. *Chem. Mater.*, 2016, **28**, 7098-7109.

   Contribution: fabrication, optimization, and characterization of OPV devices with PTB7 and PTB7-Th. Discussed in section 4.2.

4. **Jon-Paul Sun**, Arthur D. Hendsbee, Alexander J. Dobson, Gregory C. Welch and Ian G. Hill. Perylene diimide based all small-molecule organic solar cells: Impact of branched-alkyl side chains on solubility, photophysics, self-assembly, and photovoltaic parameters. *Org. Electron.*, 2016, **35**, 151-157.

   Contribution: fabrication, optimization, and characterization of OPV devices. Discussed in section 4.1.

5. Lénaï Madec, Lin Ma, Kathlyne J. Nelson, Remi Petibon, **Jon-Paul Sun**, Ian G. Hill and Jeffrey R. Dahn. The effects of a ternary electrolyte additive system on the electrode/electrolyte interfaces in high voltage Li-ion cells. *J. Electrochem. Soc.*, 2016, **163**, A1001-A1009.

   Contribution: analyzed XPS results with lead author.

6. Bayrammurad Saparov, **Jon-Paul Sun**, Weiwei Meng, Zewen Xiao, Hsin-Sheng Duan, Oki Gunawan, Donghyeop Shin, Ian G. Hill, Yanfa Yan and David B. Mitzi. Thin-film deposition and characterization of a Sn-deficient perovskite derivative Cs2SnI6. *Chem. Mater.*, 2016, **28**, 2315-2322.

   Contribution: PES of perovskites.

7. Lénaïc Madec, Remi Petibon, Jian Xia, **Jon-Paul Sun**, Ian G. Hill and Jeffrey R. Dahn. Understanding the role of prop-1-ene-1,3-sultone and vinylene carbonate in LiNi1/3Mn1/3Co1/3O2/graphite pouch cells: electrochemical, GC-MS and XPS analysis. *J. Electrochem. Soc.*, 2015, **162**, A2635-A2645.

   Contribution: analyzed XPS results with lead author.

8. Lénaïc Madec, Remi Petibon, Ken Tasaki, Jian Xia, **Jon-Paul Sun**, Ian G. Hill and Jeffrey R. Dahn. Mechanism of action of ethylene sulfite and vinylene carbonate electrolyte additives in LiNi1/3Mn1/3Co1/3O2/graphite pouch cells: electrochemical, GC-MS and XPS analysis. *Phys. Chem. Chem. Phys.*, 2015, **17**, 27062-27076.

   Contribution: analyzed XPS results with lead author.

9. Ala'a F. Eftaiha, Arthur D. Hendsbee, **Jon-Paul Sun** and Ian G. Hill. The influence of molecular geometry on photophysical properties and self-assembly of phthalimide end-capped thiophene-based organic molecule. *Materials Letters*, 2015, 157, 252-255.

   Contribution: UPS of organic molecules.

10. Seth M. McAfee, Jessica M. Topple, **Jon-Paul Sun**, Ian G. Hill, & Gregory C. Welch. The structural evolution of an isoindigo-based non-fullerene acceptor for use in organic photovoltaics. *RSC Adv.,* 2015, **5**, 80098-80109.

    Contribution: UPS of acceptor molecules.

11. Silvia Masala, Valerio Adinolfi, **Jon Paul Sun**, Silvano Del Gobbo, Oleksandr Voznyy, Illan J. Kramer, Ian G. Hill and Edward H. Sargent. The silicon:colloidal quantum dot heterojunction. *Adv. Mater.*, 2015, **27**, 7445-7450.

Contribution: PES and Kelvin probe of silicon:colloidal quantum dot samples.

12. Arthur D. Hendsbee, Seth M. McAfee, **Jon-Paul Sun**, Teresa M. McCormick, Ian G. Hill and Gregory C Welch. Phthalimide-based π-conjugated small molecules with tailored electronic energy levels for use as acceptors in organic solar cells. *J. Mater. Chem.* C, 2015, **3**, 8904-8915.

Contribution: UPS of acceptor molecules and fabrication, optimization, and characterization of OPV devices. Discussed in section 3.4.

13. Bayrammurad Saparov, Feng Hong, **Jon-Paul Sun**, Hsin-Sheng Duan, Weiwei Meng, Samuel Cameron, Ian G. Hill, Yanfa Yan and David B. Mitzi. Thin-film preparation and characterization of Cs3Sb2I9: a lead-free layered perovskite semiconductor. *Chem. Mater.*, 2015, **27**, 5622-5632.

Contribution: PES of perovskites.

14. Jixian Xu, Andrei Buin, Alexander H. Ip, Wei Li, Oleksandr Voznyy, Riccardo Comin, Mingjian Yuan, Seokmin Jeon, Zhijun Ning, Jeffrey J. McDowell, Pongsakorn Kanjanaboos, **Jon-Paul Sun**, Xinzheng Lan, Li Na Quan, Dong Ha Kim, Ian G. Hill, Peter Maksymovych & Edward H. Sargent. Perovskite–fullerene hybrid materials suppress hysteresis in planar diodes. *Nat. Commun.*, 2015, 6, 7081.

Contribution: Kelvin probe of perovskite-fullerene hybrids.

15. Arthur D. Hendsbee, **Jon-Paul Sun**, Theresa M. McCormick, Ian G. Hill and Gregory C. Welch. Unusual loss of electron mobility upon furan for thiophene substitution in a molecular semiconductor. *Org. Electron*., 2015, 18, 118-125.

Contribution: UPS and fabrication and characterization of TFT devices. Discussed in section 3.3.

16. Seth M. McAfee, Jessica M. Topple, Abby-Jo Payne, **Jon-Paul Sun**, Ian G. Hill, and Gregory C. Welch. An electron deficient small molecule accessible from sustainable synthesis and building blocks for use as a fullerene alternative in organic photovoltaics. *J. Chem. Phys. Chem.*, 2015, **16**, 1190-1202.

Contribution: UPS of acceptor molecules.

17. Lénaïc Madec, Jian Xia, Remi Petibon, Kathlyne J. Nelson, **Jon-Paul Sun**, Ian G. Hill,and Jeff R. Dahn. Effect of sulfate electrolyte additives on LiNi1/3Mn1/3Co1/3O2/graphite pouch cell lifetime: correlation between XPS surface studies and electrochemical test results. *J. Phys. Chem. C*, 2014, **118**, 29608-29622.

Contribution: analyzed XPS results with lead author.

18. Zhijun Ning, Oleksandr Voznyy, Jun Pan, Sjoerd Hoogland, Valerio Adinolfi, Jixian Xu, Min Li, Ahmad R. Kirmani, **Jon-Paul Sun**, James Minor, Kyle W. Kemp, Haopeng Dong, Lisa Rollny, André Labelle, Graham Carey, Brandon Sutherland, Ian Hill, Aram Amassian, Huan Liu, Jiang Tang, Osman M. Bakr and Edward H. Sargent. Air-stable n-type colloidal quantum dot solids. *Nat. Mater.*, 2014, **13**, 822-828.

Contribution: PES and Kelvin prove of colloidal quantum dots.

19. Ala'a F. Eftaiha, **Jon-Paul Sun**, Arthur D. Hendsbee, Casper Macaulay, Ian G. Hill and Gregory C. Welch. High open circuit voltage organic solar cells based upon fullerene free bulk heterojunction active layers. *Can. J. Chem.*, 2014, **92**, 1-8.

Contribution:UPS of acceptor molecule.

20. Ala'a F. Eftaiha, **Jon-Paul Sun**, Ian G. Hill and Gregory C. Welch. Recent advances in non-fullerene, small molecular acceptors for solution processed bulk heterojunction solar cells. *J. Mater. Chem. A*, 2014, **2**, 1201-1213.

Contribution: Wrote section of review article detailing the limitations of fullerenes as acceptors in OPVs.

21. **Jon-Paul Sun**, Arthur D. Hendsbee, Ala'a F. Eftaiha, Casper Macaulay, Lesley R. Rutledge, Gregory C. Welch and Ian G. Hill. Phthalimide-thiophene-based conjugated organic small molecules with high electron mobility. *J. Mater. Chem. C*, 2014, **2**, 2612-2621.

Contribution: UPS and fabrication and characterization of TFT devices. Discussed in section 3.2

22. Arthur D. Hendsbee, **Jon-Paul Sun**, Lesley R. Rutledge, Ian G. Hill and Gregory C. Welch. Electron deficient diketopyrrolopyrrole dyes for organic electronics: synthesis by direct arylation, optoelectronic characterization, and charge carrier mobility. *J. Mater. Chem. A*, 2014, **2**, 4198-4207.

Contribution: UPS and fabrication and characterization of TFT devices. Discussed in section 3.1.

23. Mingqing Wang, **Jon-Paul Sun**, Sandy Suei and Ian G. Hill. Optimizing the photovoltage of polymer/zinc oxide hybrid solar cells by calcium doping. *J. Appl. Phys*., 2012, **112**, 044511.

Contribution: synthesized Ca-doped ZnO nanoparticles.